THE OHIO STATE UNIVERSITY

The Reflection and Transmission Properties of a Triple Band Dichroic Surface

S.W. Schneider and B.A. Munk

The Ohio State University

ElectroScience Laboratory

Department of Electrical Engineering
Columbus, Ohio 43212

Final Technical Report 723108-1
Grant No. NCC3-158
December 1990

National Aeronautics and Space Administration
Lewis Research Center
21000 Brookpark Road
Cleveland, OH 44135

A. Approved for public release; Distribution is unlimited

NOTICES

When Government drawings, specifications, or other data are used for any purpose other than in connection with a definitely related Government procurement operation, the United States Government thereby incurs no responsibility nor any obligation whatsoever, and the fact that the Government may have formulated, furnished, or in any way supplied the said drawings, specifications, or other data, is not to be regarded by implication or otherwise as in any manner licensing the holder or any other person or corporation, or conveying any rights or permission to manufacture, use, or sell any patented invention that may in any way be related thereto.

Contents

List of Figures

Chapter 1

Introduction

This report details the development of a practical dichroic surface design that is reflective in the Ka-band from 22.5 – 27.3 GHz and the Ku-band from 13.7 – 15.1 GHz, yet transparant in the S-band from 2.0 – 2.3 GHz for all planes of incidence, and for angles of incidence out to $\eta = 45°$. The principal components of the design are "gangbuster" arrays. These "gangbuster" arrays are comprised of straight skewed dipole elements as shown in Figure 1.1a. We refer to the array of Figure 1.1a as "gangbuster half-surface" since the dipoles can handle only one polarization, namely an incident field with its E-vector in the plane of the conducting elements. To handle any arbitrary polarization a second "gangbuster half-surface" is rotated 90°, and mounted an array separation distance "s" behind the first as shown in Figure 1.1b. The combination of these two orthogonal "half-surfaces" is referred to as a "whole-surface".

We begin this report by formulating a dichroic surface design (Chapter 2) that is comprised of two parallel "half-surfaces" separated by a dielectric of thickness "d" that is comparable to a fraction of a wavelength at S-band.

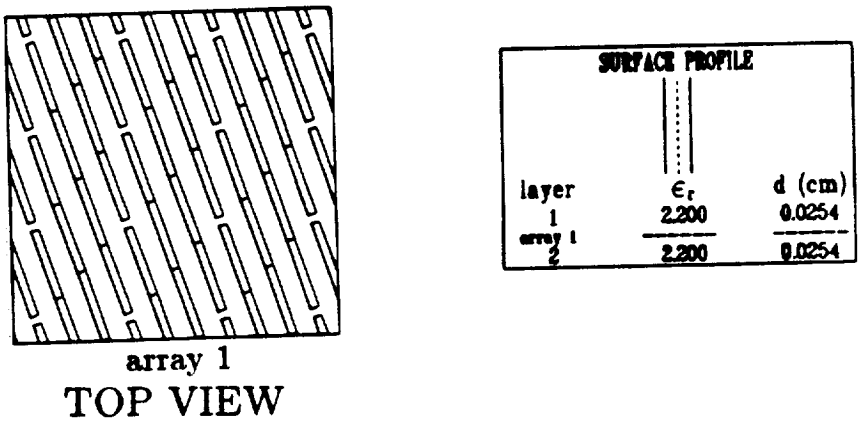

(a)

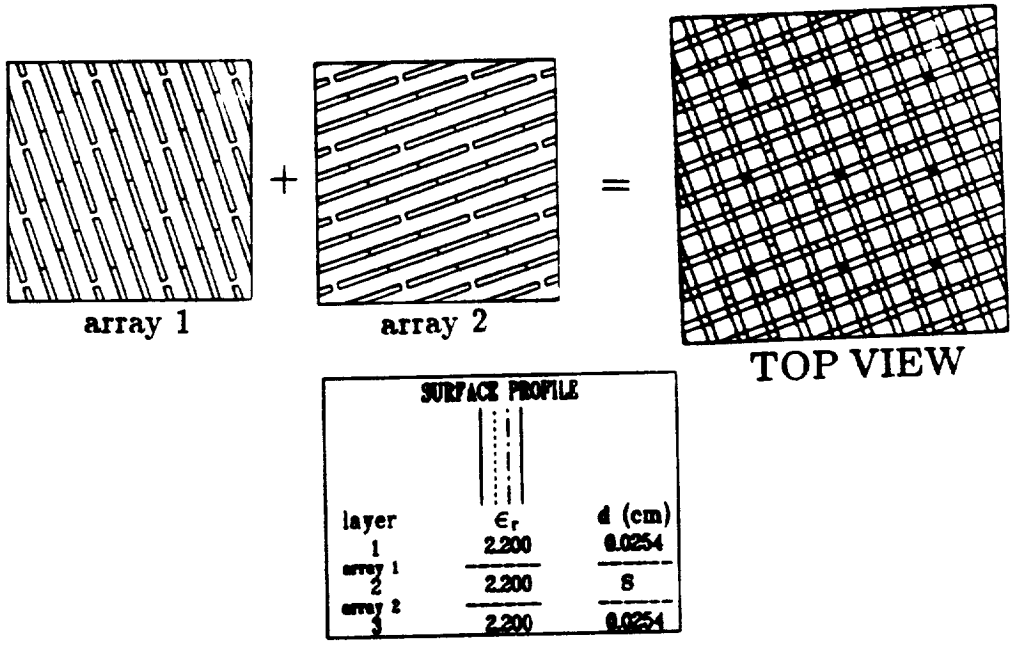

(b)

Figure 1.1: The "gangbuster array" is comprised of straight skewed dipole elements.
a: The "gangbuster half-surface" can only handle polarizations with the E-vector in the plane of the conducting elements.
b: The "gangbuster whole-surface", which is comprised of two orthogonal "gangbuster half-surfaces" separated by as array separation "s", can handle arbitrary polarizations.

A dielectric matching plate is then added to improve the S-band transmission region. We consider only "half-surfaces" when formulating this design inorder to facilitate a deeper understanding of our design approach.

Next, in Chapter 3, we consider how loss (both dielectric and conduction) effects the idealized dichroic surface design of Chapter 2. Here we demonstrate the importance of using low loss dielectrics, particularly for the array substrates. We also show that copper loss is insignificant in this design.

Finally, in Chapter 4 we replace the "gangbuster half-surfaces" of our dichroic surface design with "gangbuster whole-surfaces" thus allowing any arbitrary plane of incidence. This chapter investigates the cross polarization component of this new design. We will find that the cross polarization is quite dependent on the array separation "s" between the orthogonal arrays of our "whole-surface".

1.1 Definition of the Incidence Angles

Figure 1.2 shows the spherical coordinate system used to determine the plane and angle of the incident electric field. From this figure we note that the $\hat{y}$-axis is the polar axis and the angle η is the polar angle. The angle η is defined as the angle of incidence and is measured counterclockwise from the $-\hat{y}$-axis. (Obviously, $\eta = 0°$ corresponds to normal angle of incidence.) The plane of incidence is defined by the plane containing the $\hat{y}$-axis that is at an angle α with the $\hat{x}$-axis.

In all the calculations of this report we have aligned $\hat{z}$-axis in the direc-

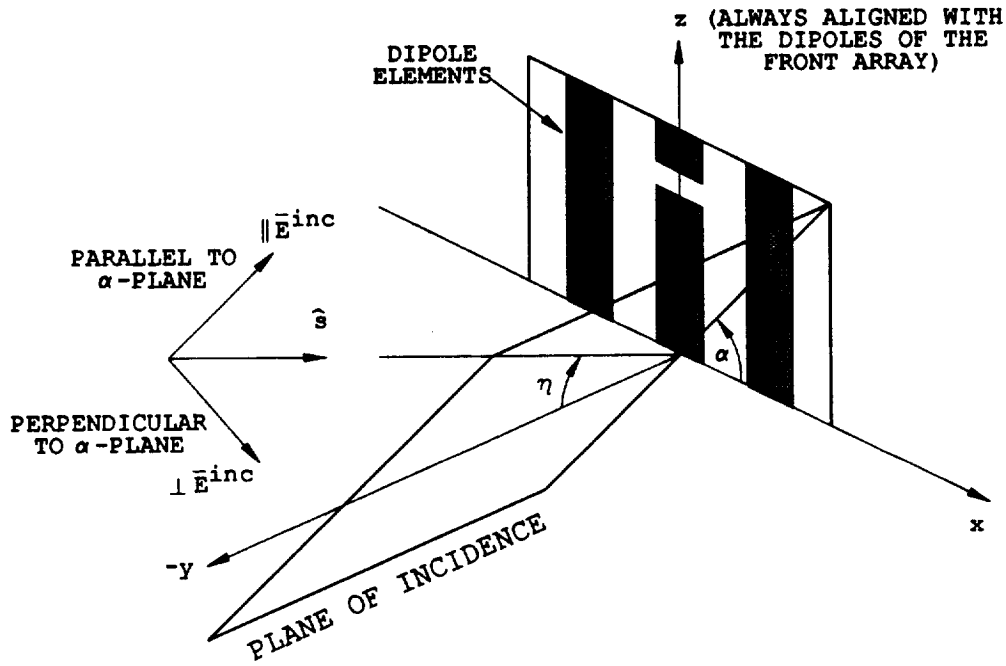

Figure 1.2: The spherical coordinate system used in this report. The direction of the dipole elements of the front "gangbuster half-surface" is always along the $\hat{z}$-axis.

tion of the dipole elements of the front "gangbuster half-surface". Therefore the plane of incidence $\alpha = 0°$ defines the H-plane of the front "half-surface", while $\alpha = 90°$ defines the E-plane of the front "half-surface".

Chapter 2

Design of a Dichroic Surface

In this chapter we formulate a dichroic surface design that is reflective in bands from 13.7 – 15.1 GHz and 22.5 – 27.3 GHz, but transparant from 2.0 – 2.3 GHz for angles of incidence out to $\eta = 45°$. Since our concern here is the parallel polarized component, the design will use only "gangbuster half-surfaces" with the understanding that later (Chapter 4) these "half-surfaces" will be replaced by "gangbuster whole-surfaces". This simplification facilitates a deeper understanding of the design approach by eliminating the subtle effects of cross polarization.

2.1 Single Layer Surfaces

We show in Figure 2.1 the parallel reflection coefficient curves of three types of "gangbuster half-surfaces" at normal angle of incidence. These three "half-surfaces" are comprised of straight skewed elements as shown in the insert of Figure 2.1. It is obvious from this figure that the more densely packed the elements, the more broad banded the reflection properties of the surface. Figure 2.2 shows the parallel reflection coefficient curves for

the same three "half-surface" types at an oblique angle of incidence in the E-plane (specifically $\eta = 45°$). We note a null at $\sim$ 34 GHz in this figure that was not present in the normal incidence case (further, there is no null present when the field is incident obliquely in the H-plane). The reason for this null is that an oblique incident field in the E-plane can excite both an even (fundemental) and an odd current mode on the element as shown in Figure 2.3. The odd mode resonance typically occurs around twice the fundemental resonance. It can be shown that between these two resonances there will always be an infinitly deep null (for no grating lobes, and in the principal planes) which is aptly referred to as a "modal interaction null". (This null is a simple example of Foster's Reactance Theorem.)

At the present, we are not aware of a good, practical way of preventing the odd current mode. We therefore avoid the problem by chosing a surface whose "modal interaction null" occurs above the Ka-reflection band, yet is still reflective in the Ku-band. To this end we selected a type-3 "gangbuster" surface embedded in a dielelectric substrate. The reflection characteristics of this surface are shown in Figure 2.4 for normal angle of incidence, as well as $\eta = 45°$ in both the E and H-planes. All pertinent dimensions are given in the figure insert.

2.2 Double Array Surfaces

2.2.1 Interaction of Two Single Array Surfaces

We saw above that it is possible to find a single "half-surface" that is reflective in both the Ka and Ku-band. Unfortunately, the reflection coefficient

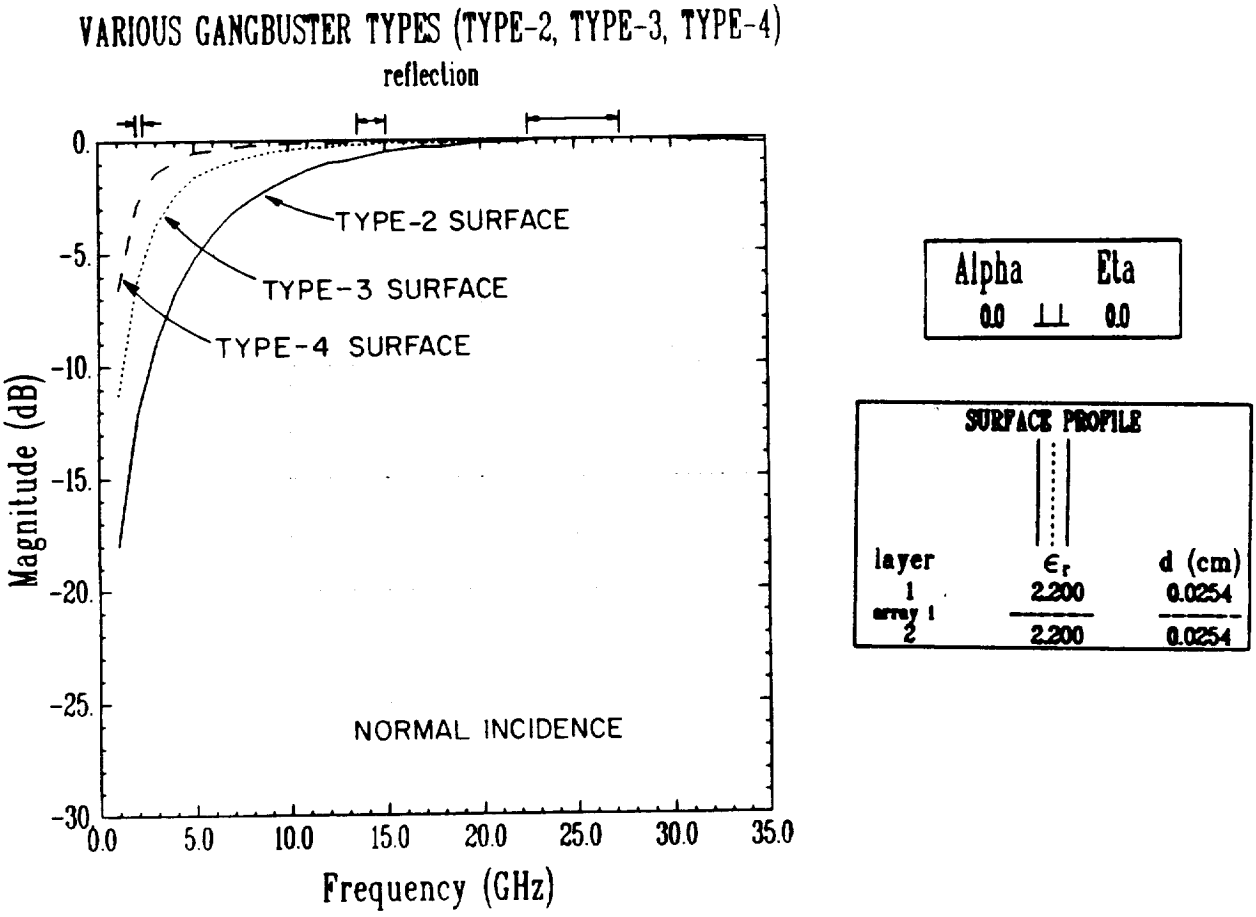

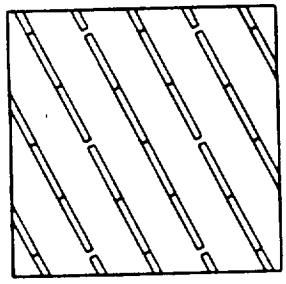

TYPE-2 SURFACE

DX = DZ = .230 cm

L = .5 cm ; W = .015 cm

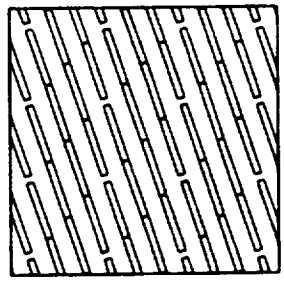

TYPE-3 SURFACE

DX = DZ = .163 cm

L = .5 cm ; W = .015 cm

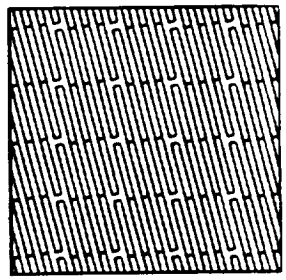

TYPE-4 SURFACE

DX = DZ = .125 cm

L = .5 cm ; W = .015 cm

Figure 2.1: The parallel reflection coefficient curves for type-2, type-3, and type-4 "gangbuster half-surfaces" at normal angle of incidence.

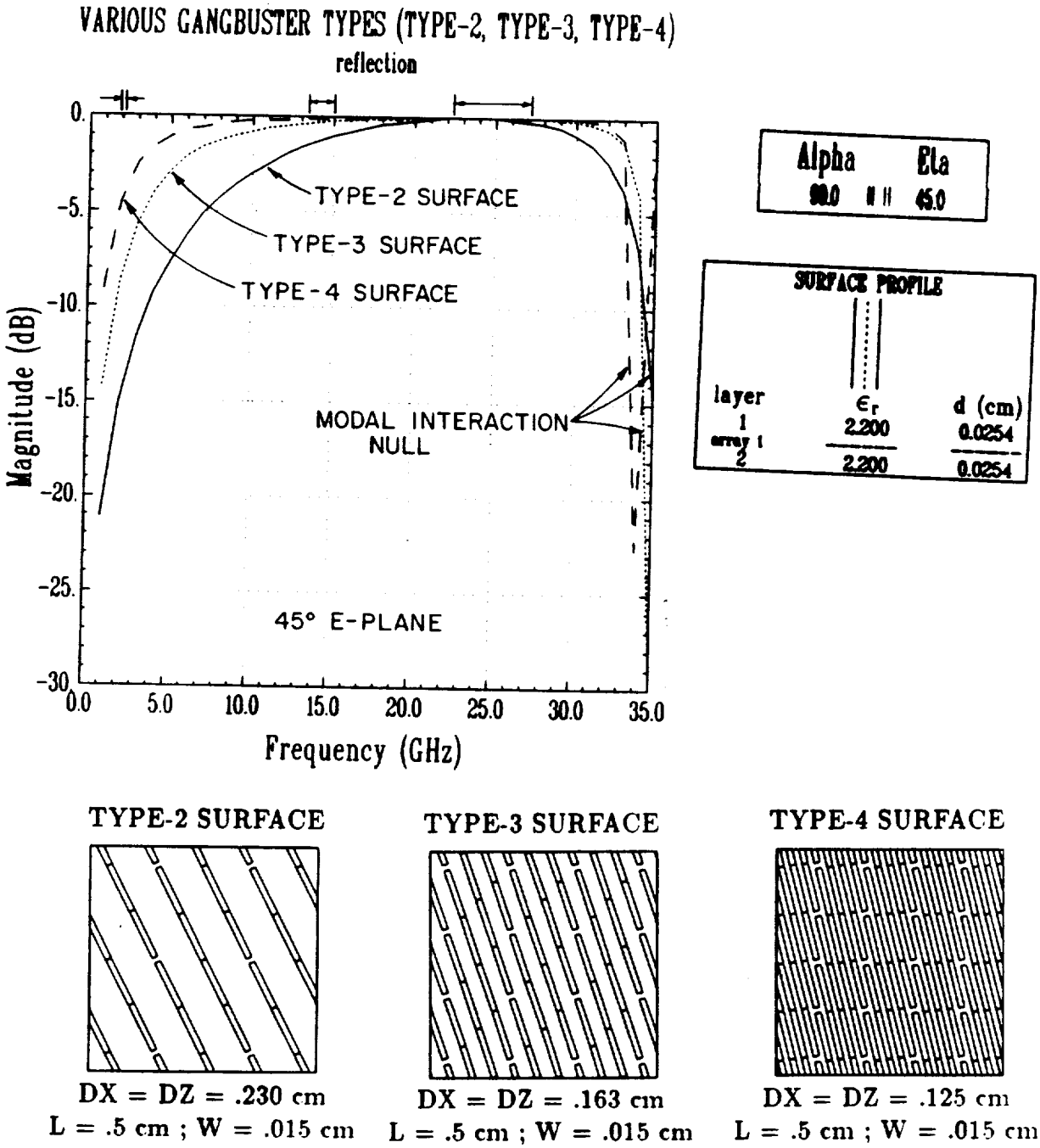

Figure 2.2: The parallel reflection coefficient curves for type-2, type-3, and type-4 "gangbuster half-surfaces" at $\eta = 45°$ angle of incidence in the E-plane.

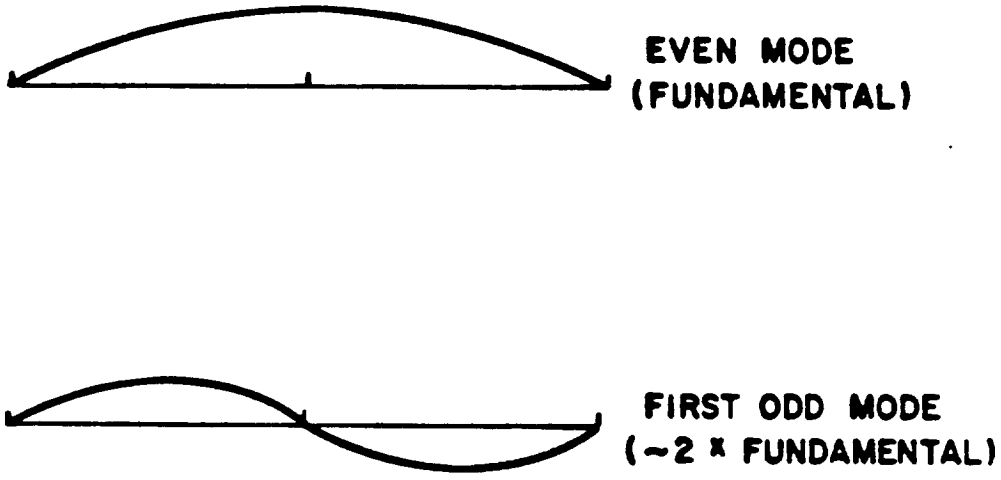

Figure 2.3: An array of dipoles can be excited in the even mode for any angle of incidence, while an odd mode can only be excited by oblique incidence in the E-plane. Between these two resonances in the E-plane there will be a "modal interaction null".

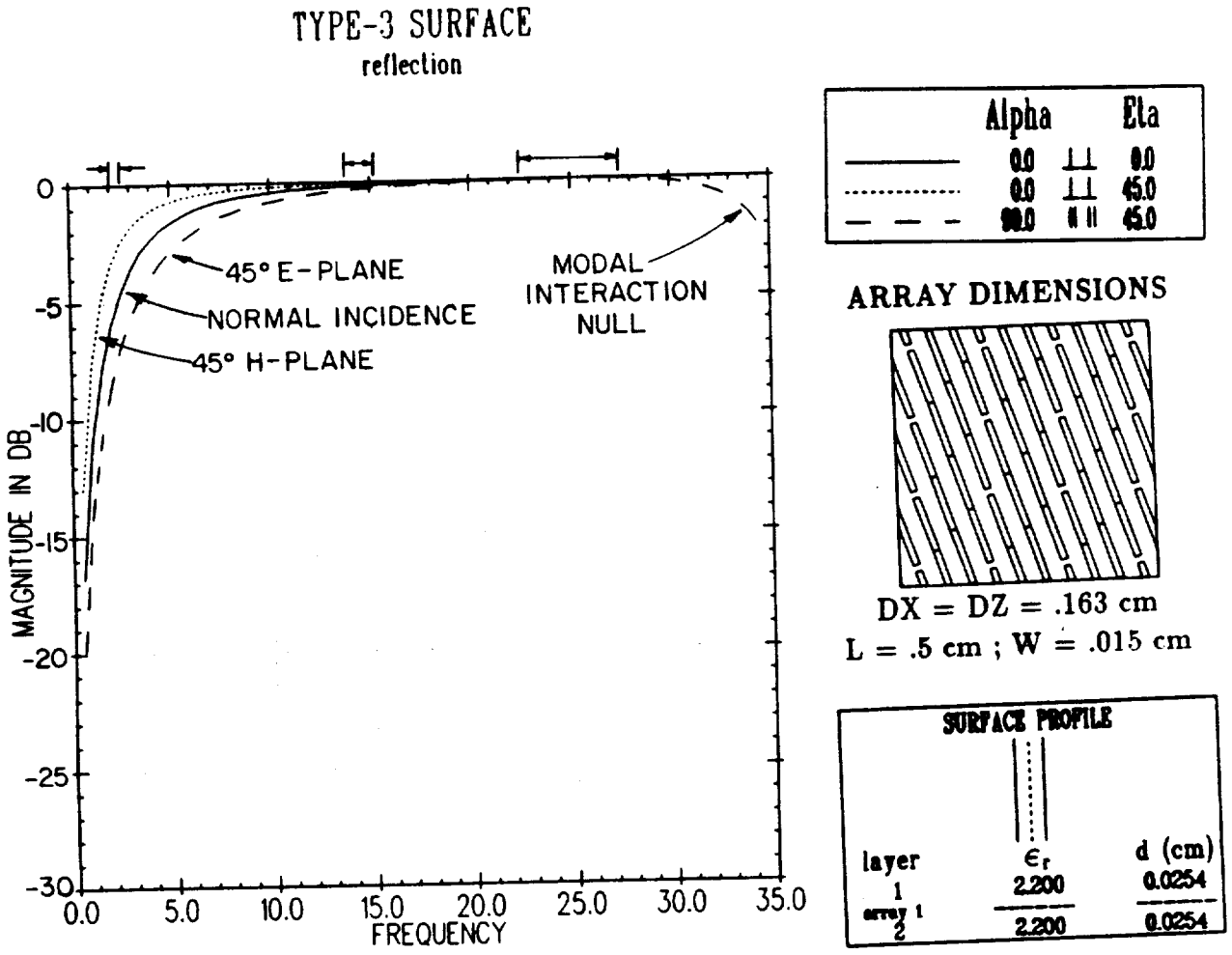

Figure 2.4: The parallel reflection coefficient curves for the type-3 "gang-buster half-surface" chosen as a basis for our dichroic surface design.

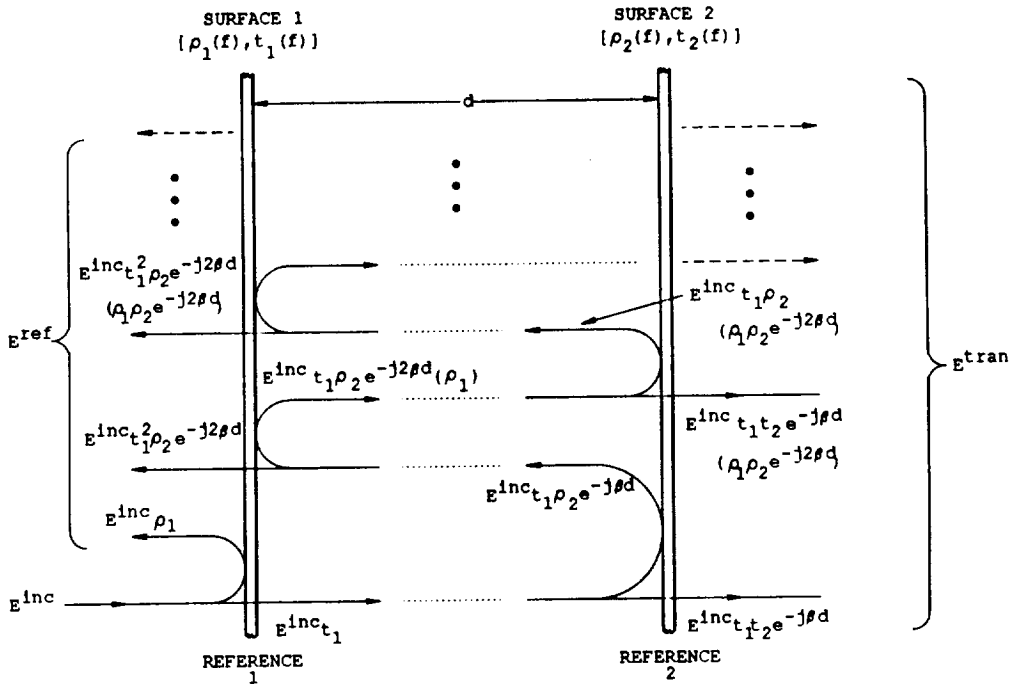

Figure 2.5: A general double array surface consisting of two non-perfect reflective surfaces ($\rho_1 = \rho_1(f)$ and $\rho_2 = \rho_2(f)$) and spaced a distance "d" apart.

for this very broadband surface does not roll off fast enough have a good transmission region in S-band (2.0-2.3 GHz). To obtain a reflection curve that is more flat on top and has a low frequency transmission region, we now place two parallel surfaces a distance "d" behind each other to form a *double array* surface. This distance "d" is comparable to a quarter of a wavelength at S-band frequencies.

Figure 2.5 shows a general double array surface in which two lossless surfaces are spaced a distance "d" apart. Each of these surfaces is character-

ized by a reflection coefficient, $\rho_n = \rho_n(f)$, and a transmission coefficient, $t_n = t_n(f)$. The reflection and transmission coefficients for each lossless surface are related by the consevation of energy equations.

$$|t_n|^2 + |\rho_n|^2 = 1.0 \tag{2.1}$$

and

$$t_n = 1.0 + \rho_n \tag{2.2}$$

When the front surface is illuminated by a normal incident electric field we may find the reflected field by summing all of the left traveling waves at the front surface (we assume that the distance "d" is large enough that the mutual coupling between the two surfaces is neglible (i.e. $d > \sim\lambda/4$)).

$$\begin{aligned} E^{ref} &= E^{inc}\rho_1 + E^{inc}t_1^2\rho_2 e^{-j2\beta d} + E^{inc}t_1^2\rho_2 e^{-j2\beta d}(\rho_1\rho_2 e^{-j2\beta d}) \\ &\quad + E^{inc}t_1^2\rho_2 e^{-j2\beta d}(\rho_1\rho_2 e^{-j2\beta d})^2 + \ldots \\ &= E^{inc}\rho_1 + E^{inc}t_1^2\rho_2 e^{-j2\beta d}\sum_{n=0}^{\infty}(\rho_1\rho_2 e^{-j2\beta d})^n \\ &= E^{inc}\rho_1 + \frac{E^{inc}t_1^2\rho_2 e^{-j2\beta d}}{1-\rho_1\rho_2 e^{-j2\beta d}} \\ &= E^{inc}\left[\frac{\rho_1 - \rho_2 e^{-j2\beta d}(\rho_1^2 - t_1^2)}{1-\rho_1\rho_2 e^{-j2\beta d}}\right] \end{aligned} \tag{2.3}$$

Using Equation (2.2) in Equation (2.3) we may define the reflection coefficient at the front of the double array surface.

$$\Gamma = \frac{E^{ref}}{E^{inc}} = \left[\frac{\rho_1 - \rho_2 e^{-j2\beta d}(\rho_1^2 - t_1^2)}{1-\rho_1\rho_2 e^{-j2\beta d}}\right] = \left[\frac{\rho_1 + \rho_2 e^{-j2\beta d}(1+2\rho_1)}{1-\rho_1\rho_2 e^{-j2\beta d}}\right] \tag{2.4}$$

Similarly, summing the right traveling waves to the right of second array yields the transmission coefficient at the rear of the double array surface.

$$\tau = \frac{E^{tran}}{E^{inc}} = \left[\frac{t_1 t_2 e^{-j\beta d}}{1-\rho_1\rho_2 e^{-j2\beta d}}\right] = \left[\frac{(1+\rho_1)(1+\rho_2)e^{-j\beta d}}{1-\rho_1\rho_2 e^{-j2\beta d}}\right] \tag{2.5}$$

We note in Equation (2.4) and (2.5) that there is a null in the reflection coefficient (corresponding to a perfect transmission region) every time the numerator of Equation (2.4) goes to 0. We refer to these nulls as "surface interference nulls". Physically, these nulls are created by the complete cancellation of all the left traveling wave in Figure 2.5 (In other words, the reflected signal is completely "phased out" and there is total transmission of the incident field.) We note further in Equation (2.4) that when the reflection coefficients ρ_1 and ρ_2 are constant, the "surface interaction nulls" occur periodically in the reflection coefficient. Now, when the reflection coefficients of two surfaces are identical (i.e. $\rho_1 = \rho_2 = \rho$) Equation (2.4) becomes:

$$\Gamma = \frac{E^{ref}}{E^{inc}} = \rho \left[\frac{1 + (2\rho + 1)e^{-j2\beta d}}{1 - \rho^2 e^{-j2\beta d}} \right] \tag{2.6}$$

From this equation we observe that for two identical, highly reflective arrays (i.e. $\rho \sim -1.0$) there will be perfect nulls in the reflection band every $f \sim (\frac{n}{2d})v$ where $n = 1, 2, 3...$, and v is the velocity of light in the material between the two surfaces. It is important to notice from Equation (2.6) that the bandwidth of the "surface interaction nulls" depends on the reflection coefficients of the surfaces ($\rho_1 = \rho_2 = \rho$). Specifically, as ρ approaches -1.0 the width of these nulls becomes infinitesmally narrow.

To further understand the implications of the above equations it is quite instructive to consider the equivalent circuit of two dipole arrays separated by a distance d as shown in Figure 2.6. We note that each dipole array is represented by a series LC-circuit placed in parallel in an equivalent transmission line. When the LC-circuit resonates it looks as a short circuit on

the transmission line. At this precise frequency the spacing d between the two arrays is immaterial since a short is a short! At frequencies below resonance the impedance of both arrays is going to be capacitive. However, if we take the impedance of array 2 and calculate this impedance as it appears at the position of array 1 due to the separation d, it will be inductive for some $d < \lambda/4$. When this inductance is combined in parallel with the capacitive impedance of array 1 a cancellation will take place and at some frequency a perfect null in the reflection band will occur (i.e. "surface interference null"). Similarly, if we increase the frequency, the array impedances will be inductive. If at this higher frequency the separation is $3\lambda/4 < d < \lambda$, array 2 will appear capacitive at array 1 and again a null in the reflection band will occur. There will obviously be more nulls at higher frequencies and for other values of d.

All of the above phenomenon are clearly demonstrated in Figure 2.7 which shows two identical type-3 "gangbuster half-surfaces" spaced a distance $d = 1.0$ cm and $d = 3.0$ cm apart in $\epsilon_r = 2.2$. The reflection coefficient for the type-3 "gangbuster surfaces" used is given in Figure 2.4. We note from Figure 2.7 how the "surface interference nulls" are dependent on the spacing "d", and how they become increasingly narrow as the reflection coefficient of the single "half-surface" approaches -1.0 (i.e. the array approachs resonance).

To this point, we have considered only the interaction of two arrays with a separation "d" at normal angle of incidence. When the angle of incidence becomes oblique we are reminded that the actual electrical length of this

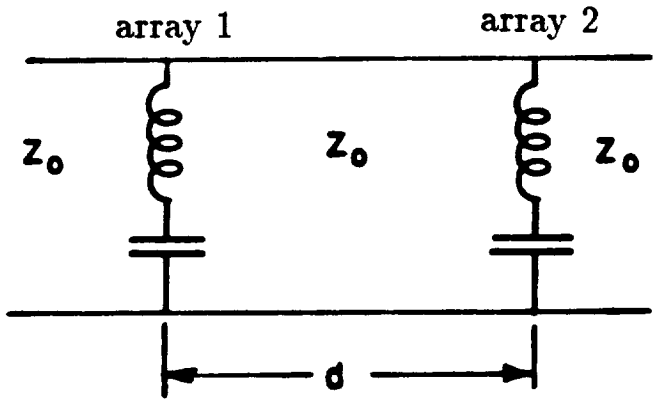

Figure 2.6: The equivalent circuit for two dipole arrays separated by a dielectric slab of thickness d.

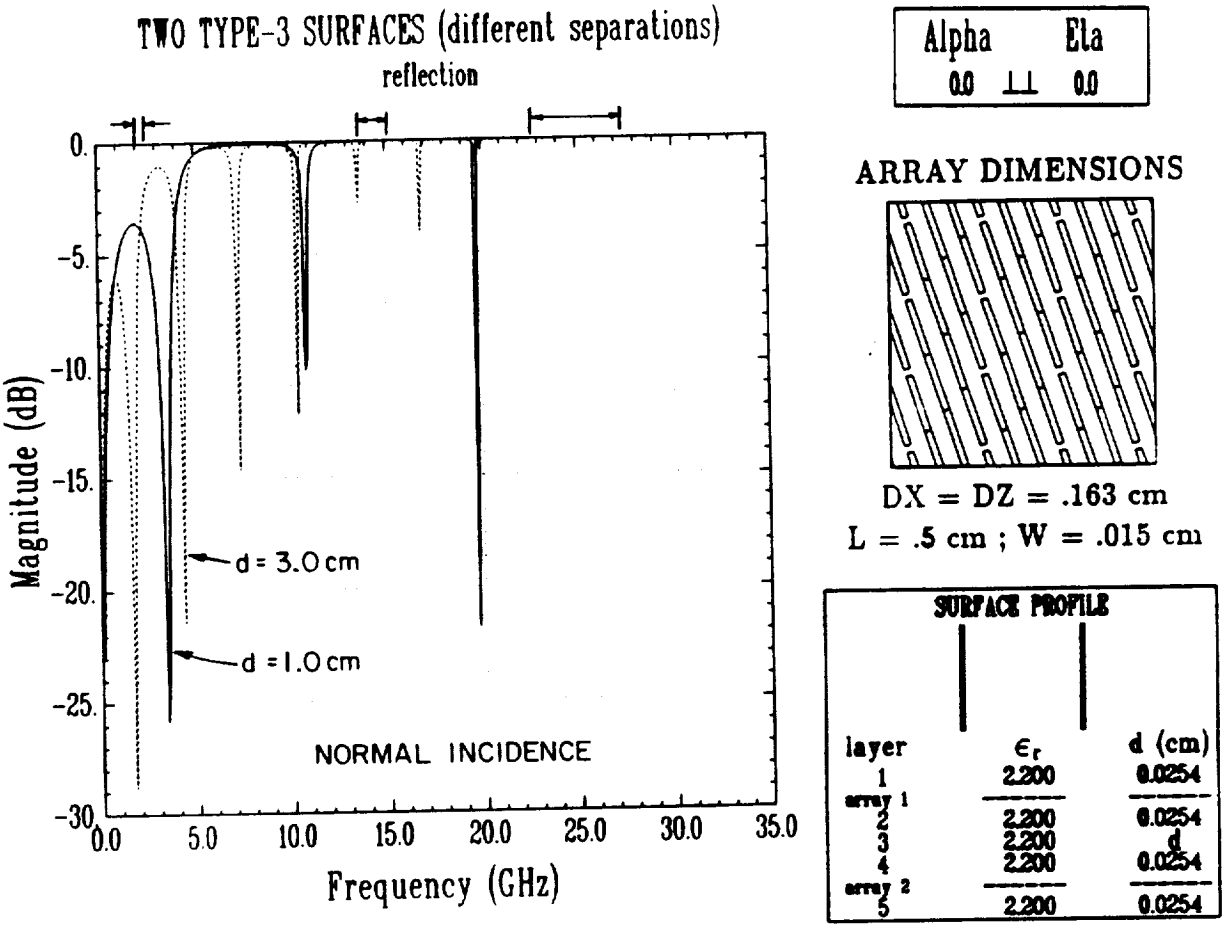

Figure 2.7: Two identical type-3 "gangbuster half-surfaces" separated by a distance "d"=1.0 cm and 3.0 cm in $\epsilon_r = 2.2$.

separation is $\beta d \cos\eta$, where β is the propagation constant in the particular dielectric medium, and η is the direction of the incident field in the medium. Thus, the "surface interference nulls" observed before will move toward a higher frequency as the angle is increased. We would, however, expect this variance to be reduced with a higher dielectric constant since the angle η would be reduced in accordance with Snell's Law. The disadvantage of using large dielectric constants is that high dielectrics cause the level below the lowest null to become greater.

For our design we chose separation distance $d = 1.95$ cm in $\epsilon_r = 2.2$. The reflection coefficient for this separation is shown in Figure 2.8 for 0-35 GHz, at normal angle of incidence and at $\eta = 45°$ in the E and H-planes. A close-up of this reflection coefficient from 12.0-17.0 GHz is shown in Figure 2.9 and close-up of the transmission coefficient from 1.0-3.0 GHz is shown in Figure 2.10. We notice that while the spacing $d = 1.95$ cm causes the the transmission region to be slightly high ($\sim 2.2 - 2.5$ GHz), it does avoid sizable "surface interference nulls" in the Ku-reflection band for all angles of incidence out to $\eta = 45°$ in both the E and H-planes.

2.2.2 Double Array Dichroic Surface with a Matching Plate

In the previous section we used the interaction of two single array surfaces to form a double array surface. We saw that inorder to keep the Ku-reflection band free from "surface interference nulls" for all angles of incidence out to $\eta = 45°$ we needed an separation distance of $d = 1.95$ cm in $\epsilon = 2.2$. This distance did not, unfortunately, produce the required S-band transmission

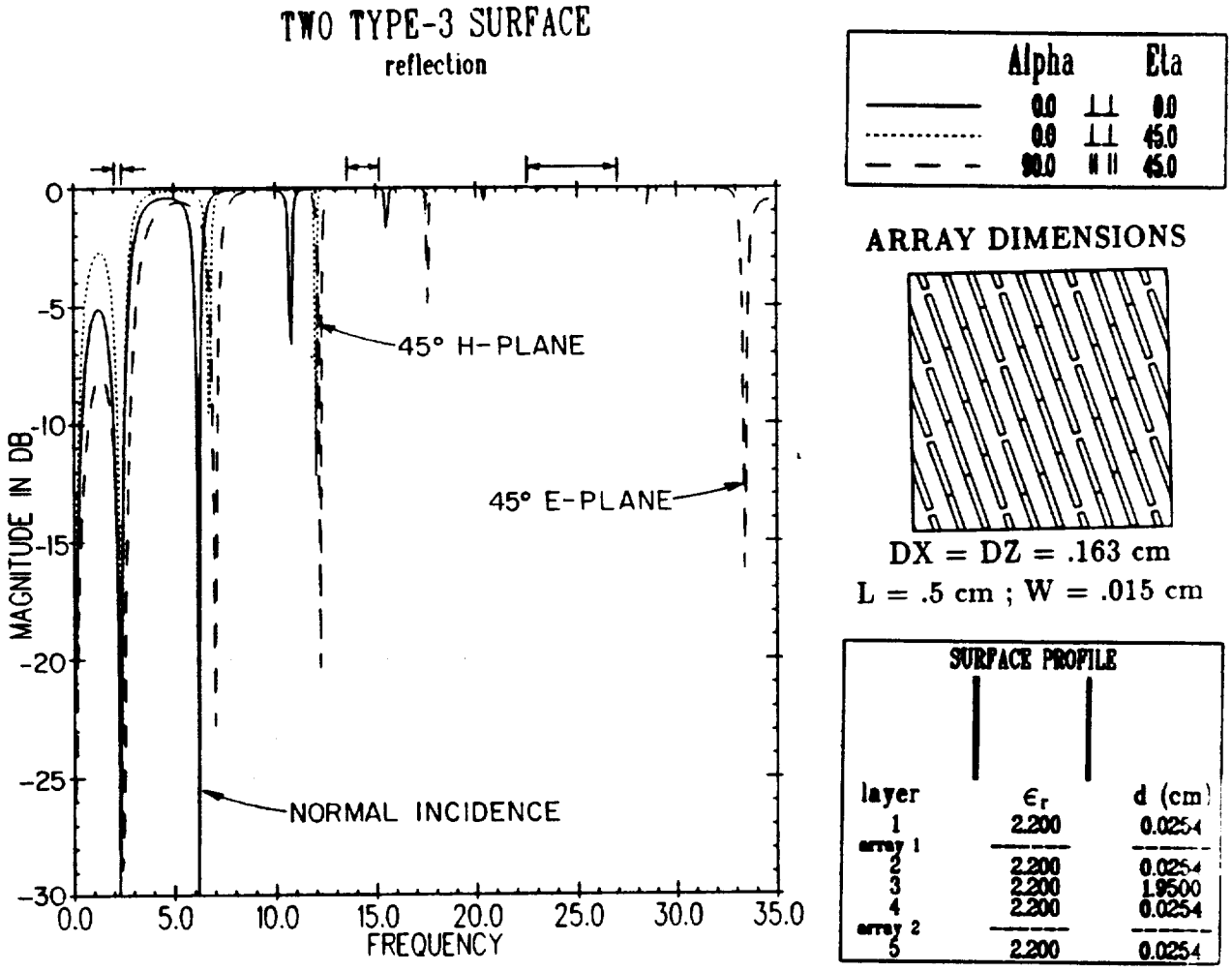

Figure 2.8: The reflection coefficient curves for a double array design with a separation distance $d = 1.95$ cm in $\epsilon_r = 2.2$ for $f = 0 - 35$ GHz.

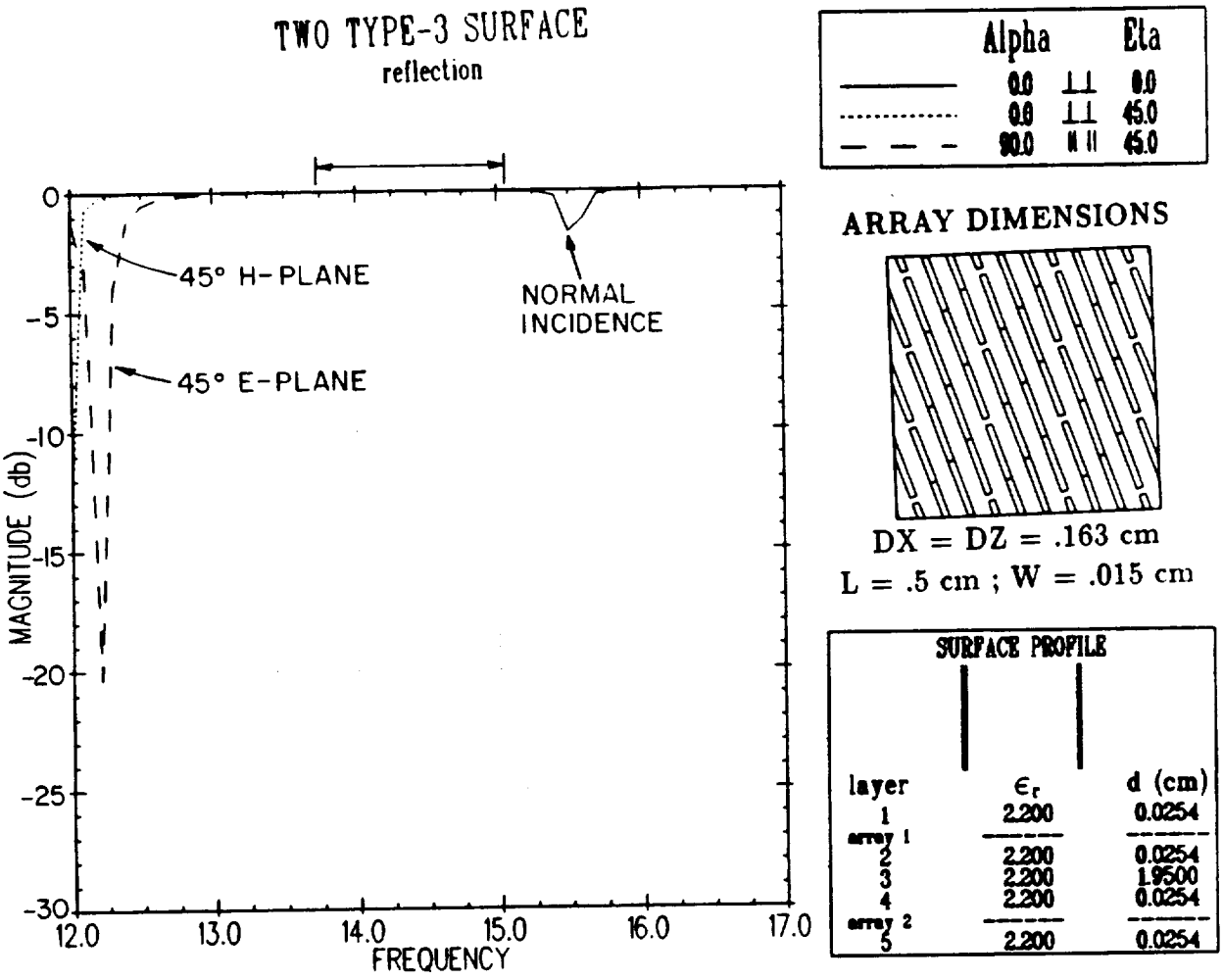

Figure 2.9: The reflection coefficient curves for a double array design with a separation distance $d = 1.95$ cm in $\epsilon_r = 2.2$ for $f = 12.0 - 17.0$ GHz.

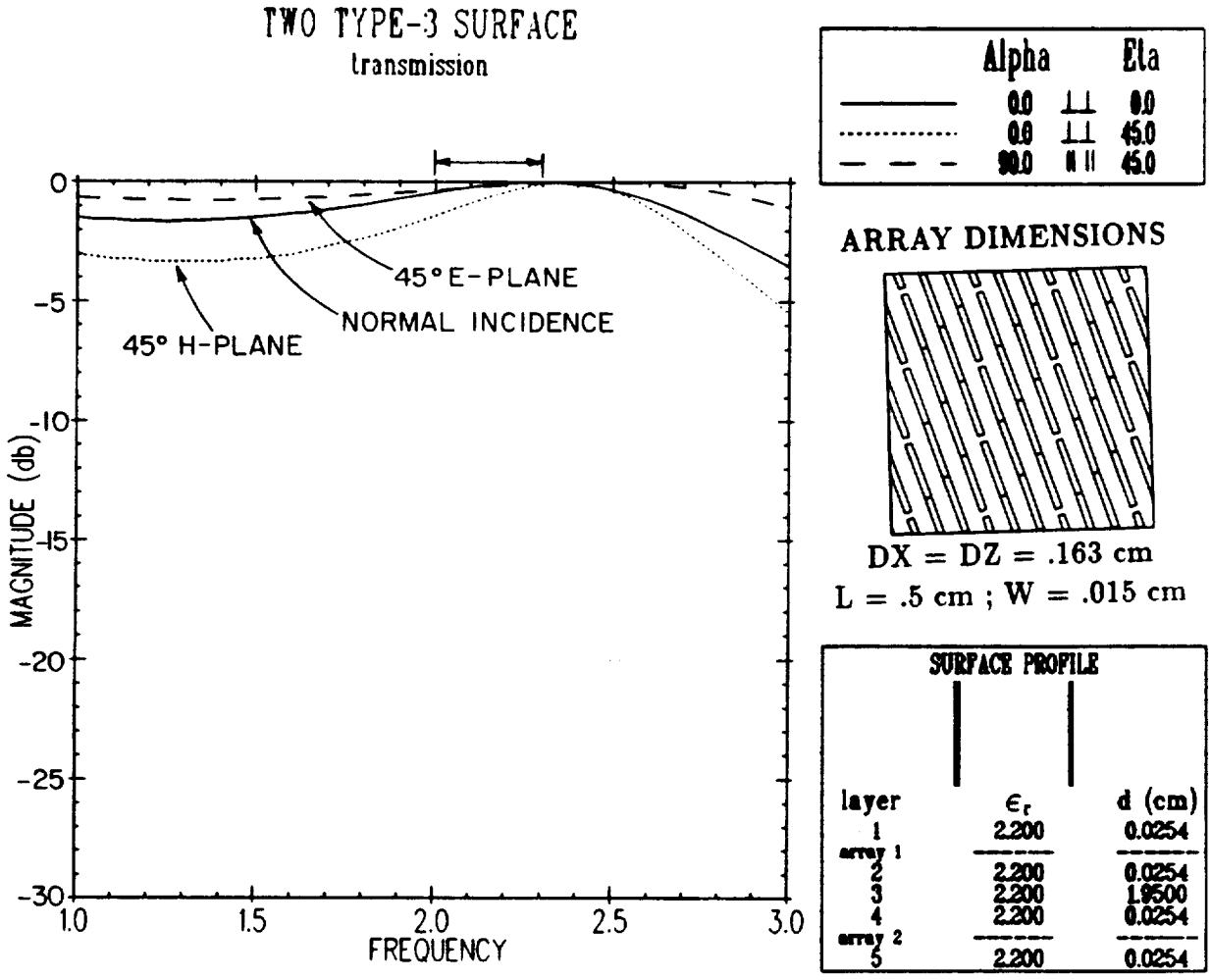

Figure 2.10: The transmission coefficient curves for a double array design with a separation distance $d = 1.95$ cm in $\epsilon_r = 2.2$ for $f = 1.0 - 3.0$ GHz.

region. To enhance the transmission region of this double array surface we added a dielectric slab combination which was designed using simple matching principles. We refer to these added dielectric slabs as a "dielectric matching plate".

Figure 2.11 shows the reflection coefficient for this double array dichroic surface with a matching plate in the frequency range 0-35 GHz, with angles of incidence $\eta = 0°$, and $\eta = 45°$ in the E- and H-planes. The pertinent dimensions of the surface and the matching plate are shown in the figure insert. Next, Figures 2.12 and 2.13 show the transmission and reflection coefficient, respectively, in the range 1.0-3.0 GHz. Finally, Figures 2.14 and 2.15 show expanded views of the reflection coefficient in the ranges 12.0-17.0 GHz and 20.0-30.0 GHz.

Comparing the transmission coefficient curve of Figure 2.12 and that of Figure 2.10 we note that the matching plate creates the required transmission region in S-band from 2.0-2.3 GHz. Comparing the reflection curves in Figures 2.11, 2.14, 2.15, with those of Figures 2.8 and 2.9 demonstrates that the reflection coefficient in the Ku and Ka-reflection bands are virtually uneffected by the matching plate. This result is not totally unexpected since we know from transmission line theory that "a short is a short".

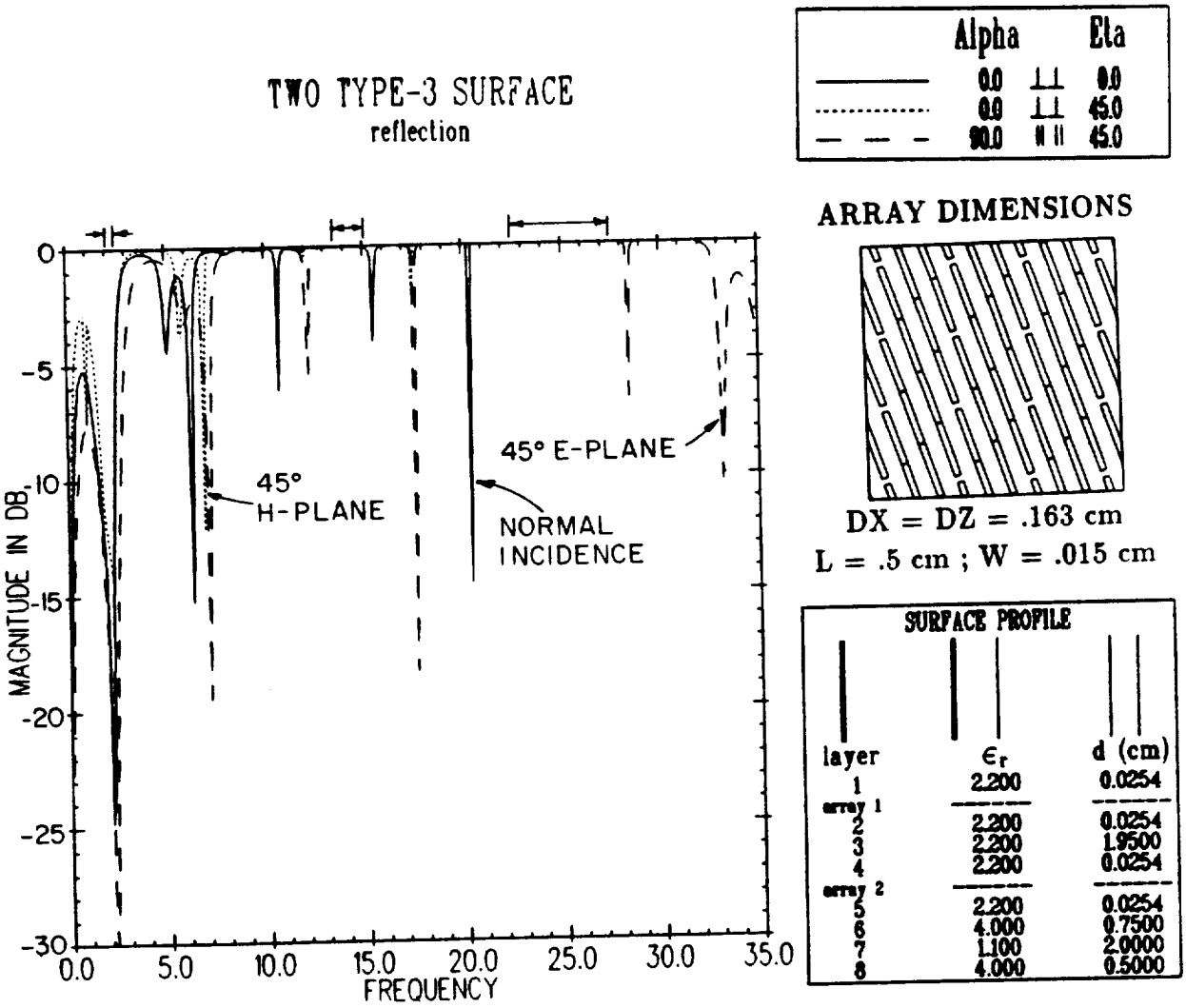

Figure 2.11: The reflection coefficient curves for a double array design with a matching plate in the range $f = 0 - 35$ GHz for $\eta = 0°$ (normal) and $\eta = 45°$ in the E- and H-plane.

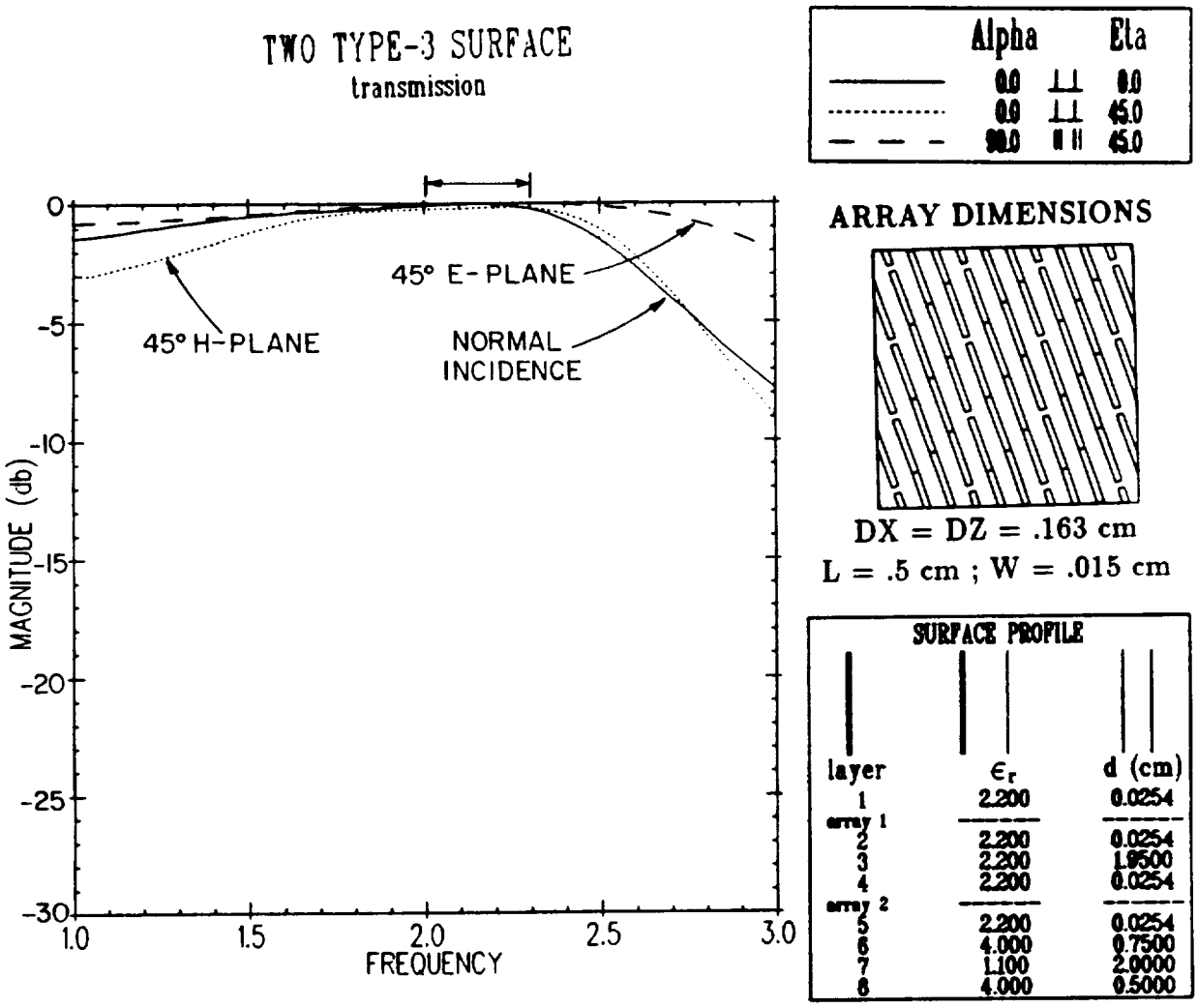

Figure 2.12: The transmission coefficient curves for a double array design with a matching plate in the range $f = 1.0 - 3.0$ GHz for $\eta = 0°$ (normal) and $\eta = 45°$ in the E- and H-plane.

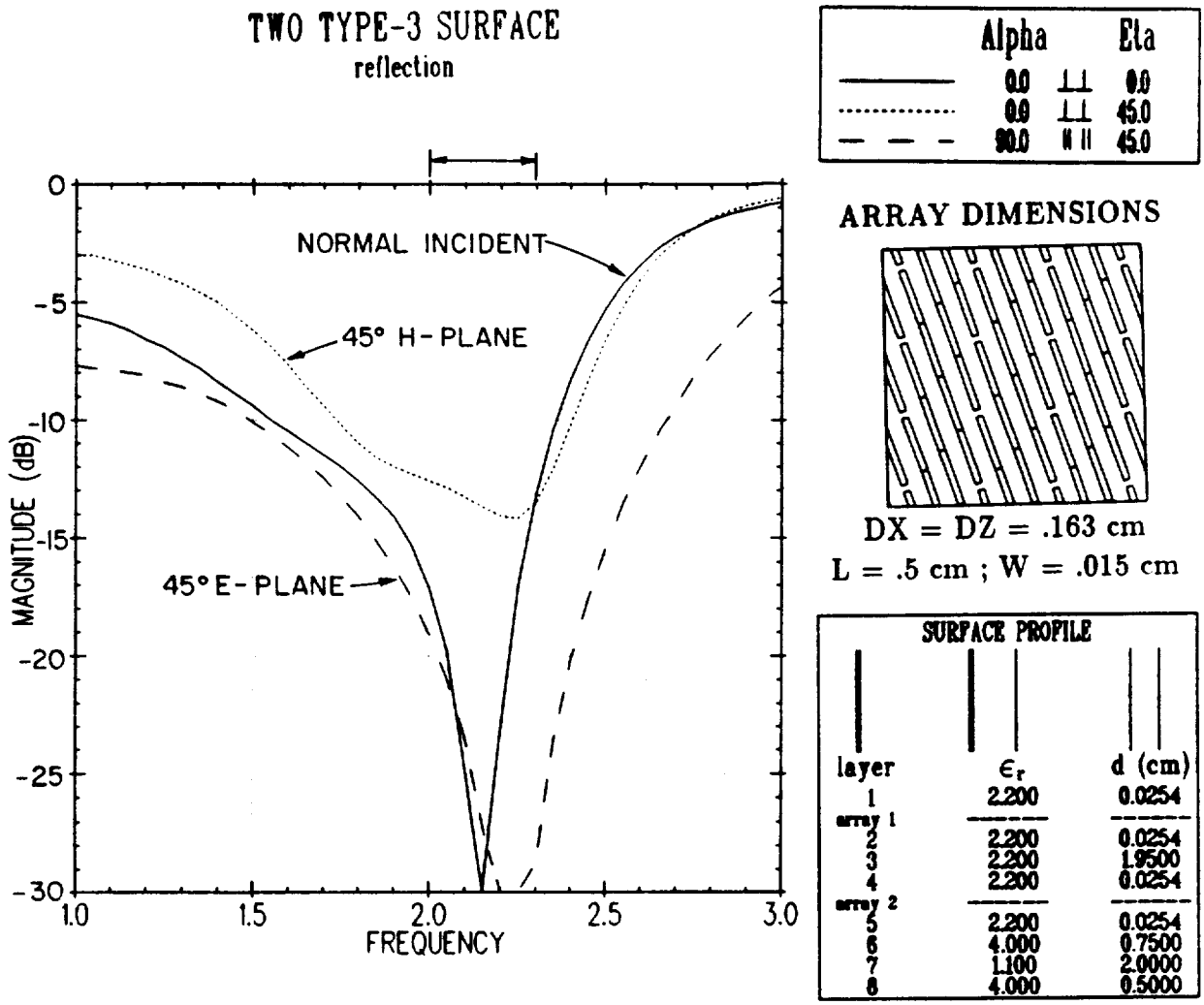

Figure 2.13: The reflection coefficient curves for a double array design with a matching plate in the range $f = 1.0 - 3.0$ GHz for $\eta = 0°$ (normal) and $\eta = 45°$ in the E- and H-plane.

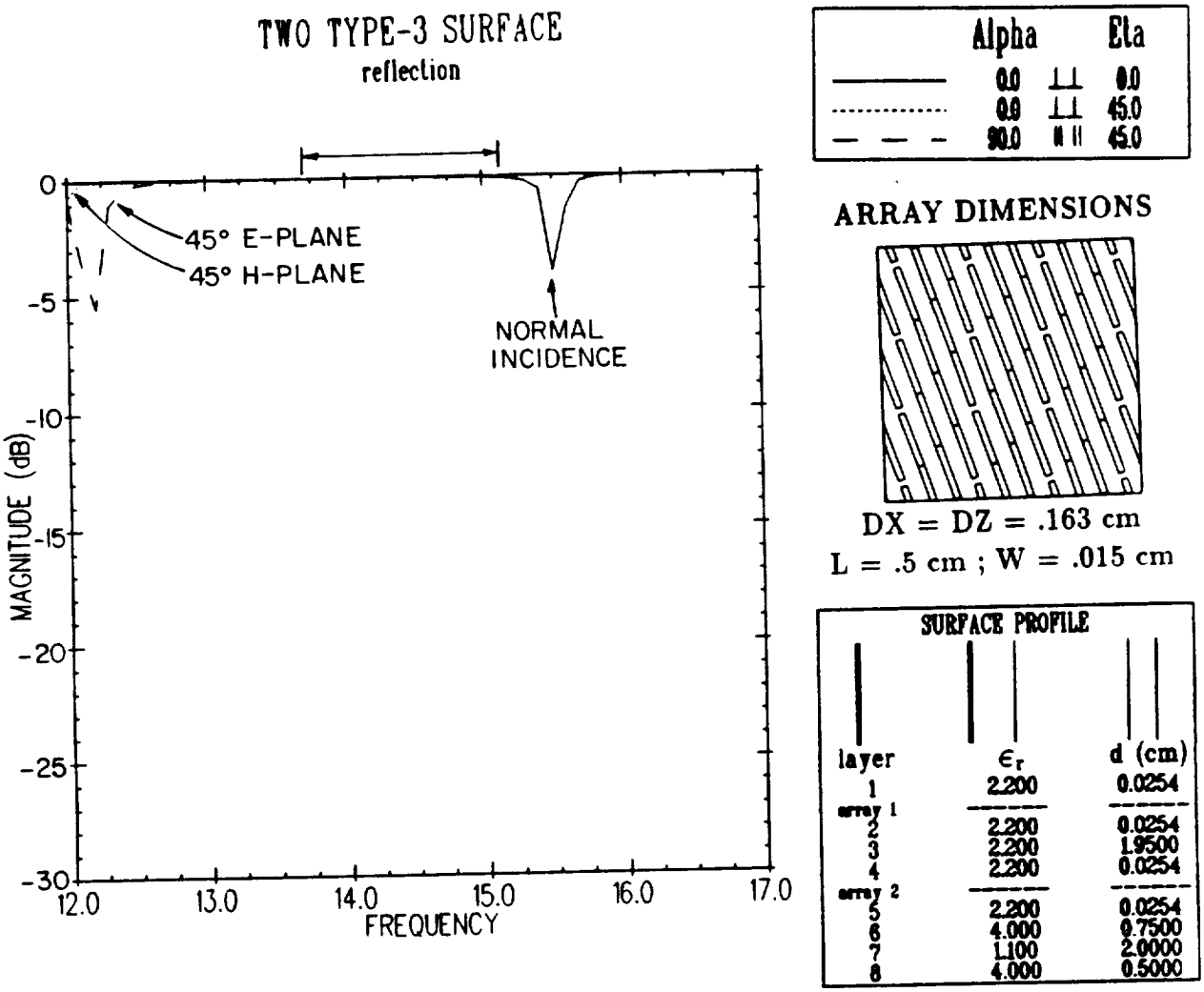

Figure 2.14: The reflection coefficient curves for a double array design with a matching plate in the range $f = 12.0 - 17.0$ GHz for $\eta = 0°$ (normal) and $\eta = 45°$ in the E- and H-plane.

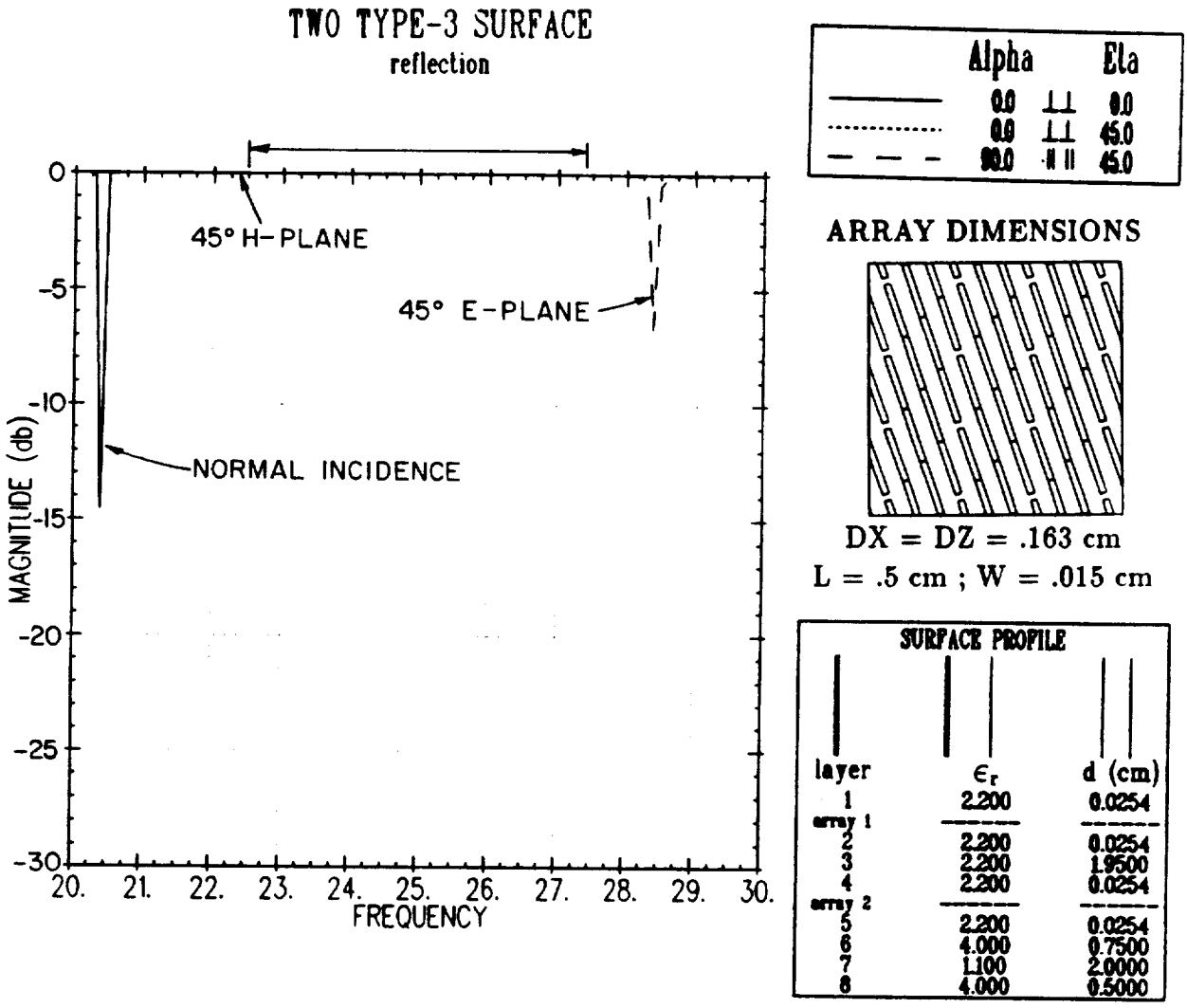

Figure 2.15: The reflection coefficient curves for a double array design with a matching plate in the range $f = 20.0 - 30.0$ GHz for $\eta = 0°$ (normal) and $\eta = 45°$ in the E- and H-plane.

Chapter 3

Losses in Dichroic Surfaces

In the previous chapter we concentrated on the design of a dichroic surface whose parallel polarized component is transparent at S-band (2.0-2.3 GHz) and reflective in Ku-band and Ka-band (13.7-15.1 GHz and 22.5-27.3 GHz respectively). To fulfill this requirement we formulated a design consisting of two lossless type-3 "gangbuster half surfaces" embedded in lossless dielectrics and enhanced by a lossless dielectric matching plate. This chapter examines the effect of loss, both dielectric and copper, on this somewhat idealized design.

3.1 Dielectric Loss in the Dichroic Surface Design

3.1.1 Loss as a Function of Dielectric Loss Tangent

We begin our study of dielectric loss in dichroic surfaces by comparing the various reflection and transmission coefficients, at normal angle of incidence, for the dielectric loss tangents = 0.0, 0.001, 0.01, and 0.1. We show

in Figure 3.1 the parallel reflection coefficient in the frequency range 0-35 GHz. Next, we show in Figure 3.2 the parallel transmission coefficient in the frequency range 0-8 GHz (this region includes our S-band transmission region, i.e. 2.0-2.3 GHz). Finally, we show in Figure 3.3 the parallel reflection coefficient in the frequency range 12-17 GHz (this region includes our Ku-band reflection region, i.e. 13.7-15.1 GHz).

We note from Figures 3.1 and 3.2 that while the reflection coefficient in the S-band is not significantly changed by an increase in the loss tangent, the transmission coefficient is drastically altered. This is because the front array dominates the reflection so that most of the reflected field need only pass through the thin lossy dielectric substrate. Conversely, the transmitted field must traverse all of the lossy materials.

Examination of the reflection band null (at 15.5 GHz) in Figure 3.3 shows an interesting feature of the dichroic surface, namely, around 15.5 GHz we find a region where the loss tan = 0.1 case is more reflective than the lossless case. This is simply because that null is a "surface interference null" which is caused by the complete cancellation of the infinite number of left traveling waves that comprise the reflected field (this was describes thoughly in the last chapter). When we introduce a lossy material between the plates, a full cancellation of these fields cannot take place, and the deep null in the reflection band is removed.

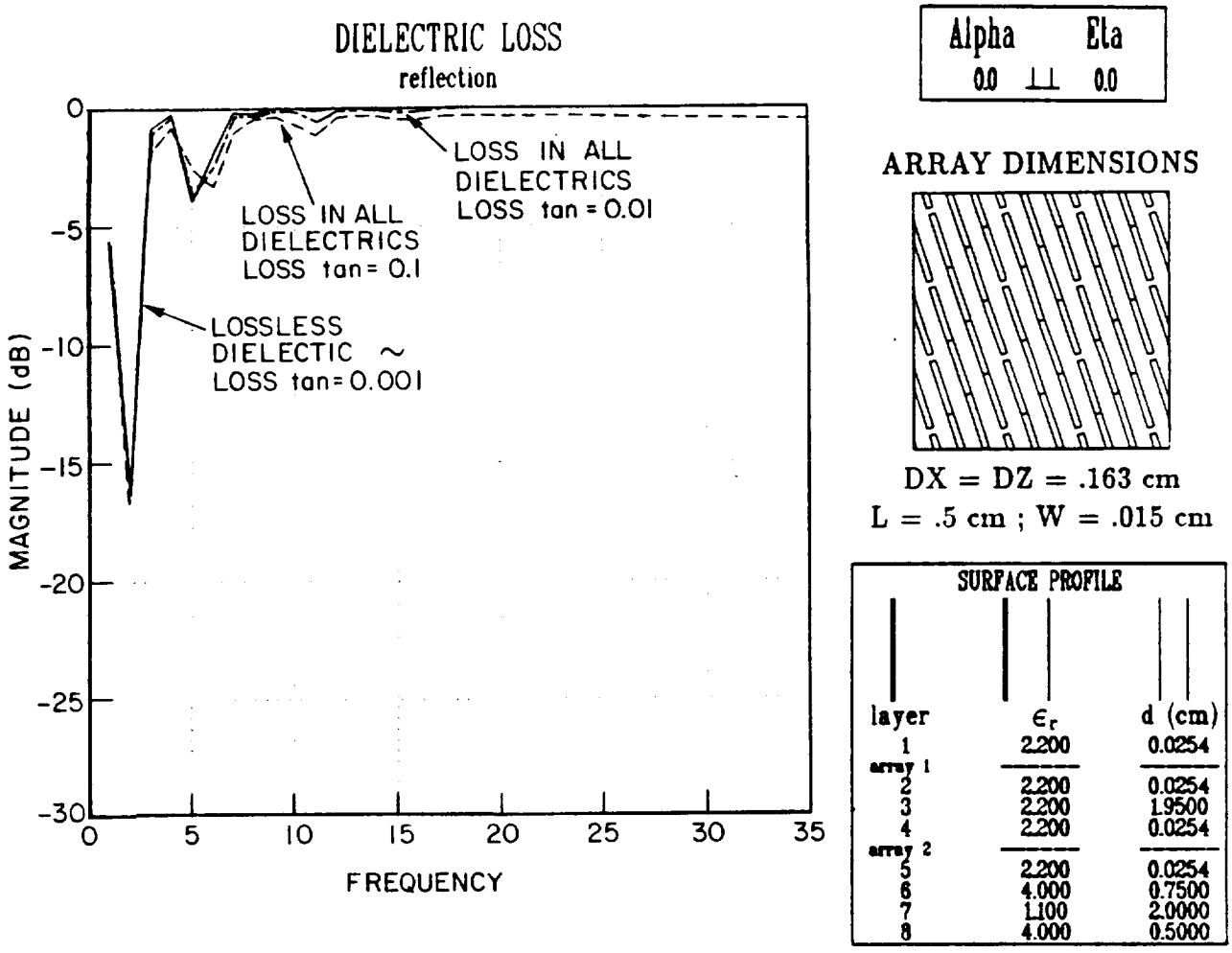

Figure 3.1: The parallel reflection coefficient curve as a function of frequency for normal angle of incidence and in the plane of the elements. Parameter is the dielectric loss tangent.

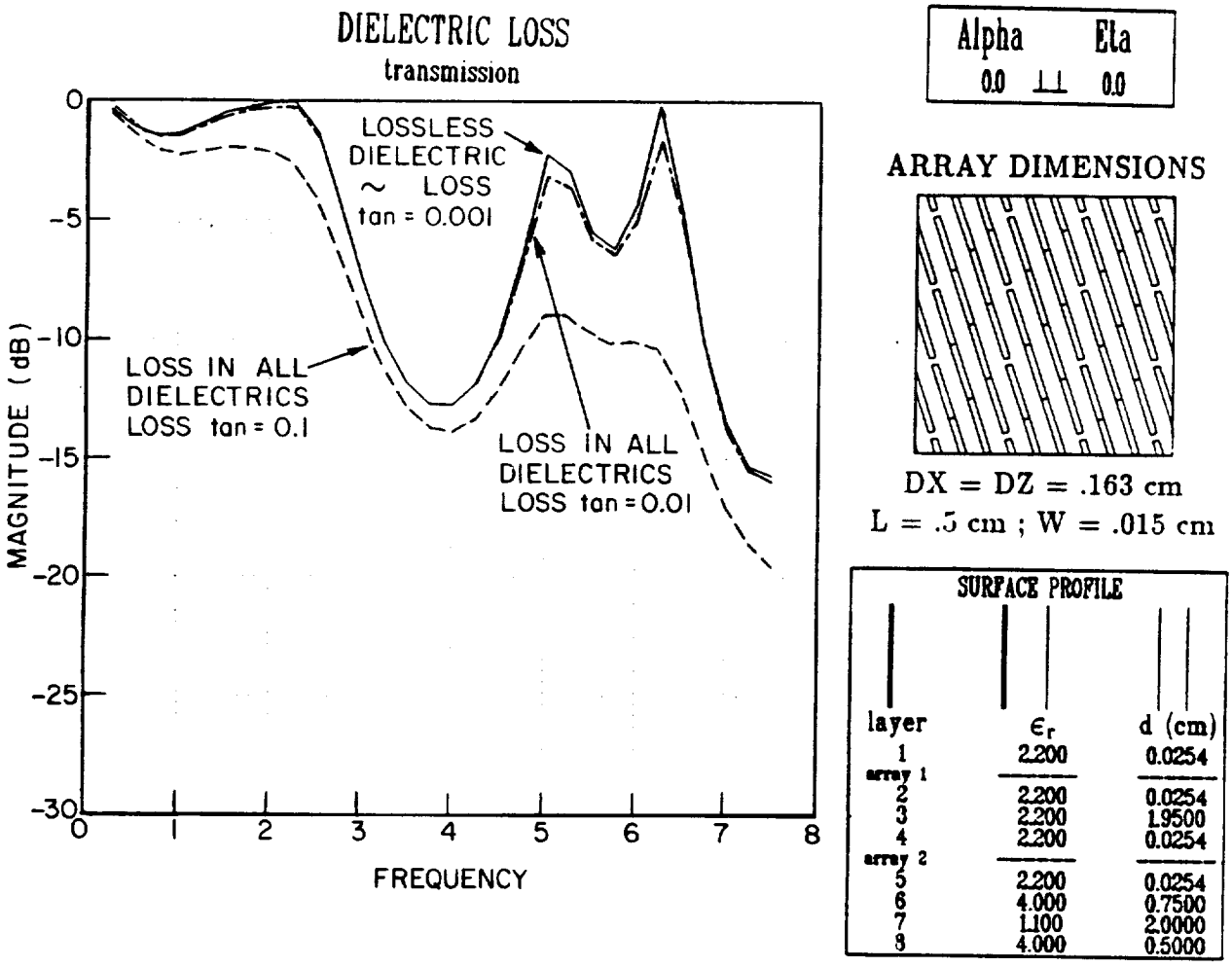

Figure 3.2: The parallel transmission coefficient curve as a function of frequency (including the S-band transmission region from 2.0-2.3 GHz) for normal angle of incidence and in the plane of the elements. Parameter is the dielectric loss tangent.

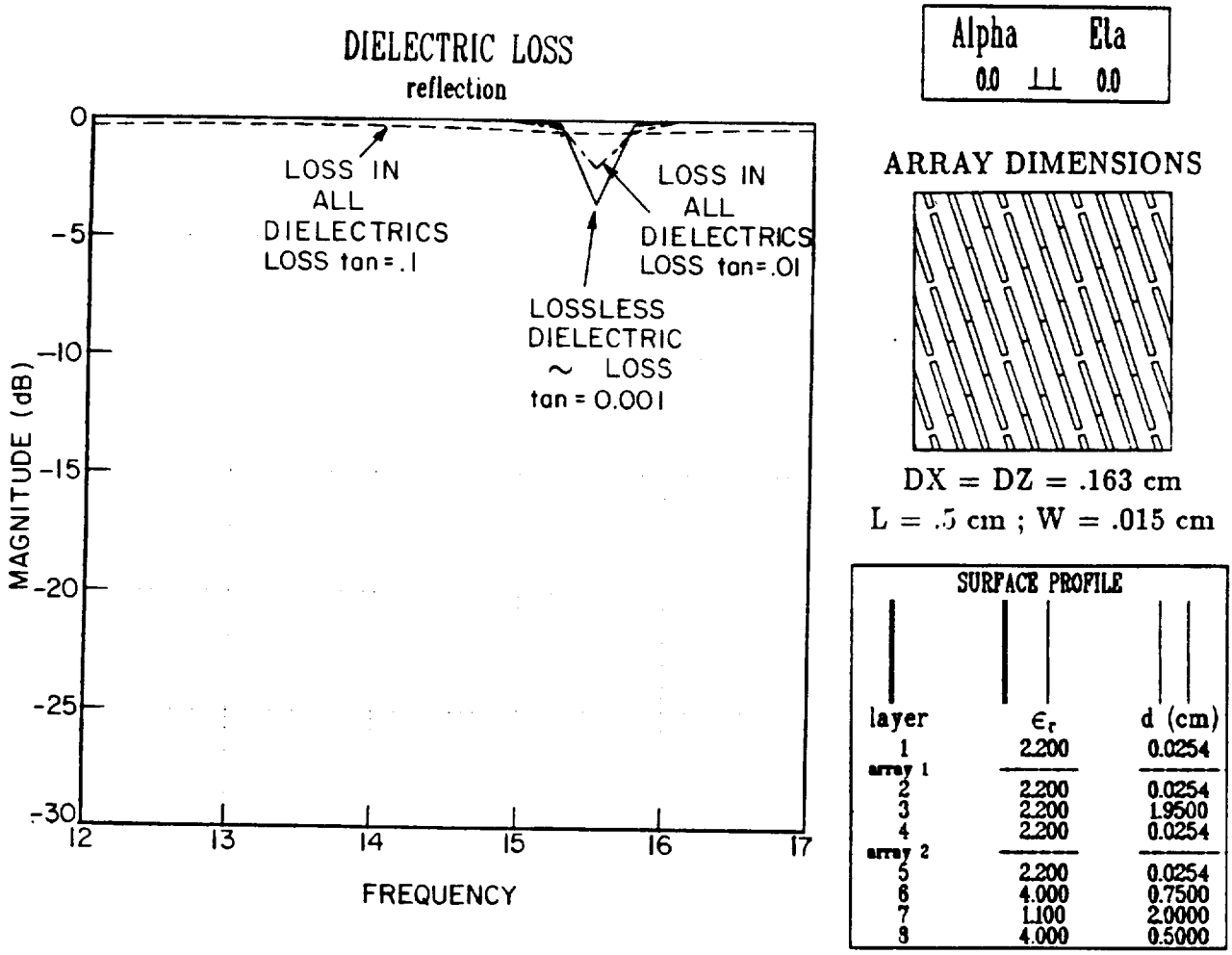

Figure 3.3: The parallel reflection coefficient curve as a function of frequency (including the Ku-band reflection region from 13.7-15.1 GHz) for normal angle of incidence and in the plane of elements. Parameter is the dielectric loss tangent.

3.1.2 Effect of the Location of Lossy Dielectric Materials

In order to obtain a deeper understanding of dielectric loss in our dichroic surface design, we consider how the location of lossy materials effects the reflection and transmission coefficients of the surface. Specifically, we wish to determine whether a lossy dielectric material in the proximity of the array elements has a greater influence on the surface characteristics than a lossy dielectric located further away. To this end, we show in Figures 3.4 and 3.5 the reflection and transmission coefficients in the Ku-band, at normal angle of incidence for: the lossless case, the loss in the substrate only case, the loss in all but substrate case, and the loss in all dielectrics case. Extremely lossy dielectrics (loss tan=0.1) were used in the calculations to clearly show the differences in the curves.

From Figure 3.4 we note that although the dielectric substrate is only $\sim 1/50th$ the electrical length of the other dielectrics it accounts for almost half of the reflection loss. This high percentage of loss in the substrate is due to primarily two reasons. The first is that, as mentioned in the last section, the front array of this dichroic surface reflects most of the incident field thus allowing only a small percentage of the field to propagate through the rest of the lossy materials. The second is that the field away from the array elements is comprised of only a single propagating wave (for no grating lobes) while the field near the scatterers is highly concentrated and consists of both the propagating wave and an infinte number of evanescent waves. The highly concentrated fields around the elements will therefore have a greater amount of loss.

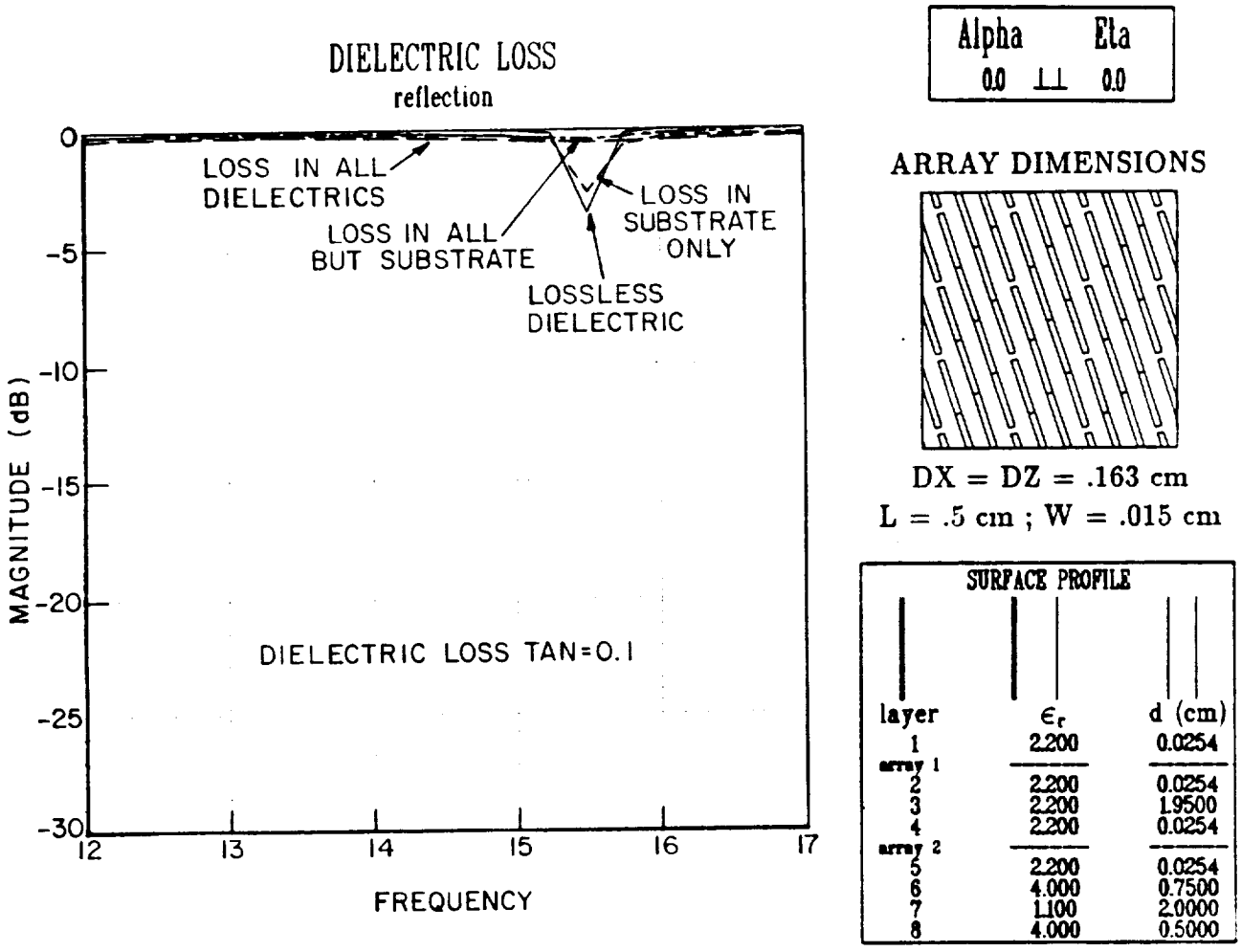

Figure 3.4: The parallel reflection coefficient curves as a function of frequency (in the Ku-band) for normal angle of incidence. Parameter is the location of the lossy dielectric material in the design.

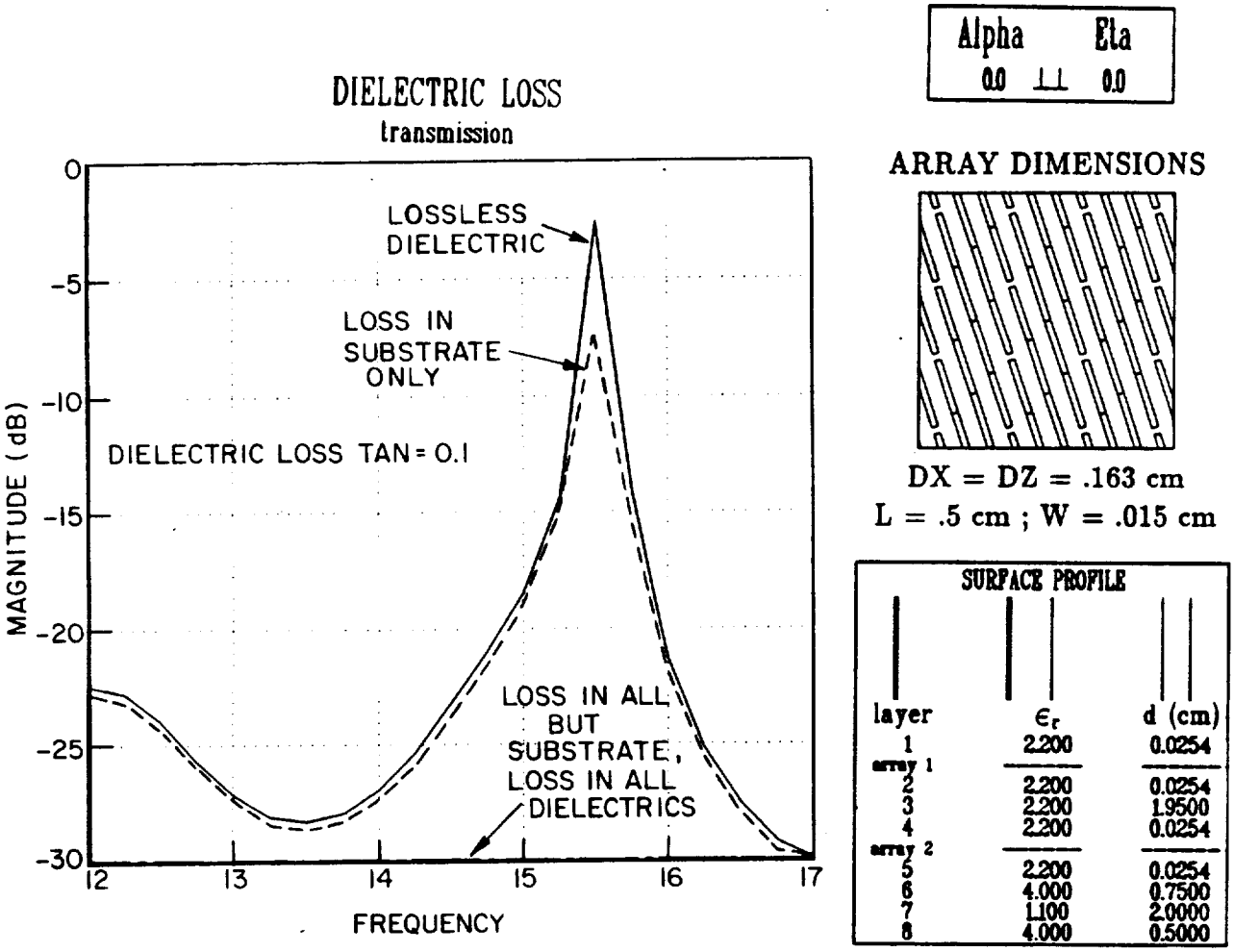

Figure 3.5: The parallel transmission coefficient curves as a function of frequency (in the Ku-band) for normal angle of incidence. Parameter is the location of the lossy dielectric material in the design.

From the transmission curve of Figure 3.5 we note that loss in the parallel transmitted component will be dominated by the attenuation in the dielectric spacer and matching plate because of their large electrical length in this frequency range. We note however, that the loss at lower frequencies with be proportionally smaller due to their smaller electrical length.

3.1.3 Effect of Dielectric Loss when the Field is Incident on the Array Side vs. Matching Plate Side

In Chapter 2 we considered only lossless elements embedded in lossless dielectrics. Under these conditions (and with the added condition that the cross polarization is zero, which is the case when considering the principal planes and normal angle of incidence) the parallel reflection and transmission properties of the dichroic surface design are independent of which side the field is incident on. That is, a field incident on the matching plate side (*dark side*), or the array side (*sunny side*) produce exactly the same parallel reflection and transmission curves. This assumption cannot be made when we are dealing with lossy dielectrics.

Consider our dichroic surface design with a very large dielectric loss tangent=0.1. Figure 3.6 and 3.7 show the parallel reflection and transmission coefficient for this lossy design with the field incident on both the array side and the matching plate side (normal angle of incidence). In Figure 3.6 we observe a huge difference in the reflection coefficients of the two cases. This is simply because in the sunny side case most of the reflected field does not

make the round trip path through all of the lossy matching plate dielectrics. The transmission coefficients of Figure 3.7 are equal in both cases since the transmitted field must always traverse the entire lossy surface.

3.2 Conduction Loss in the Dichroic Surface Design

We finally consider the effect of non-perfect conducting elements on our dichroic surface design. To determine this effect we assume that the skewed dipole elements are made of copper that has a conductivity of $\sigma = 58\ M\mho m^{-1}$. Using this and the fact that at high frequencies the current is confined to a very thin layer at the surface of the copper, δ (called the $1/e$ depth of penetration), we can define a *skin resistance* R_s as:

$$R_s = 1/\sigma\delta \quad \Omega/\square \tag{3.1}$$

where

$$\delta = 1/\sqrt{f\pi\mu\sigma} \quad m \tag{3.2}$$

As an upper limit of the copper losses we find the skin resistance at 30 GHz from Equation (3.1) to be $R_s = .045\ \Omega/\square$. The parallel reflection coefficient for this case and the lossless case are shown in Figure 3.8. It is obvious from this figure that the copper loss in our design is negligible.

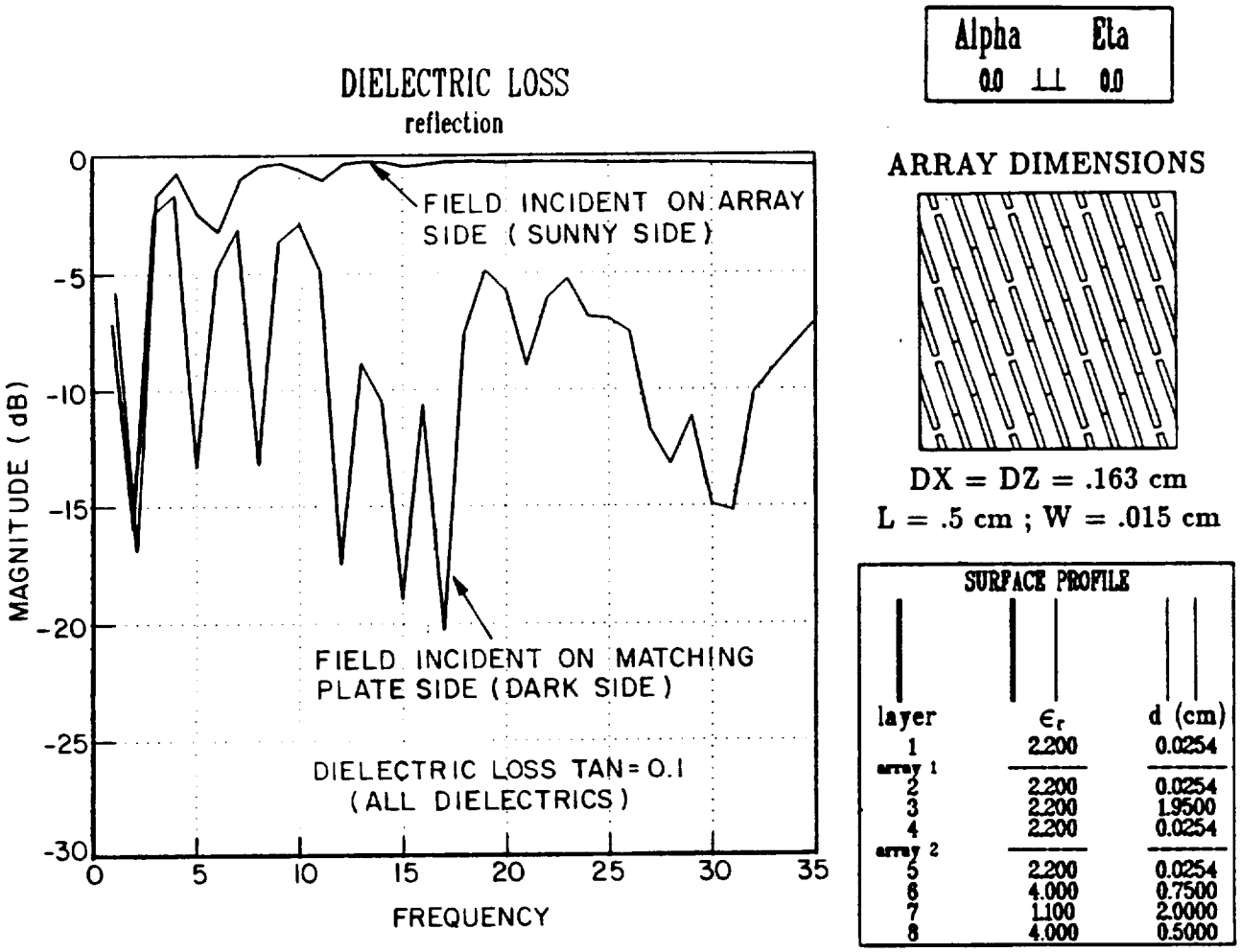

Figure 3.6: The parallel reflection coefficient curve as a function of frequency at normal angle of incidence for the field incident on the array side and the matching plate side.

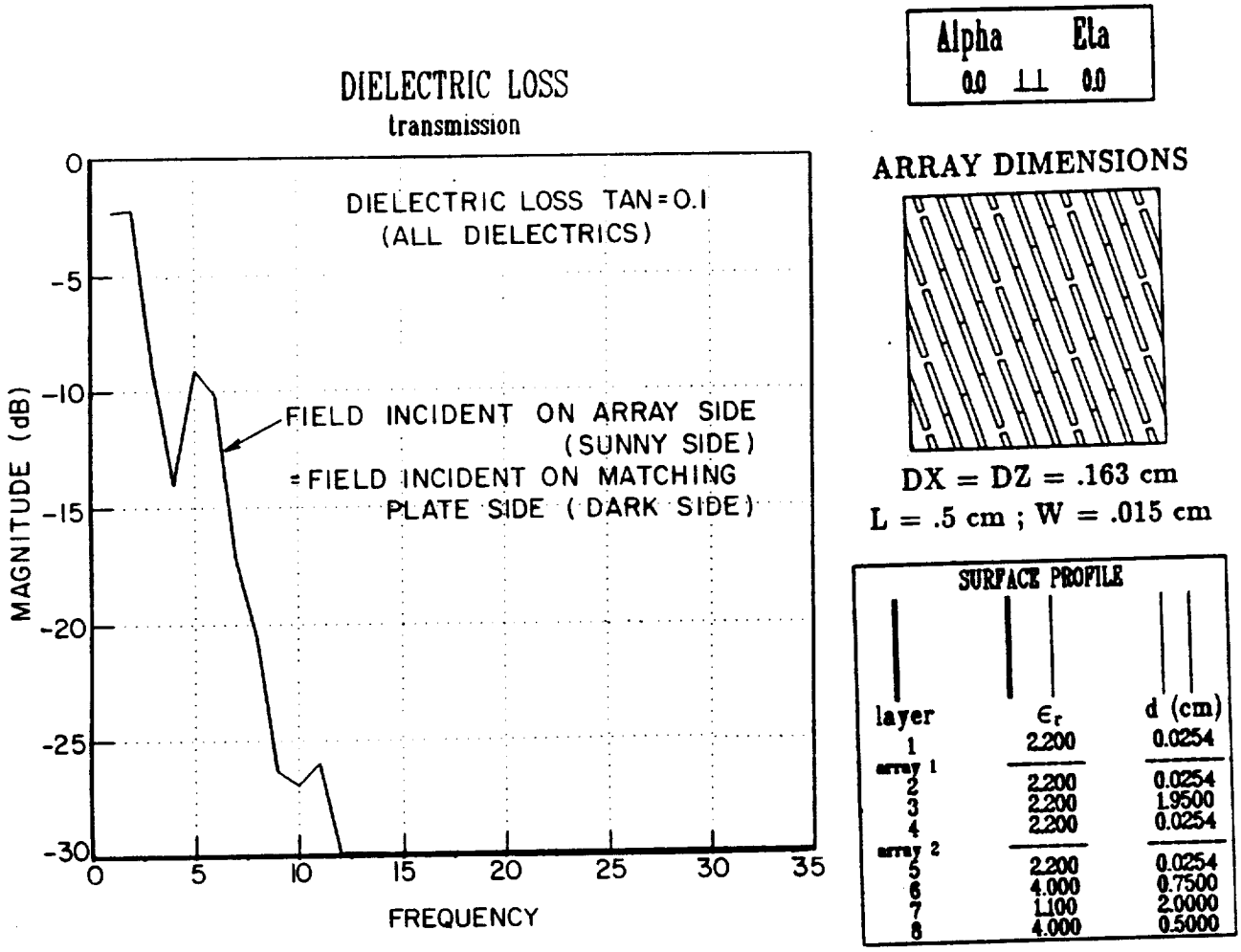

Figure 3.7: The parallel transmission coefficient curve as a function of frequency at normal angle of incidence for the field incident on the array side and the matching plate side.

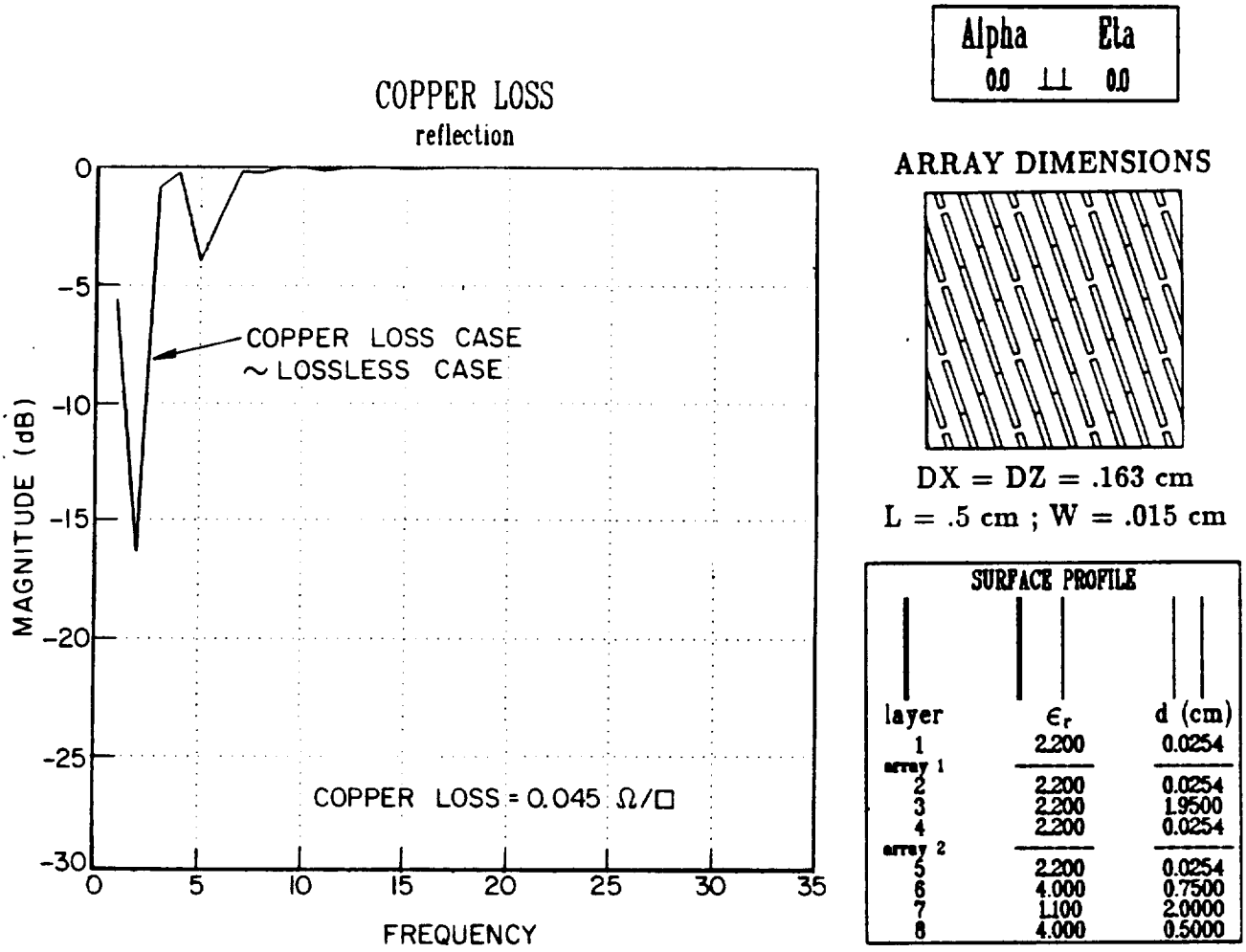

Figure 3.8: Parallel reflection coefficient curves (lossless case and for copper loss = .045 $\Omega/\square$) as a function of frequency for normal angle of incidence and in the plane of the elements.

Chapter 4

Cross Polarization in "Gangbuster Whole-Surface" Designs

So far in this report we have considered a dichroic surface design consisting of two parallel "gangbuster half-surfaces" separated by a thickness of dielectric "*d*", and enhanced with a dielectric matching plate. It was noted in Chapter 1 that these "half-surfaces" can handle only the polarization with the E-vector in the plane of the conducting elements. In this chapter these "half-surfaces" are replaced by "gangbuster whole-surfaces". The second orthogonal array of the "whole-surface" allows the design to handle any arbitrary plane of incidence. However it introduces a mean of producing a cross polarized field component. This chapter considers the cross polarization in "gangbuster whole surfaces".

4.1 Cross Polarizarion Characteristics of Single "Gangbuster Whole-Surfaces"

We begin our study of cross polarization by considering a single "gangbuster whole-surface". Recall from Figure 1.1b that the "gangbuster whole-surface" is comprised of two arrays of straight skewed dipoles ("half-surfaces"), rotated 90° with respect to each other, and spaced an array separation distance "s" apart. Examination of the geometry of these surfaces indicates that not only should cross polarization be dependent on angle and plane of incidence, but also on the separation distance "s" and the array registration (i.e. the relative position of the orthogonal elements to each other). These factors are discussed below.

4.1.1 Cross Polarization in "Whole-Surfaces" as a Function of Angle and Plane of Incidence

In this section we will investigate the reflected and transmitted signal for the type-3 "gangbuster whole-surface" as a function of angle and plane of incidence. All calculations here are performed with 5 mil separation between the two orthogonal "half-surfaces". We consider first the case where the plane of incidence is parallel with the elements of one of the arrays. This case occurs at $\alpha = 0°$ and is called the "aligned" case. The parallel reflection and transmission curves for the aligned plane of incidence with the two extreme angles of incidence, namely $\eta = 0°$ (normal) and $\eta = 45°$, are shown in Figure 4.1 and Figure 4.2, respectively. We show further, the cross polarized reflection ($R_{\perp\parallel}$ and $R_{\parallel\perp}$) and tranmission ($T_{\perp\parallel}$ and $T_{\parallel\perp}$)

coefficient curves in Figures 4.3 and 4.4 for the same angles of incidence. We note from these figures a strong increase in the cross polarization levels with increased angle of incidence, and increased frequency. We note too that the cross polarized reflection and transmission coefficients have equal magnitudes (i.e. $R_{\|\perp} = T\|\perp$).

We now consider the plane of incidence that is rotated $\alpha = 22.5°$ away from the elements of one "half-surface". Figures 4.5 and 4.6 show the parallel reflection and transmission coefficients in this plane for angles of incidence $\eta = 0°$ and $\eta = 45°$. The cross polarized reflection and transmission coefficient are shown in Figures 4.7 and 4.8. We note that again the cross polarization level increases with angle of incidence and frequency. However, we now note that the reflection and transmission cross polarization coefficients are not equal (i.e. $R_{\|\perp} \neq T\|\perp$). This feature will be discussed later.

We finally consider the plane of incidence that bisects the two orthogonal "half-surfaces" ($\alpha = 45°$). The parallel reflection and transmission coefficients for this "bisecting" case, at $\eta = 0°$ and $\eta = 45°$ angles of incidence, are shown in Figures 4.9 and 4.10. The cross polarized reflection and transmission coefficients are shown in Figures 4.11 and 4.12. The $\alpha = 45°$ case does not differ much from the $\alpha = 22.5°$ case. We note again that,in general, $R_{\|\perp} \neq T_{\|\perp}$ for $\alpha \neq 0°$ or $\alpha \neq 90°$. This is seen by inspection of Figure 4.13 as explained below.

Consider two orthogonal arrays of straight dipoles. Let the reference elements for the two arrays be oriented in the x-direction and z-direction

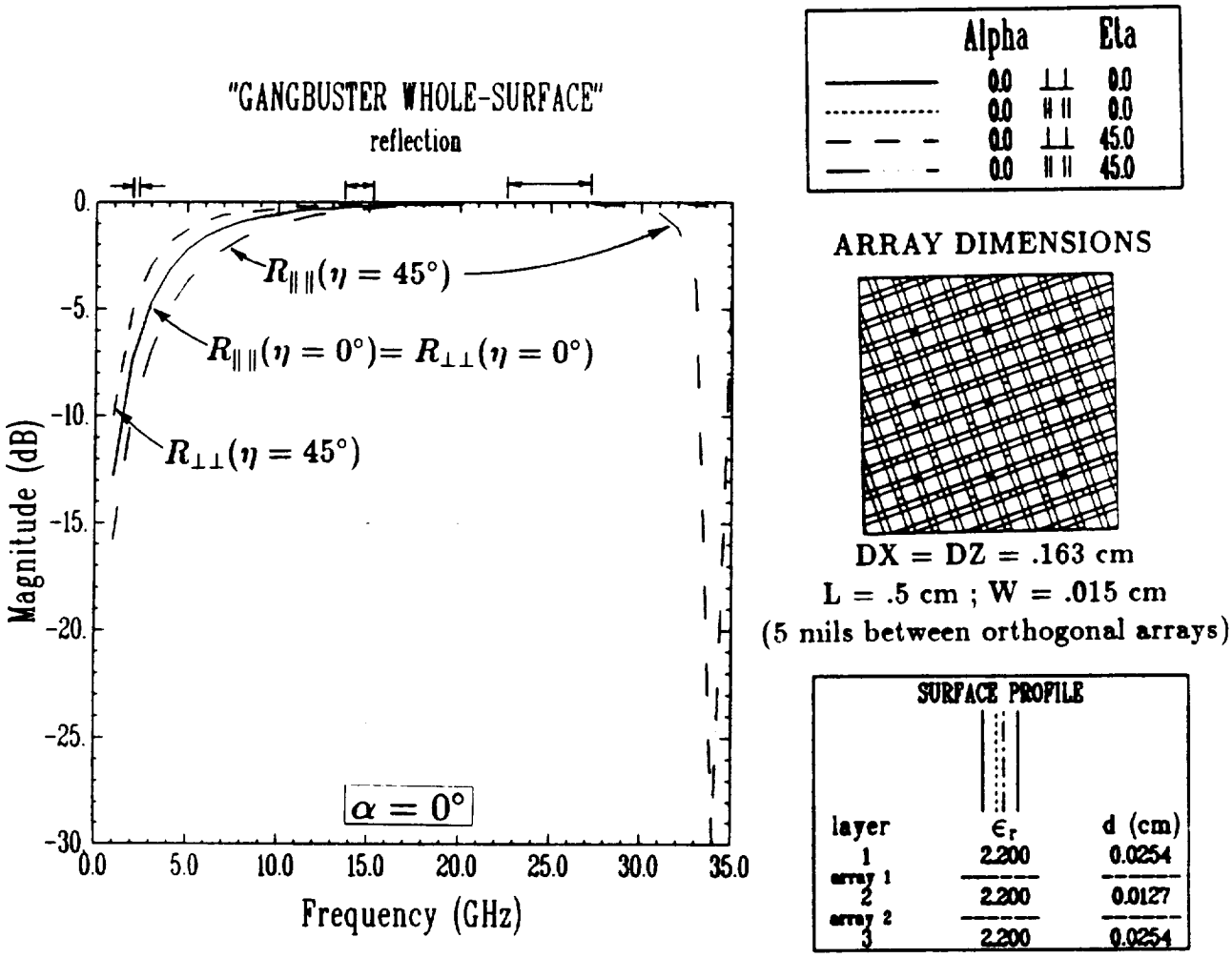

Figure 4.1: The "gangbuster whole-surface" parallel reflection coefficient for the plane of incidence $\alpha = 0°$ (aligned with elements), and angles of incidence $\eta = 0°$ and $\eta = 45°$.

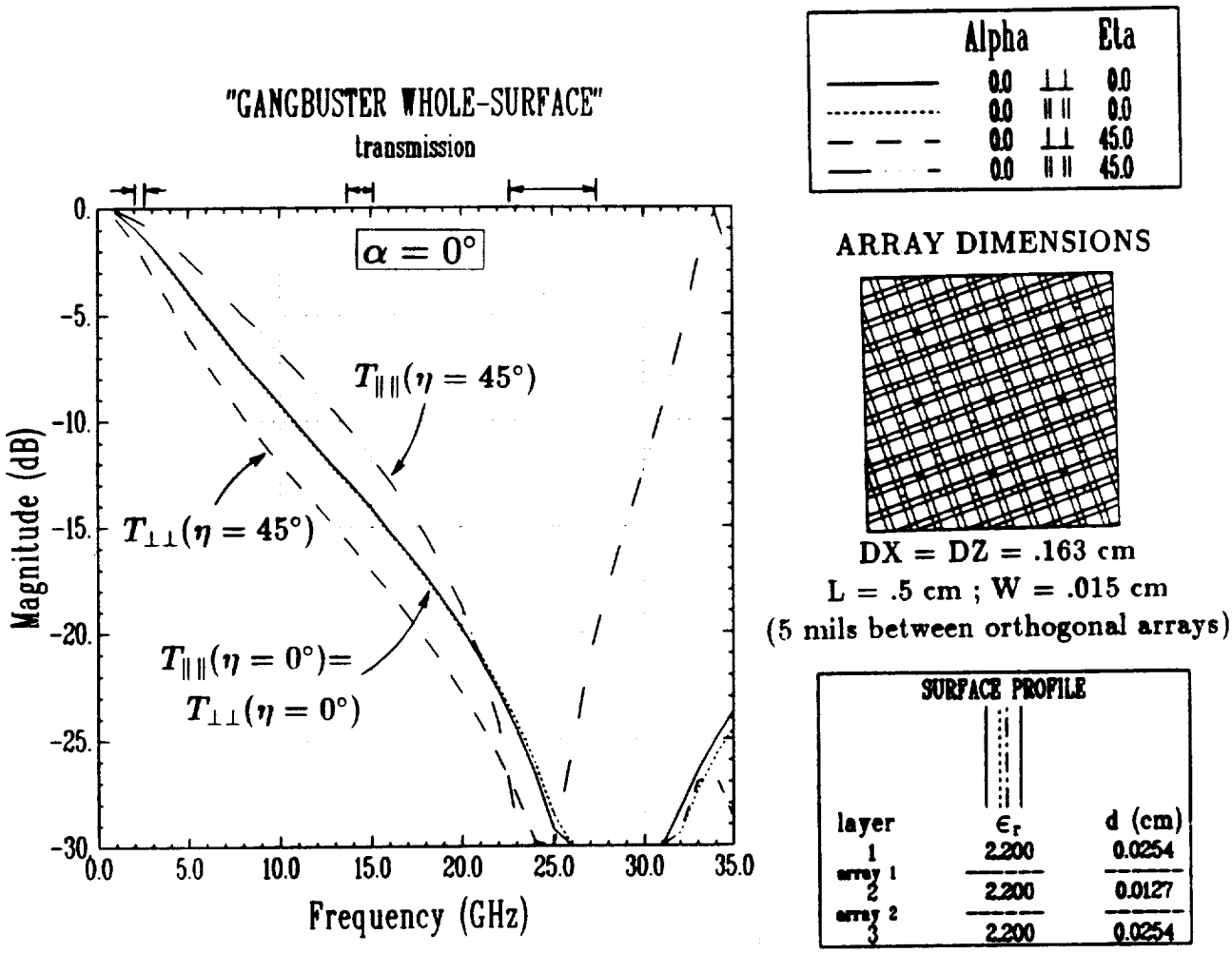

Figure 4.2: The "gangbuster whole-surface" parallel transmission coefficient for the plane of incidence $\alpha = 0°$ (aligned with elements), and angles of incidence $\eta = 0°$ and $\eta = 45°$.

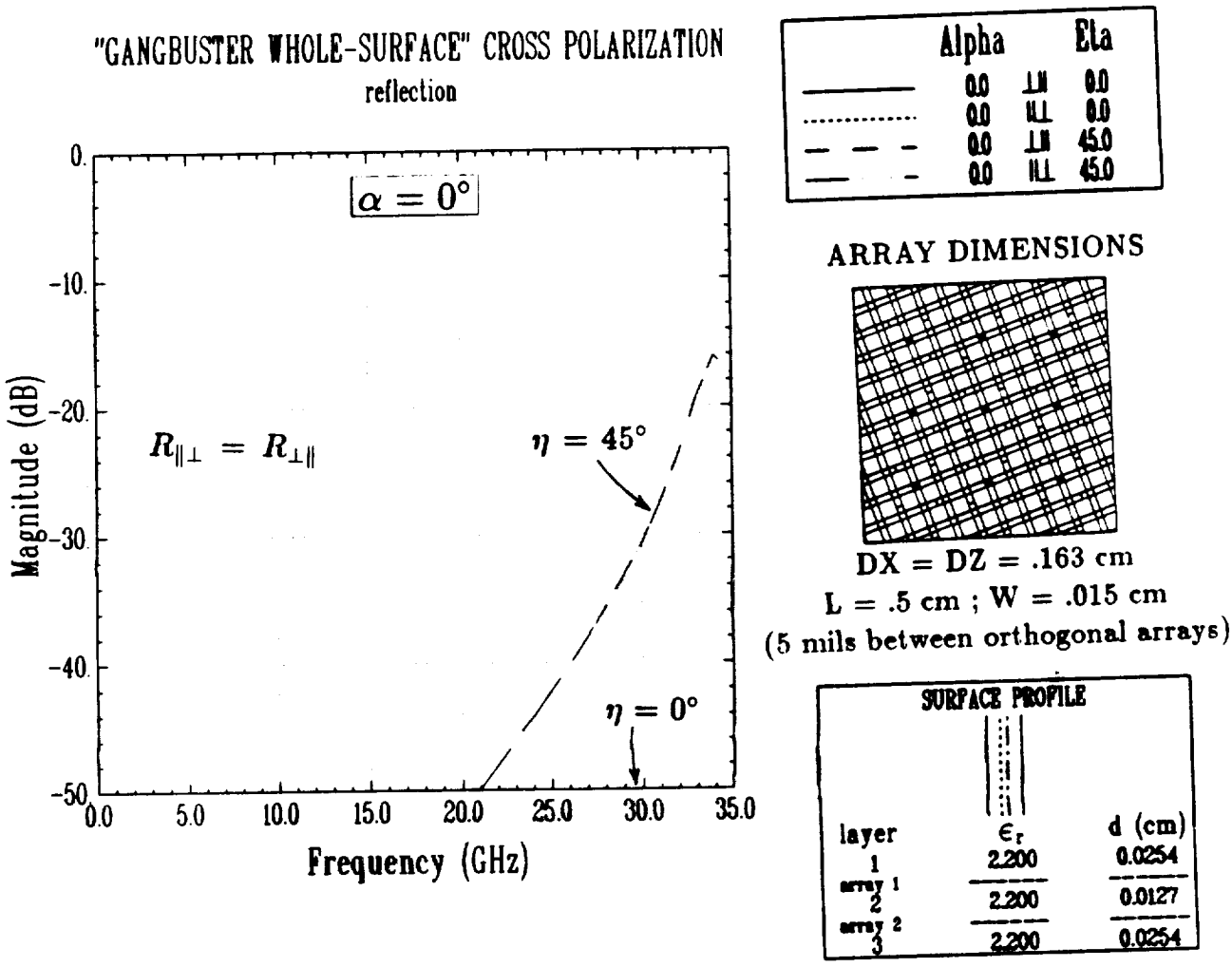

Figure 4.3: The "gangbuster whole-surface" cross polarized reflection coefficient for the plane of incidence $\alpha = 0°$ (aligned with elements), and angles of incidence $\eta = 0°$ and $\eta = 45°$.

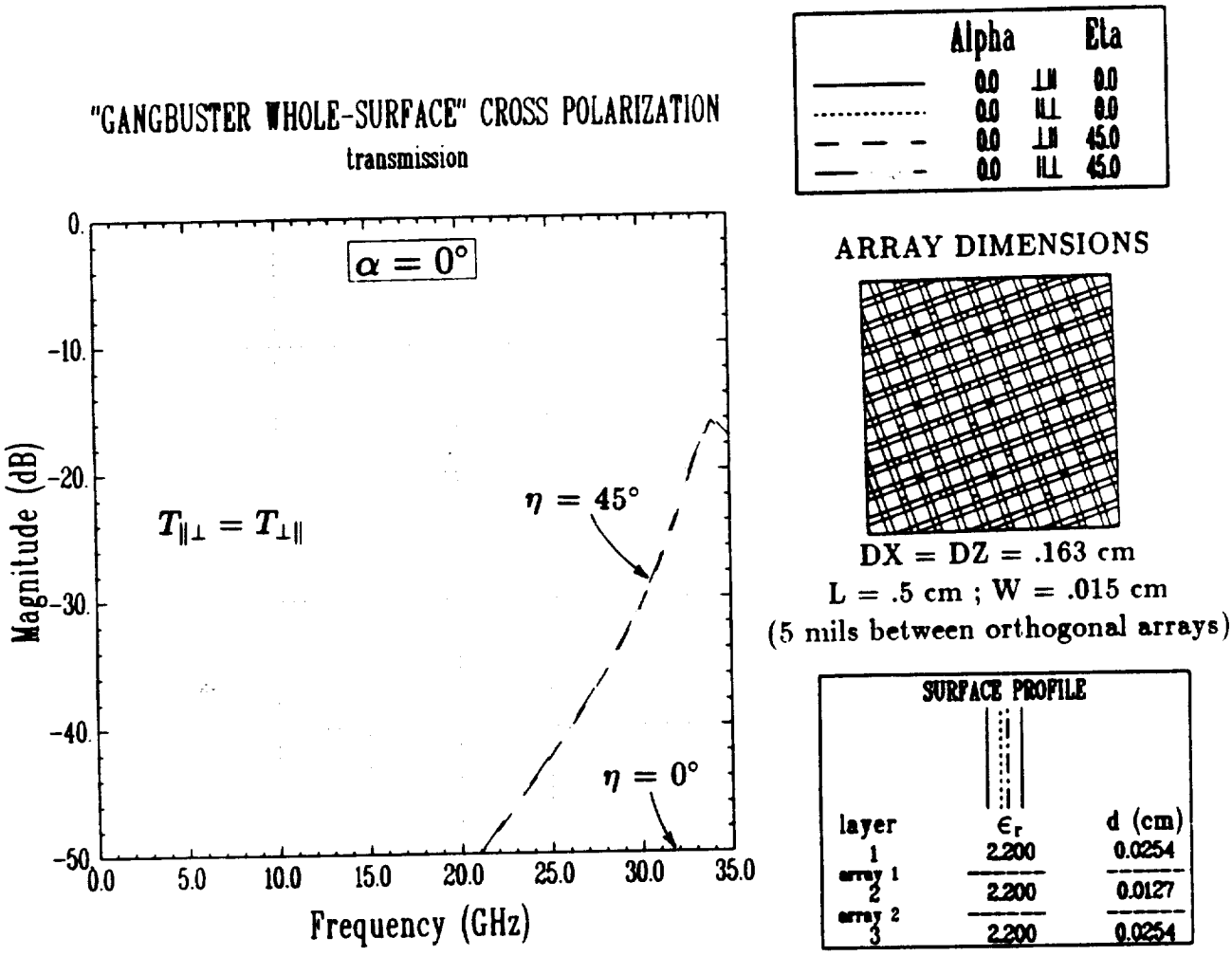

Figure 4.4: The "gangbuster whole-surface" cross polarized transmission coefficient for the plane of incidence $\alpha = 0°$ (aligned with elements), and angles of incidence $\eta = 0°$ and $\eta = 45°$.

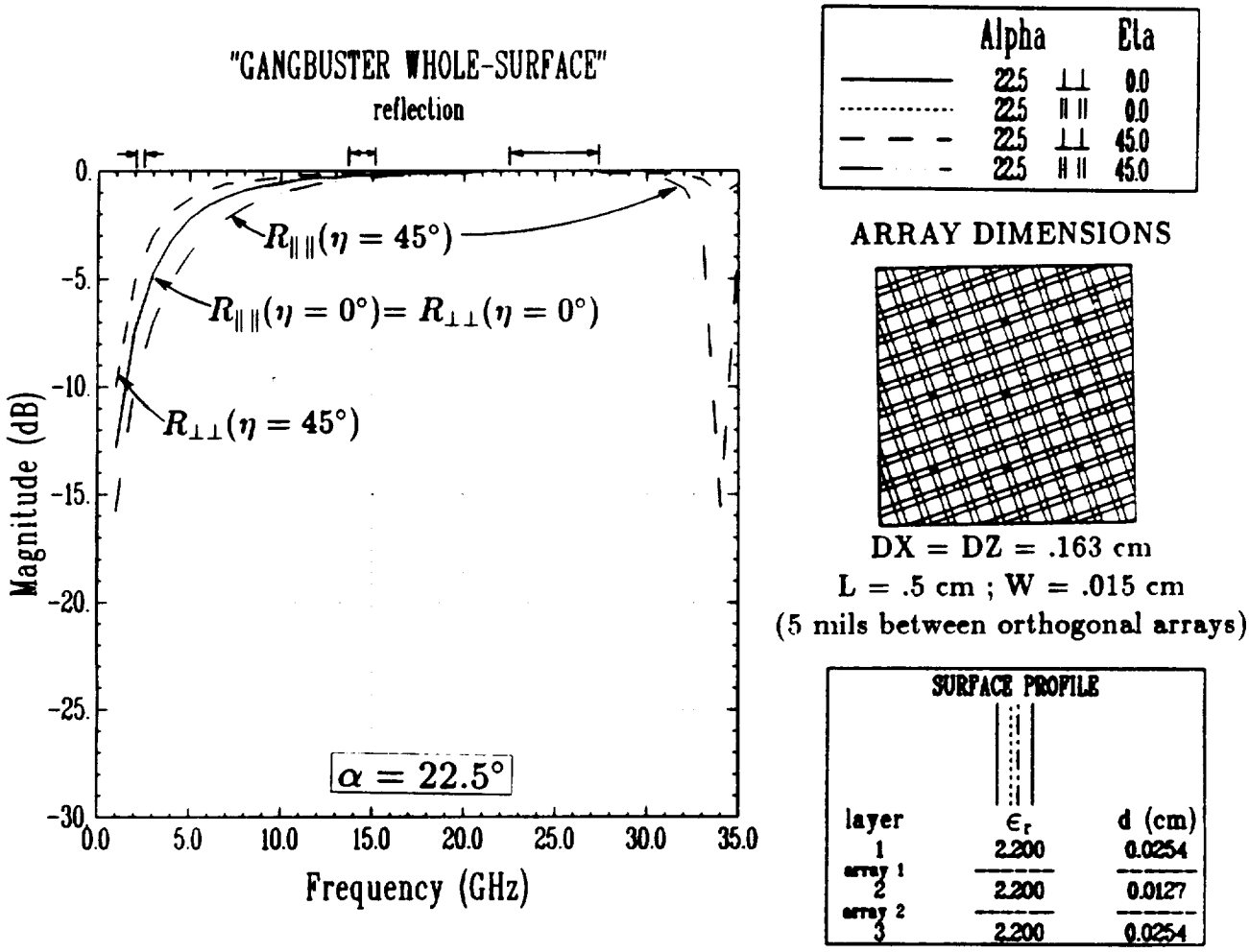

Figure 4.5: The "gangbuster whole-surface" parallel reflection coefficient for the plane of incidence $\alpha = 22.5°$, and angles of incidence $\eta = 0°$ and $\eta = 45°$.

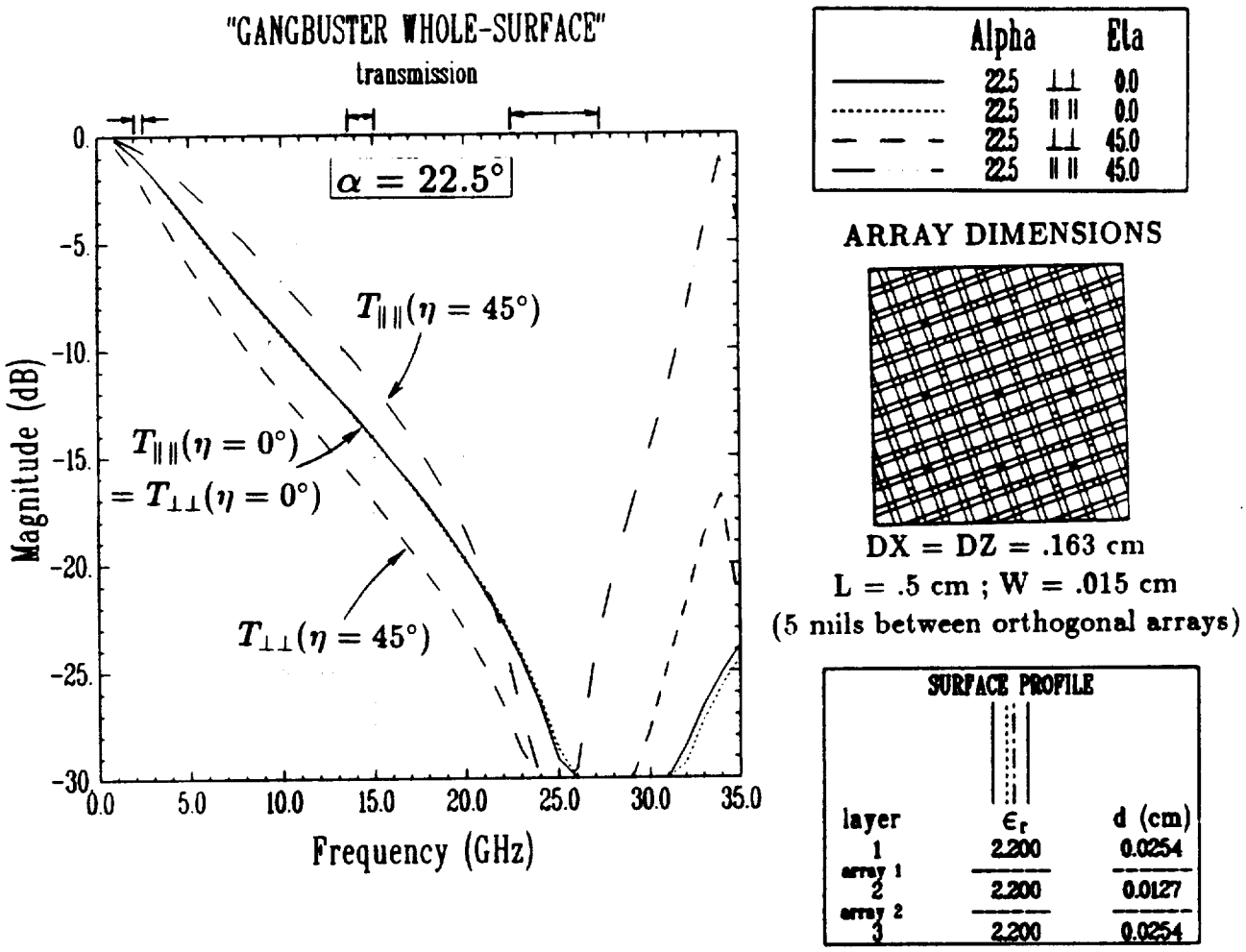

Figure 4.6: The "gangbuster whole-surface" parallel transmission coefficient for the plane of incidence $\alpha = 22.5°$, and angles of incidence $\eta = 0°$ and $\eta = 45°$.

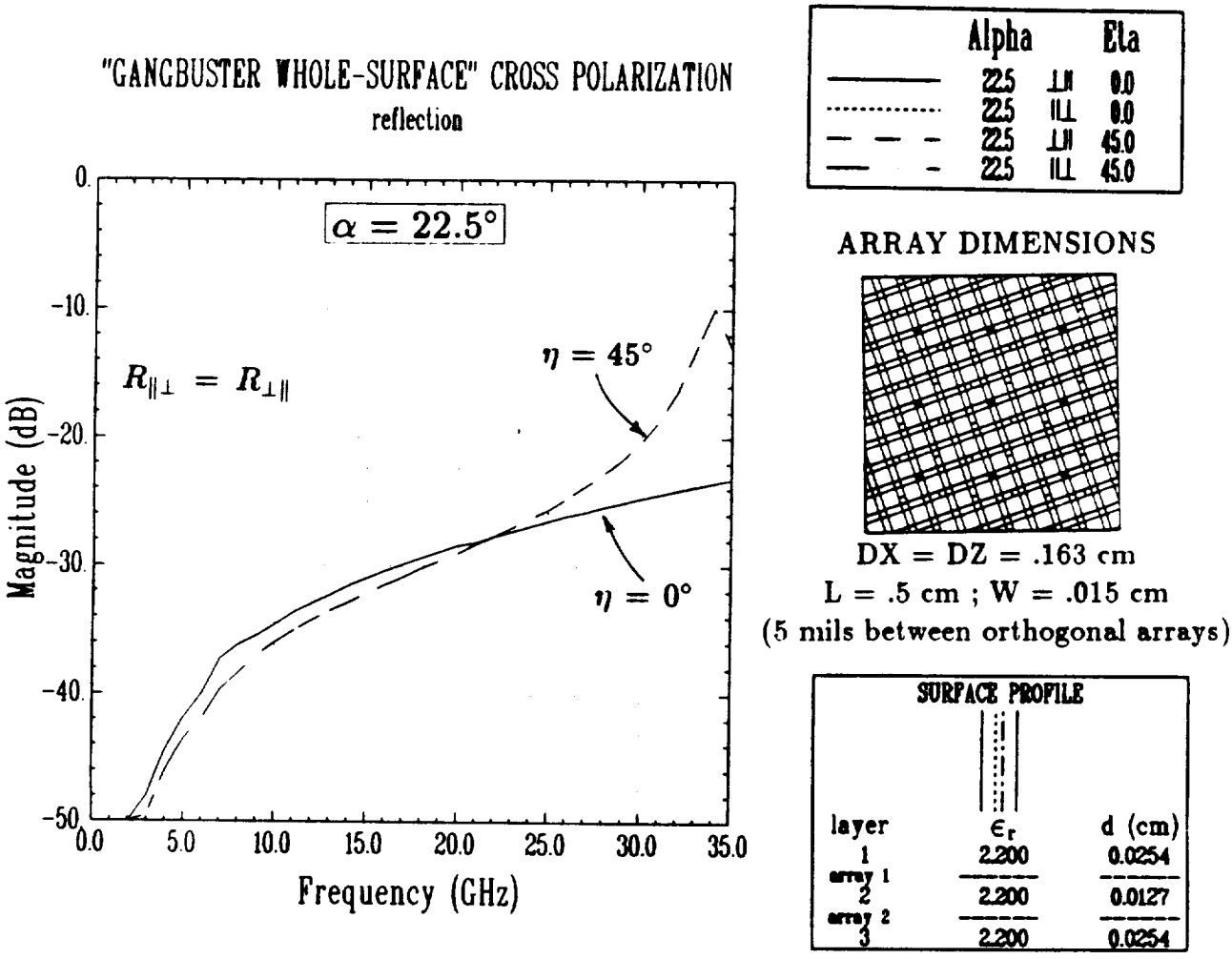

Figure 4.7: The "gangbuster whole-surface" cross polarized reflection coefficient for the plane of incidence $\alpha = 22.5°$, and angles of incidence $\eta = 0°$ and $\eta = 45°$.

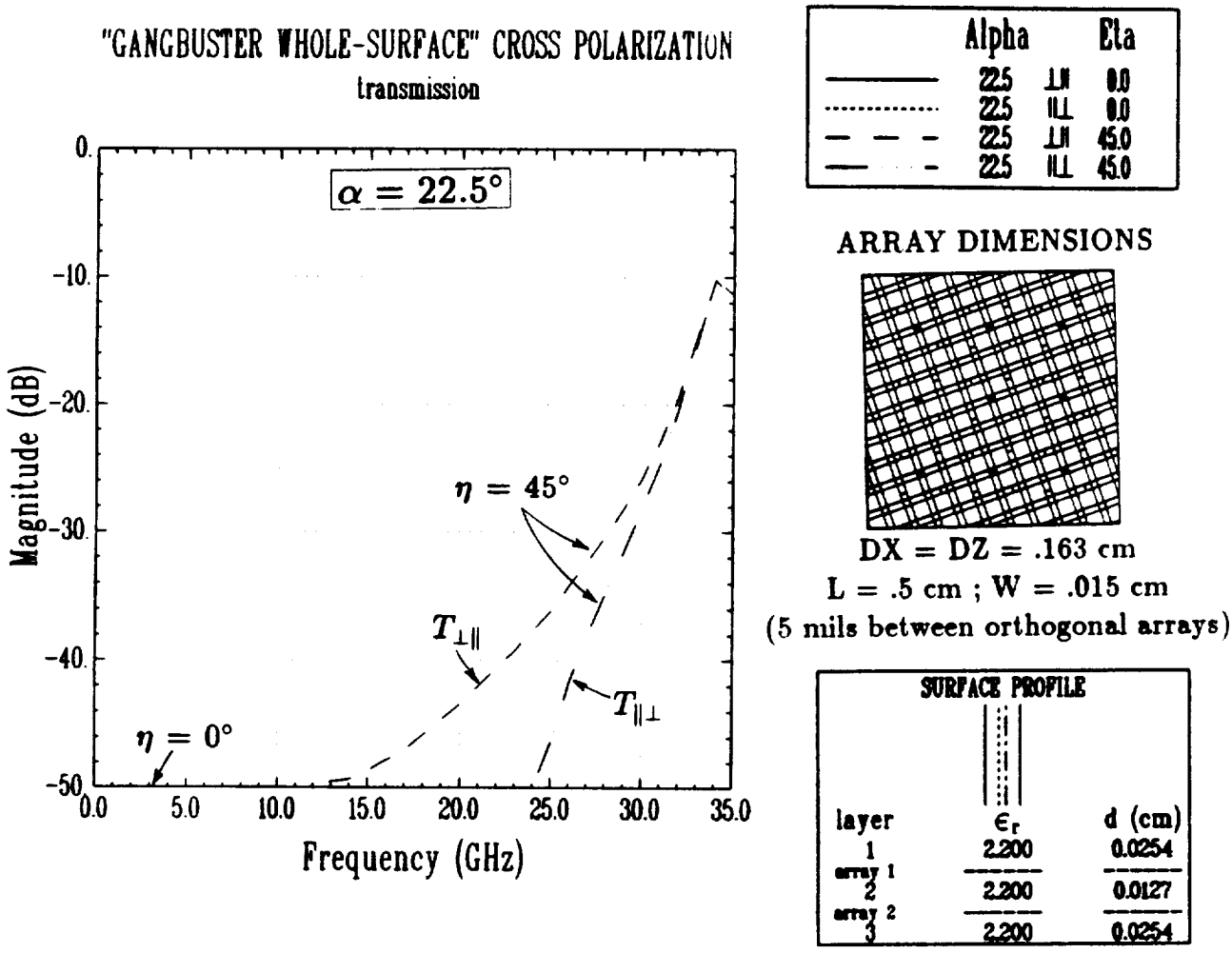

Figure 4.8: The "gangbuster whole-surface" cross polarized transmission coefficient for the plane of incidence $\alpha = 22.5°$, and angles of incidence $\eta = 0°$ and $\eta = 45°$.

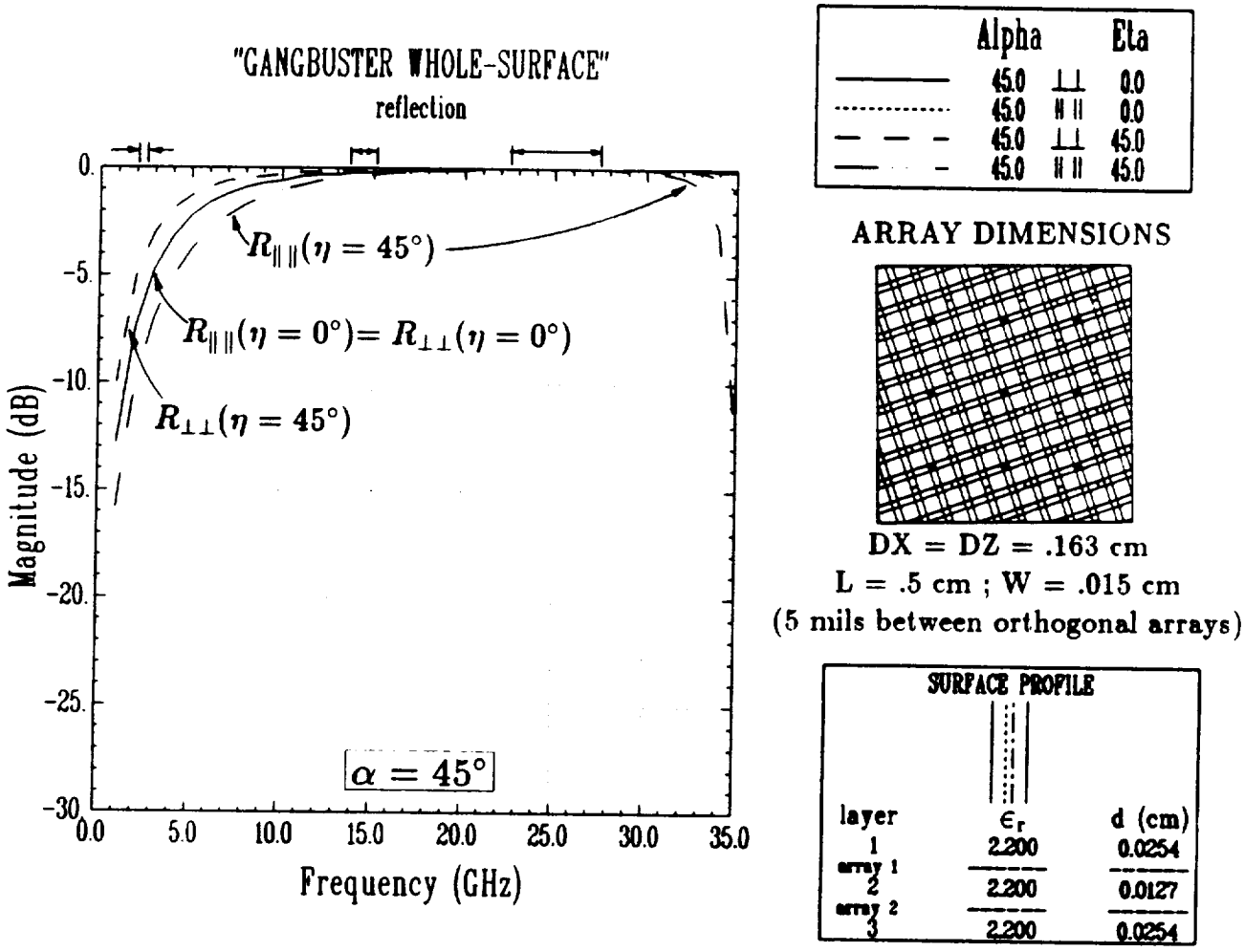

Figure 4.9: The "gangbuster whole-surface" parallel reflection coefficient for the plane of incidence $\alpha = 45°$ (bisecting elements), and angles of incidence $\eta = 0°$ and $\eta = 45°$.

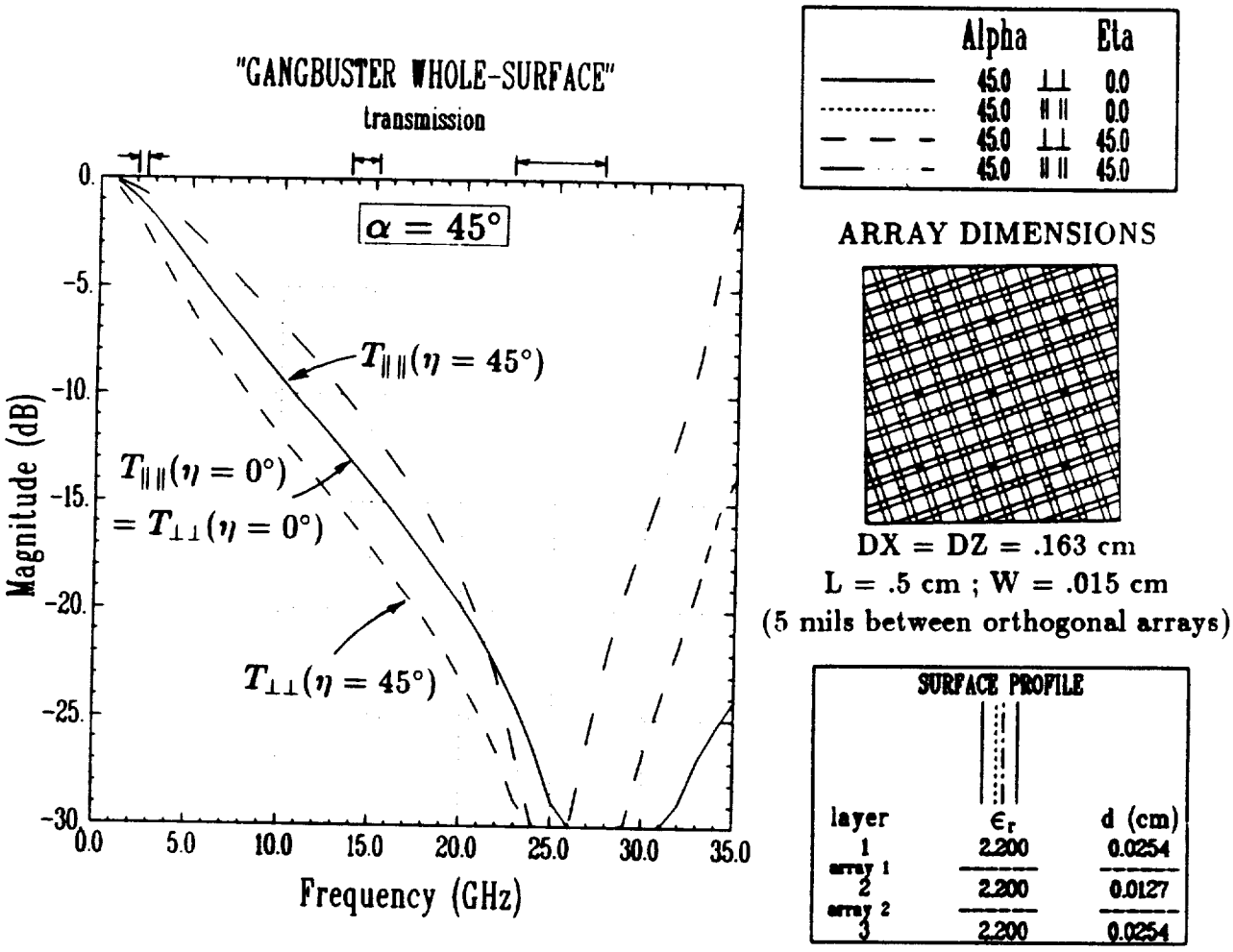

Figure 4.10: The "gangbuster whole-surface" parallel transmission coefficient for the plane of incidence $\alpha = 45°$ (bisecting the elements), and angles of incidence $\eta = 0°$ and $\eta = 45°$.

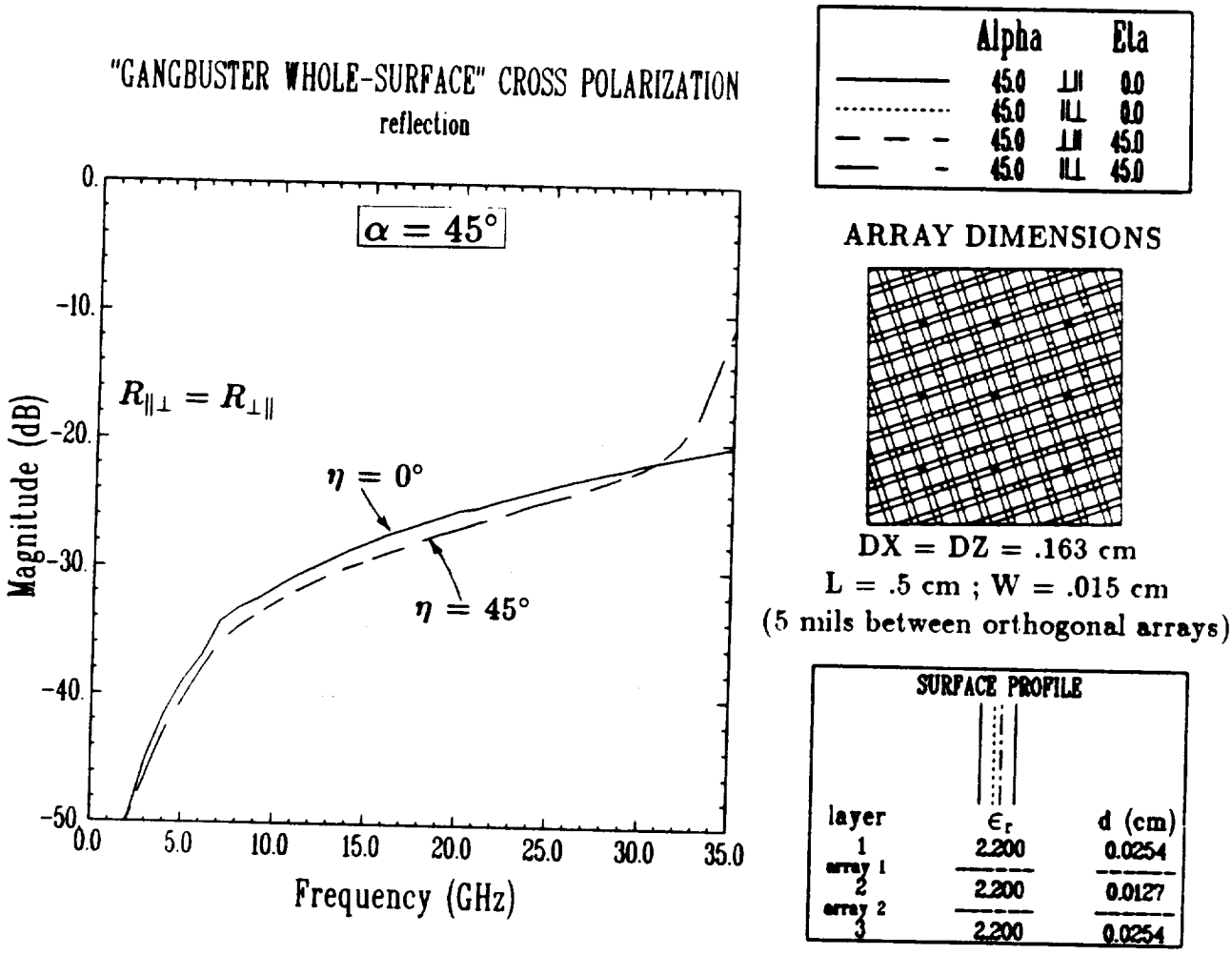

Figure 4.11: The "gangbuster whole-surface" cross polarized reflection coefficient for the plane of incidence $\alpha = 45°$ (bisecting the elements), and angles of incidence $\eta = 0°$ and $\eta = 45°$.

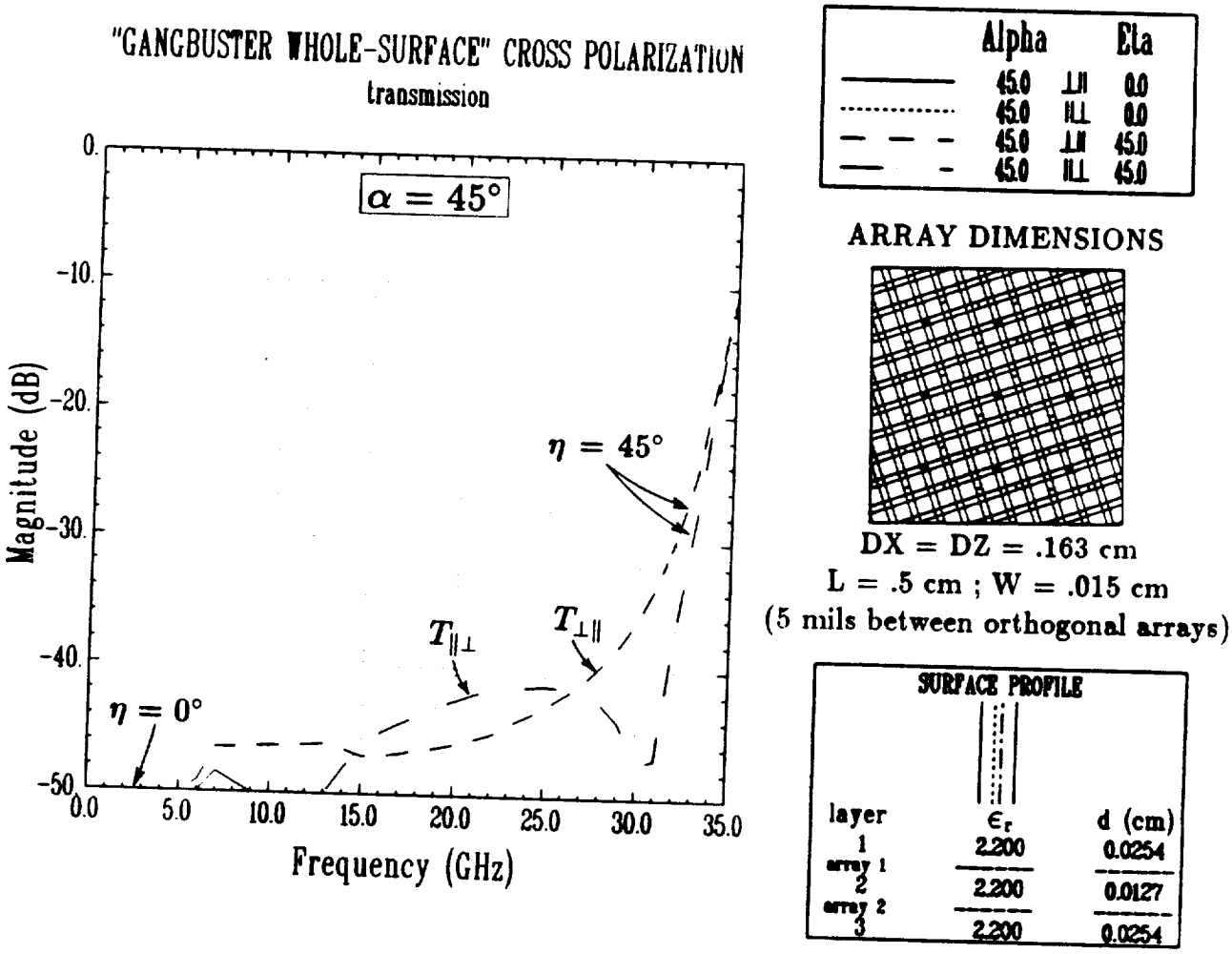

Figure 4.12: The "gangbuster whole-surface" cross polarized transmission coefficient for the plane of incidence $\alpha = 45°$ (bisecting the elements), and angles of incidence $\eta = 0°$ and $\eta = 45°$.

and their separation be denoted by "s" along the y-axis as shown. We now examine the two extreme cases, namely when a: the incident field $E^i_{||}$ is oriented along the z-axis (the aligned case) and b: the incident E-field is oriented along the diagonal between the x- and z-axis (the bisecting case).

In the aligned case shown in Figure 4.13a there will be no voltage induced in the x-oriented element by the incident field $\bar{E}^i$. Thus, any current on the x-oriented element will be entirely caused by only the array mutual coupling $Z^{z,x}$. This means both the reflected $R_{||\perp}$ and transmitted $T_{||\perp}$ signals come from the x-oriented element only, and their magnitudes must therefore be equal. Now consider the case where the incident E-field is bisecting x and z-axis as shown in Figure 4.13b. This field can be decomposed into the components E^i_x and E^i_z. Let us choose the point P on the y-axis midway between the two arrays as phase reference. In that event, the field reradiated from the x-oriented element traveling in the negative y-direction (reflected) will be $\hat{x}E^r_x e^{-j\beta s r_y}$. Similarly the signal from the z-oriented element is $\hat{z}E^r_z e^{+j\beta s r_y}$ where for all practical purposes $E^r_x \sim E^r_z \sim E^r$. Thus, the total reflected field is:

$$\begin{aligned}
\bar{E}^r &= E^r \left[\hat{x}e^{-j\beta s r_y} + \hat{z}e^{+j\beta s r_y}\right] \\
&= E^r \left[(\hat{x}+\hat{z})\cos\beta s r_y + j(-\hat{x}+\hat{z})\sin\beta s r_y\right] \\
\bar{E}^r &= \bar{E}^r_{|||}\cos\beta s r_y + j\bar{E}^r_{||\perp}\sin\beta s r_y \qquad (4.1)
\end{aligned}$$

where $\bar{E}^r_{|||}$ is the field reflected parallel and $\bar{E}^r_{||\perp}$ is reflected orthogonal to the incident field $\bar{E}^i_{||}$. Similarly the field transmitted in the positive y-direction will be given by:

$$\bar{E}^t = \hat{x}E^t_x(e^{+j\beta\frac{s}{2}r_y}\cdot e^{-j\beta\frac{s}{2}r_y}) + \hat{z}E^t_z(e^{-j\beta\frac{s}{2}r_y}\cdot e^{+j\beta\frac{s}{2}r_y})$$

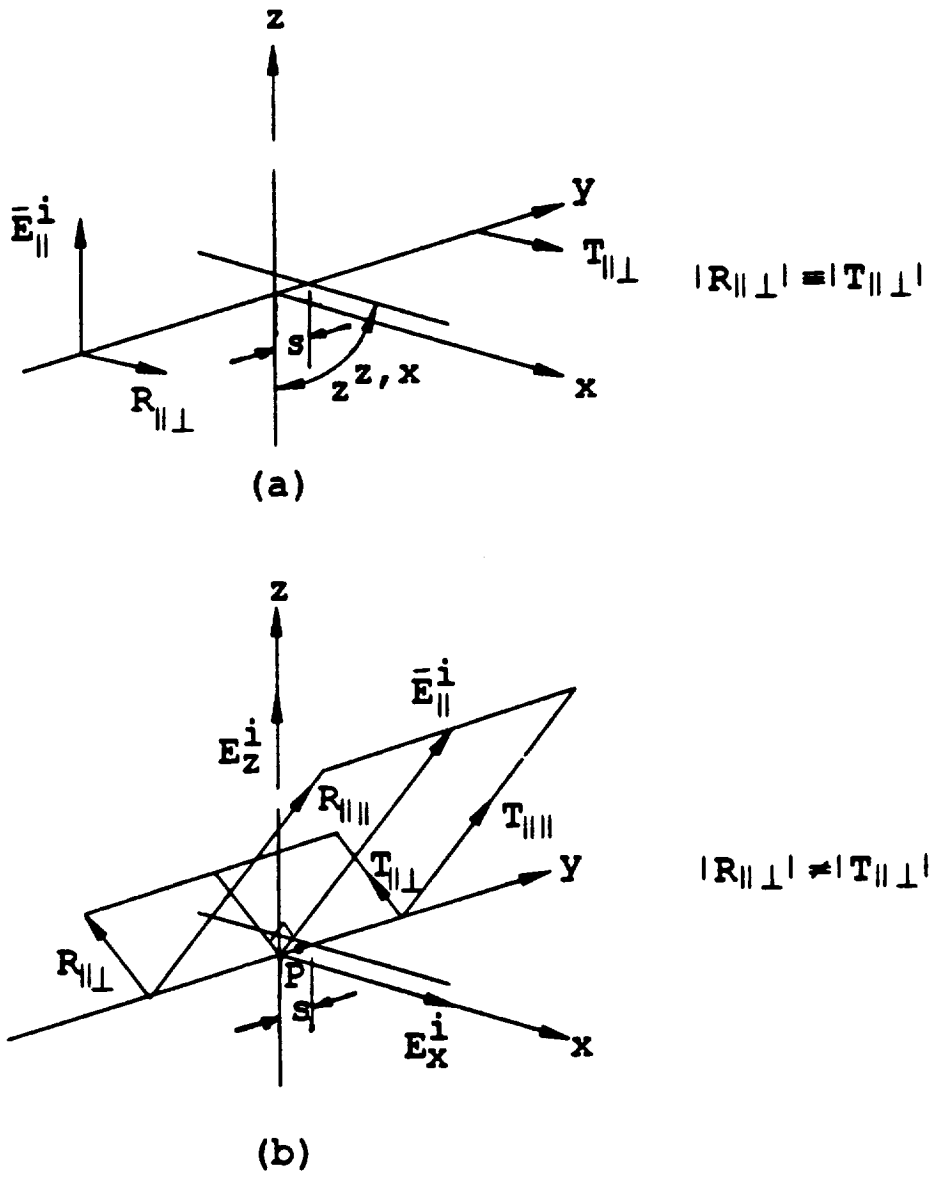

Figure 4.13: Two orthogonal arrays with the reference element for the front array oriented along the z-axis and the rear reference element oriented in the x-direction. The array separation is denoted by "s" along the y-axis.

a: The incident E-field is oriented in the z-direction (aligned case).
b: The incident E-field is oriented at 45° with respect to the z-axis (bisecting case).

$$= \hat{x}E_x^t + \hat{z}E_z^t = \bar{E}_{\|\|}^t + 0 \cdot \bar{E}_{\|\perp}^t. \tag{4.2}$$

Comparison between Equations (4.1) and (4.2) show that while a sizeable cross polarization is present in the reflected signal, it is "phased out" in the transmitted signal. The low level cross polarization that is observed at higher angles of incidence and frequencies in the calculated transmission curves is simply due to some mutual coupling between the orthogonal arrays not accounted for in case "b". Inspection of Equation (4.1) clearly shows the cross polarized reflection coefficient $R_{\|\perp}$ to be basically proportional to the array separation "s" as long as $\beta s r_y \ll 1$. This parameter "s" will therefore be explored in more detail in the next section.

4.1.2 Cross Polarization in "Whole-Surfaces" as a Function of Array Separation "s"

All of the results shown to this point have been for type-3 "gangbuster whole-surfaces" with an array separation distance "s"= 5 mils. In this section we show the effect that this separation"s" has on the cross polarization. Figure 4.14 and 4.15 show the cross polarized reflection and transmission coefficient curves for the $\eta = 45°$ angle of incidence (worst case), and for array separations "s" = 2.5, 5.0, 10.0, and 20.0 mils. The plane of incidence is $\alpha = 45°$ (again the worst case). The parallel reflection and transmission coefficient curves for this case are shown in Figures 4.9 and 4.10 for "s" = 5.0 mils (these curves represent the other spacings quite well also).

We note from Figure 4.14 that the reflection cross polarization, $R_{\|\perp}$, increases with the array separation as indicated in Equation (4.1). We note further from Figure 4.15 that while the transmission cross polarization is

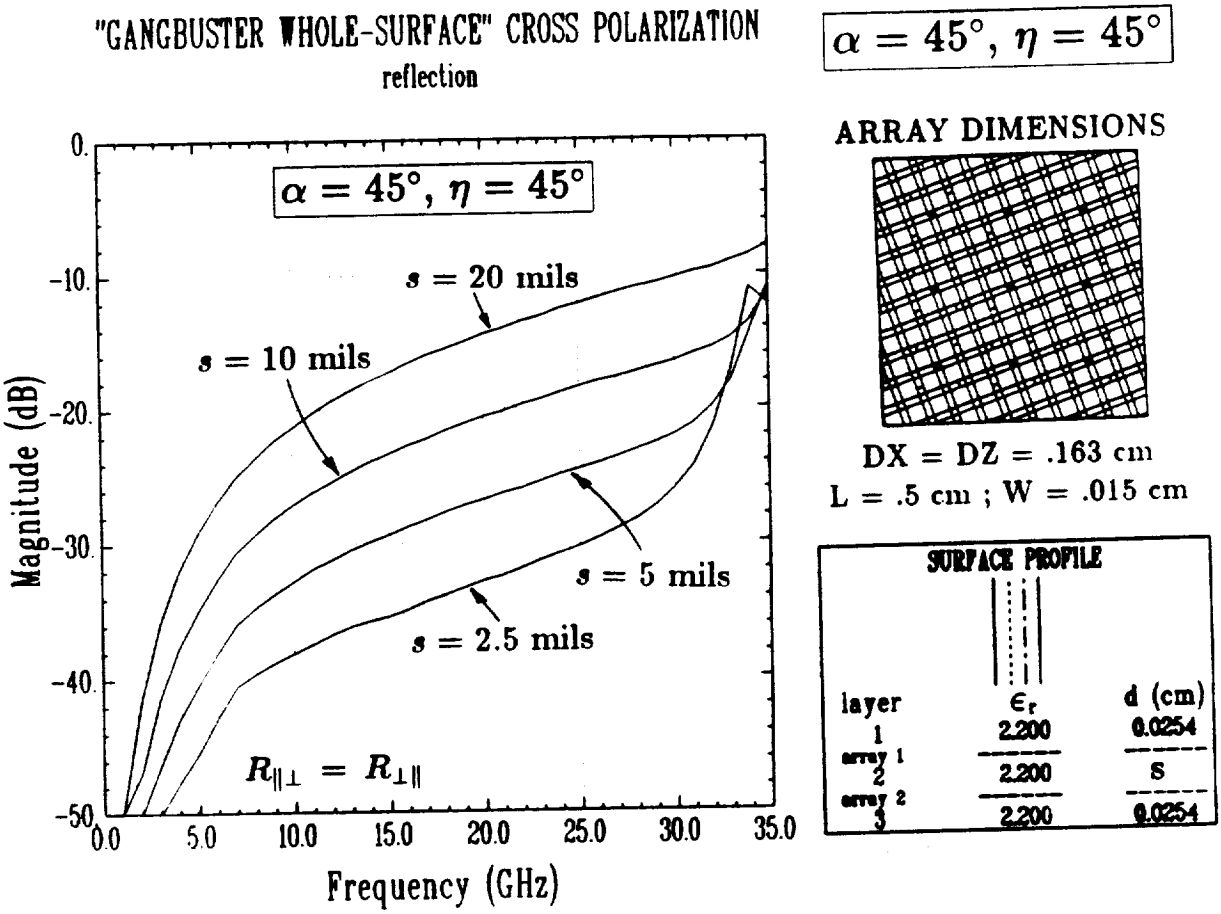

Figure 4.14: The cross polarized reflection coefficient as a function of frequency for angle of incidence $\eta = 45°$ and the plane of incidence $\alpha = 45°$. Parameter is the array separation "s".

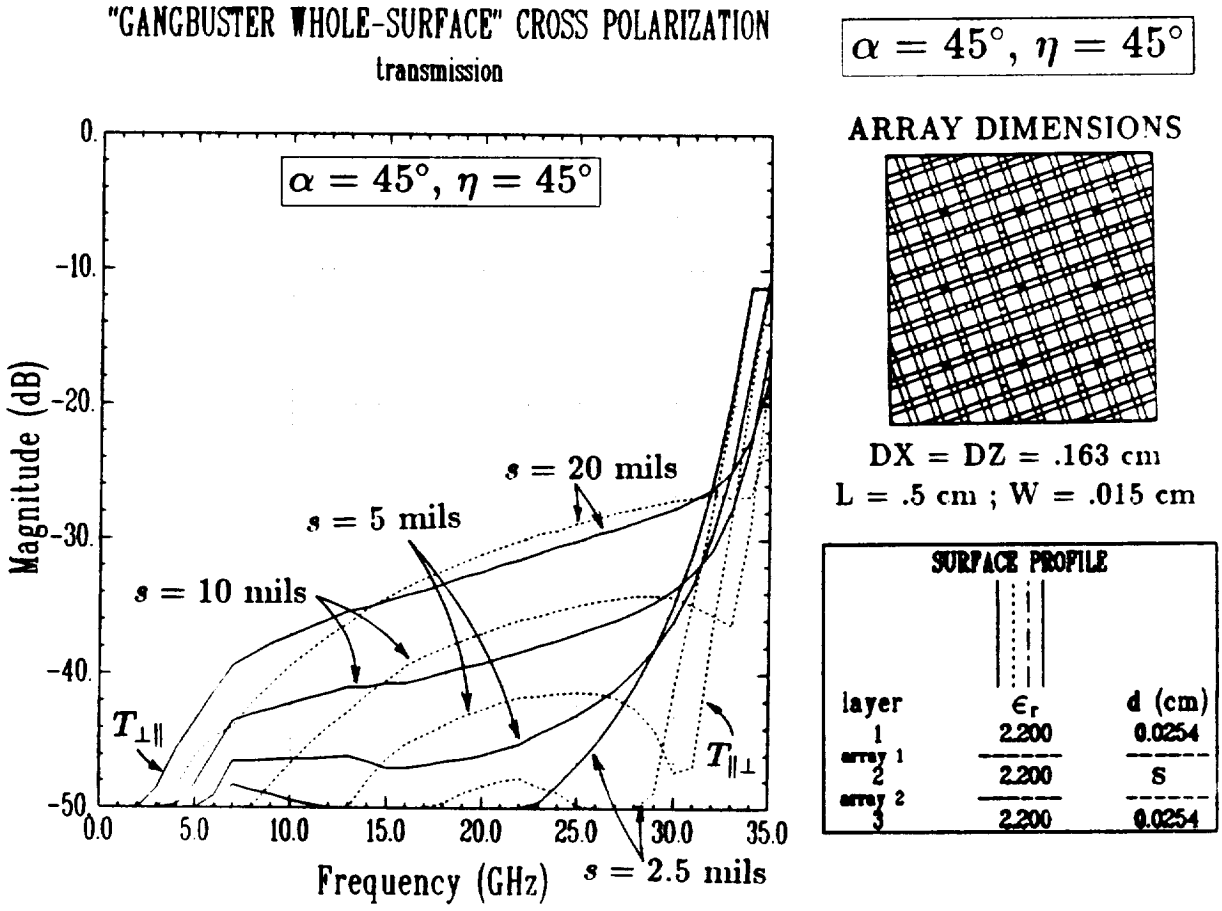

Figure 4.15: The cross polarized transmission coefficient as a function of frequency for angle of incidence $\eta = 45°$ and the plane of incidence $\alpha = 45°$. Parameter is the array separation "s".

substantually smaller than the reflection cross polarization, it is not zero as Equation (4.2) predicts. This discrepency is due to mutual coupling between the two arrays which was not incorporated into our simple derivation. Finally we note that as the frequency increases $R_{\|\perp} \sim T_{\|\perp}$ for all spacings shown here. This is because the cross polarization above resonance ($\sim$ 26 GHz) is dominated by array mutual coupling.

4.1.3 Effect of Registration of the Two Orthogonal "Half-Surfaces" on the Cross Polarization

In all of cases treated so far, the two orthogonal "half-surfaces" of our "whole-surface" were positioned with respect to each other as shown in Figure 4.16 (top). This particular registration is referred to as the "no offset" case since the dipole centers of the orthogonal "half-surfaces" differ only in the $\hat{y}$-direction. In this section we will consider the effect of changing the relative position of the two arrays in their own planes. The array separation "s" = 5 mils is used for all cases.

We consider three different registrations. The first is the no offset case as described above. The second is obtained by moving the top array $.15L$ (where L is the total length of the element) as shown in Figure 4.16 (middle). This orientation is called offset1. The final case is obtained by moving both arrays $.15L$ as shown in Figure 4.16 (bottom) and is called offset1=offset2. Figure 4.17 and 4.18 show the cross polarized reflection and transmission coefficients for all three cases in the $\alpha = 45°$ plane of incidence, and at $\eta = 45°$ angle of incidence. From these figures we note that cross polarization is relatively independent of the registration of the two orthogonal "half-

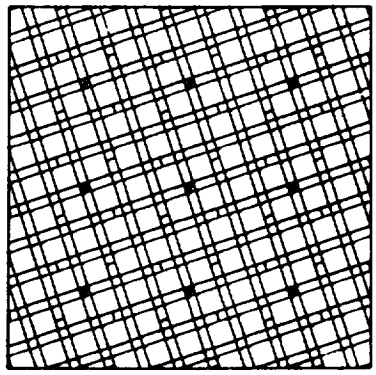

NO OFFSET

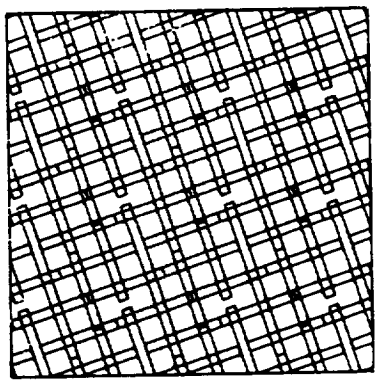

OFFSET1=.15L

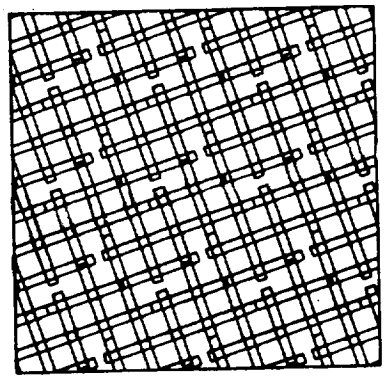

OFFSET1=OFFSET2=.15L

Figure 4.16: Various Registrations of the two orthogonal "half surfaces".

top: No Offset (reference)
middle: Offset1=.15L
bottom: Offset1=Offset2=.15L

surfaces".

4.2 Cross Polarization of the "Gangbuster" Dichroic Surface Design both with and without a Matching Plate

We now present the results for the double array dichroic surface design of Chapter 2 with the "gangbuster half-surfaces" replaced by "gangbuster whole-surfaces". The "whole-surface" used in this design is the same surface discussed thoroughly earlier in this chapter. Recall that Figures 4.9 and 4.10 show the parallel reflection and transmission coefficient for this "whole-surface" in the $\alpha = 45°$ (i.e. the worst cross polarization case). When two of these surfaces are separated a distance $d = 1.95$ cm apart to form the double array surface we have the parallel reflection and transmission coefficient curves shown in Figures 4.19 and 4.20 ($\alpha = 45°$, $\eta = 0°$ and $\eta = 45°$). Finally, the addition of the dielectric matching plate produces the parallel reflection and transmission coefficient curves shown in Figures 4.21 and 4.22. (again for $\alpha = 45°$, $\eta = 0°$ and $\eta = 45°$). The pertinent dimensions of the various surfaces are given in the figure inserts.

Having seen the parallel reflection and transmission coefficients of this design, we focus on its cross polarization properties. Recall that the cross polarized reflection and transmission curve for this single "gangbuster whole-surface" are shown in Figures 4.11 and 4.12 for the $\alpha = 45°$ case. We now show in Figures 4.23 and 4.24 the reflection and transmission cross polarization coefficients for the double array design without the dielectric matching

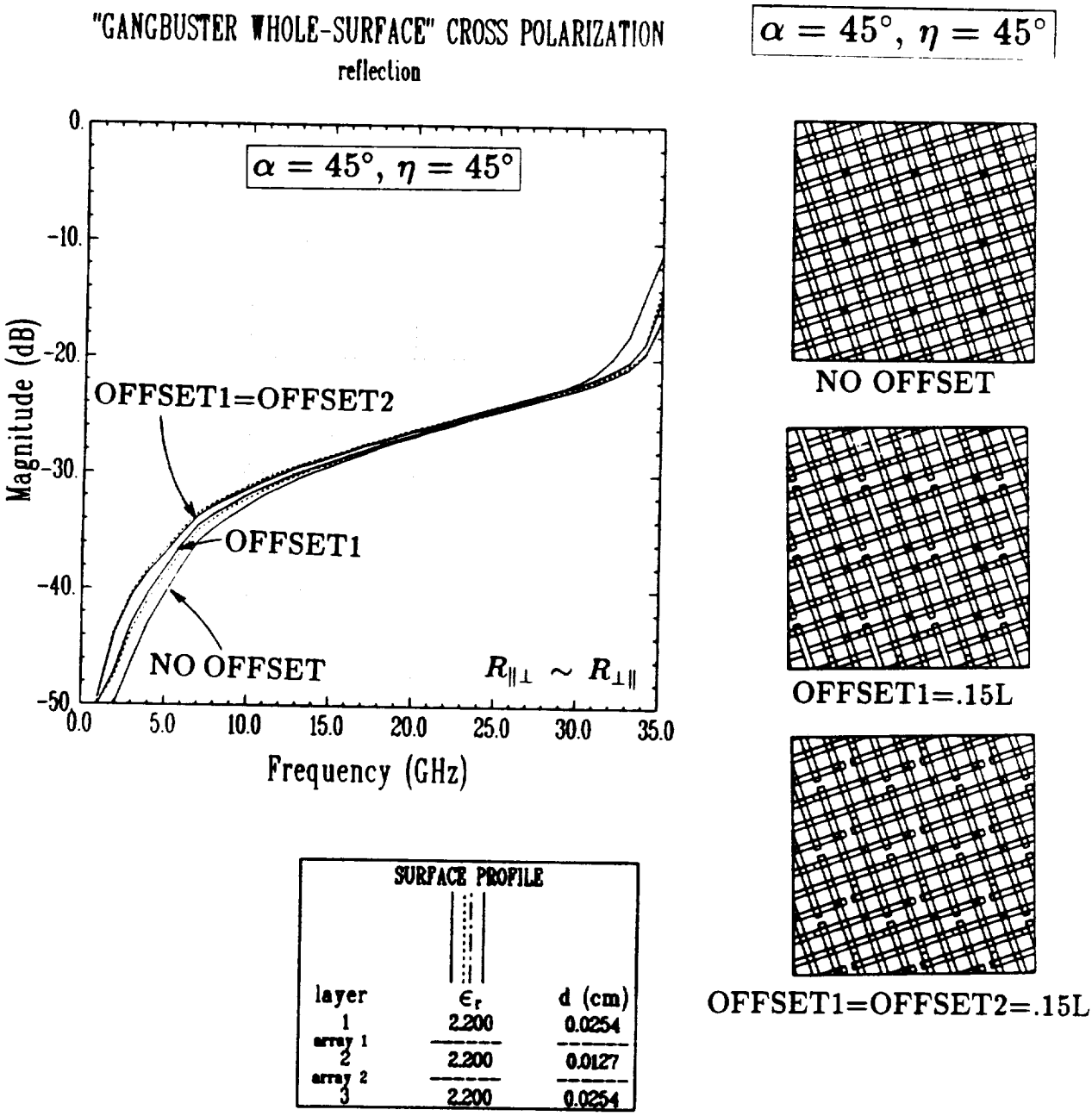

Figure 4.17: The cross polarized reflection coefficient as a function of frequency for angle of incidence $\eta = 45°$ and the plane of incidence $\alpha = 45°$. Parameter is the two "half-surface" positions with respect to each other as shown in Figure 4.16.

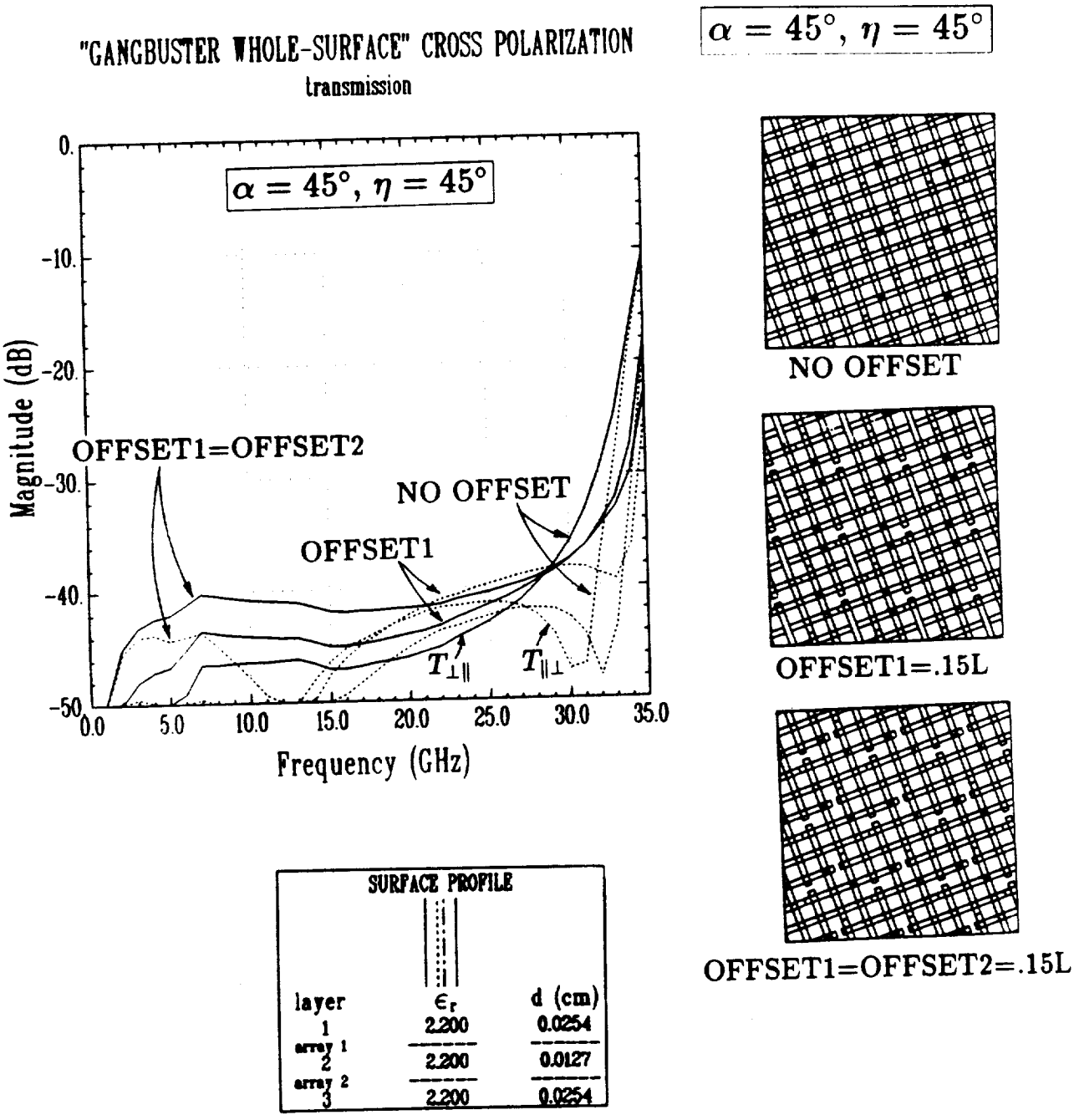

Figure 4.18: The cross polarized transmission coefficient as a function of frequency for angle of incidence $\eta = 45°$ and the plane of incidence $\alpha = 45°$. Parameter is the two "half-surface" positions with respect to each other as shown in Figure 4.16.

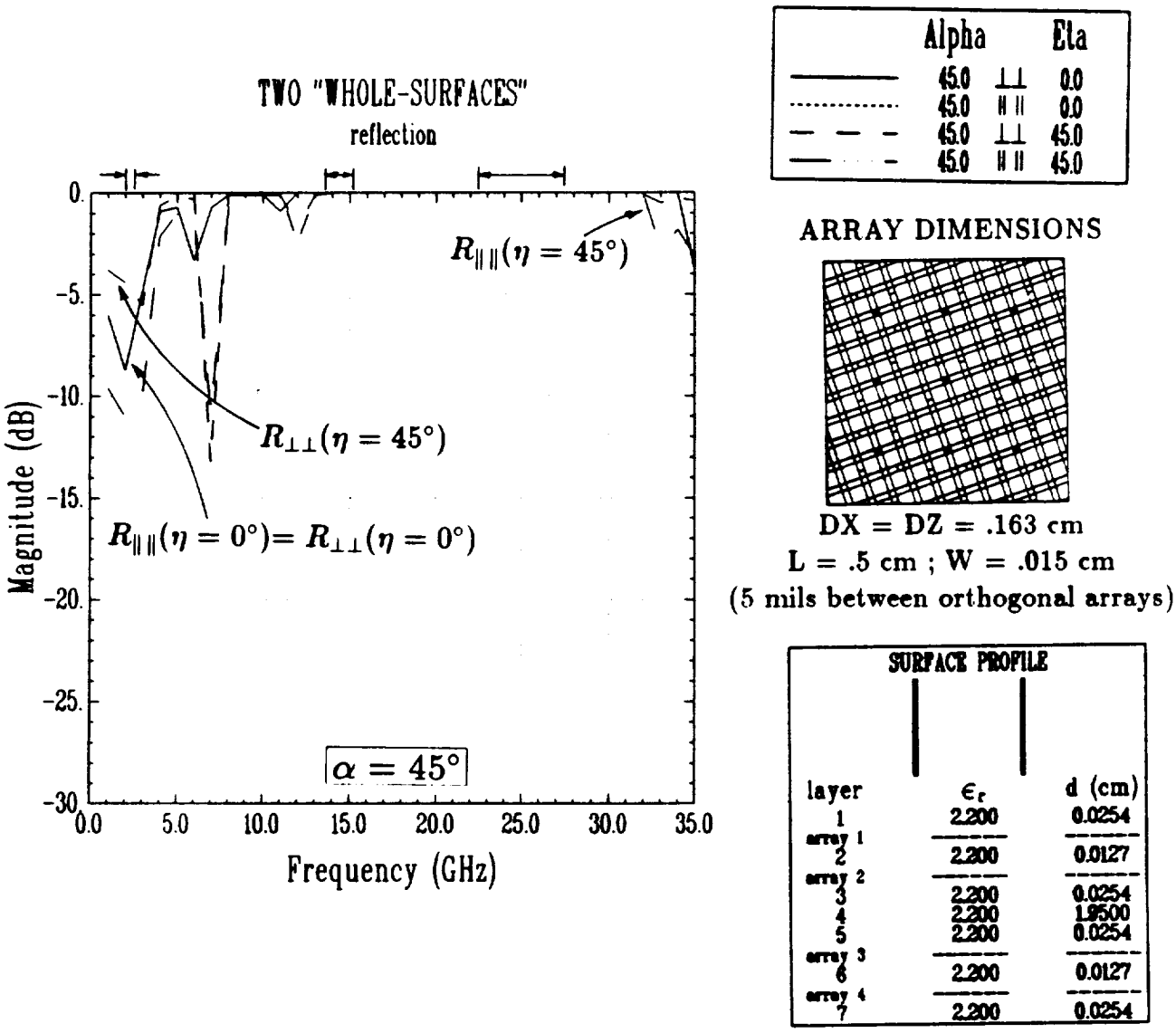

Figure 4.19: The reflection coefficient curves for the double array surface in the plane of incidence $\alpha = 45°$ at angles of incidence $\eta = 0°$ and $\eta = 45°$

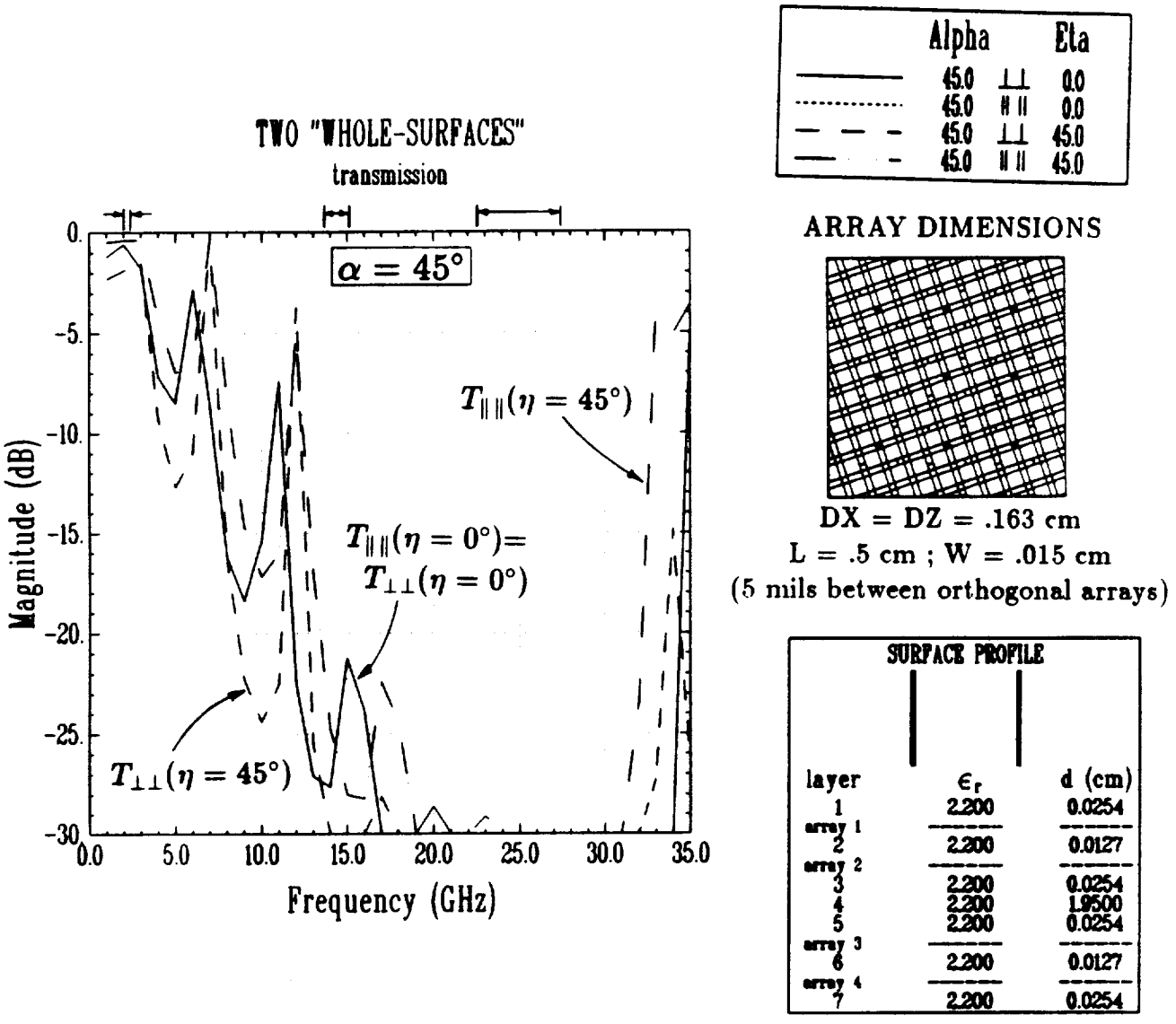

Figure 4.20: The transmission coefficient curves for the double array surface in the plane of incidence $\alpha = 45°$ at angles of incidence $\eta = 0°$ and $\eta = 45°$

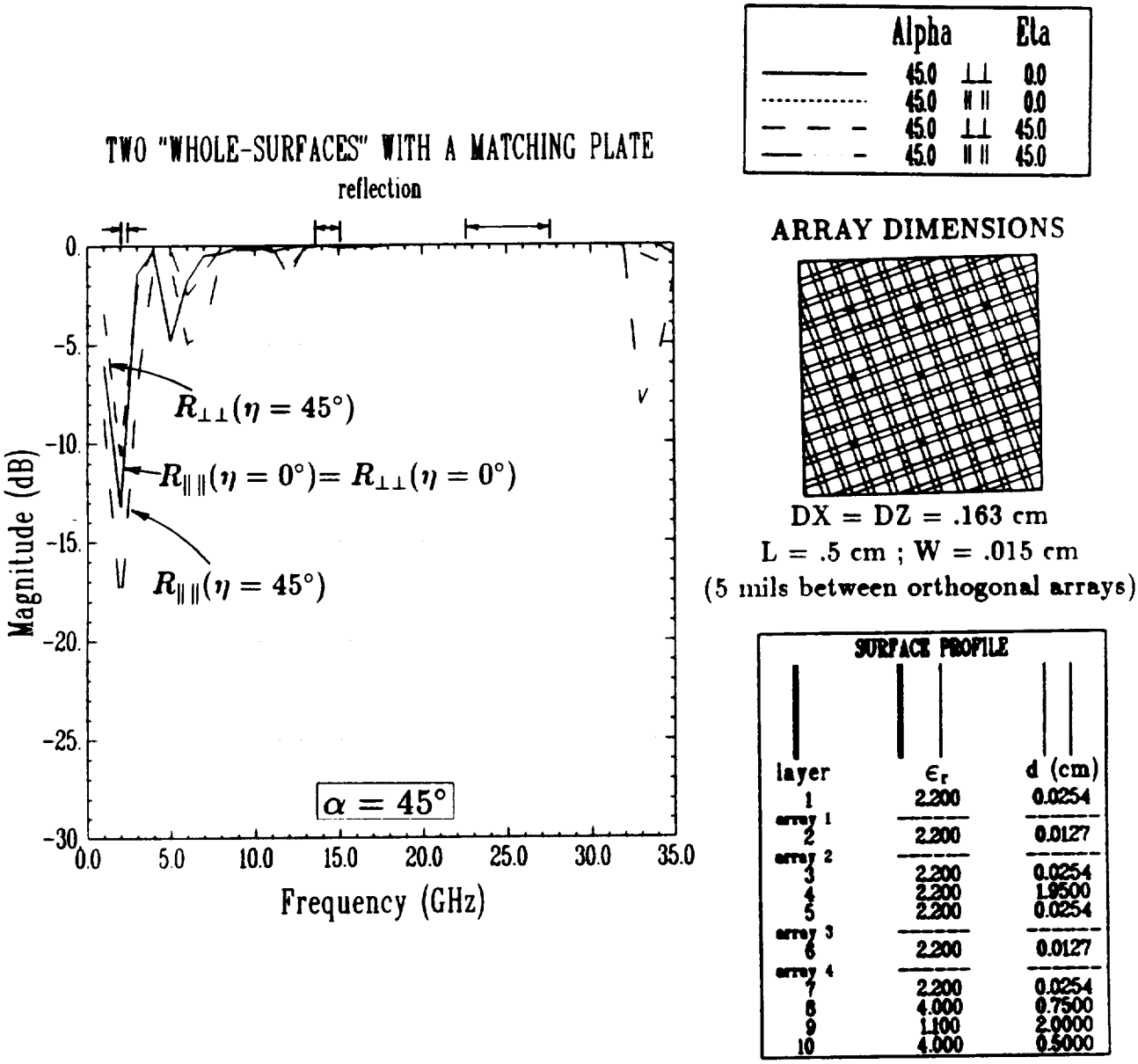

Figure 4.21: The reflection coefficient curves for the double array surface with a matching plate in the plane of incidence $\alpha = 45°$ at angles of incidence $\eta = 0°$ and $\eta = 45°$

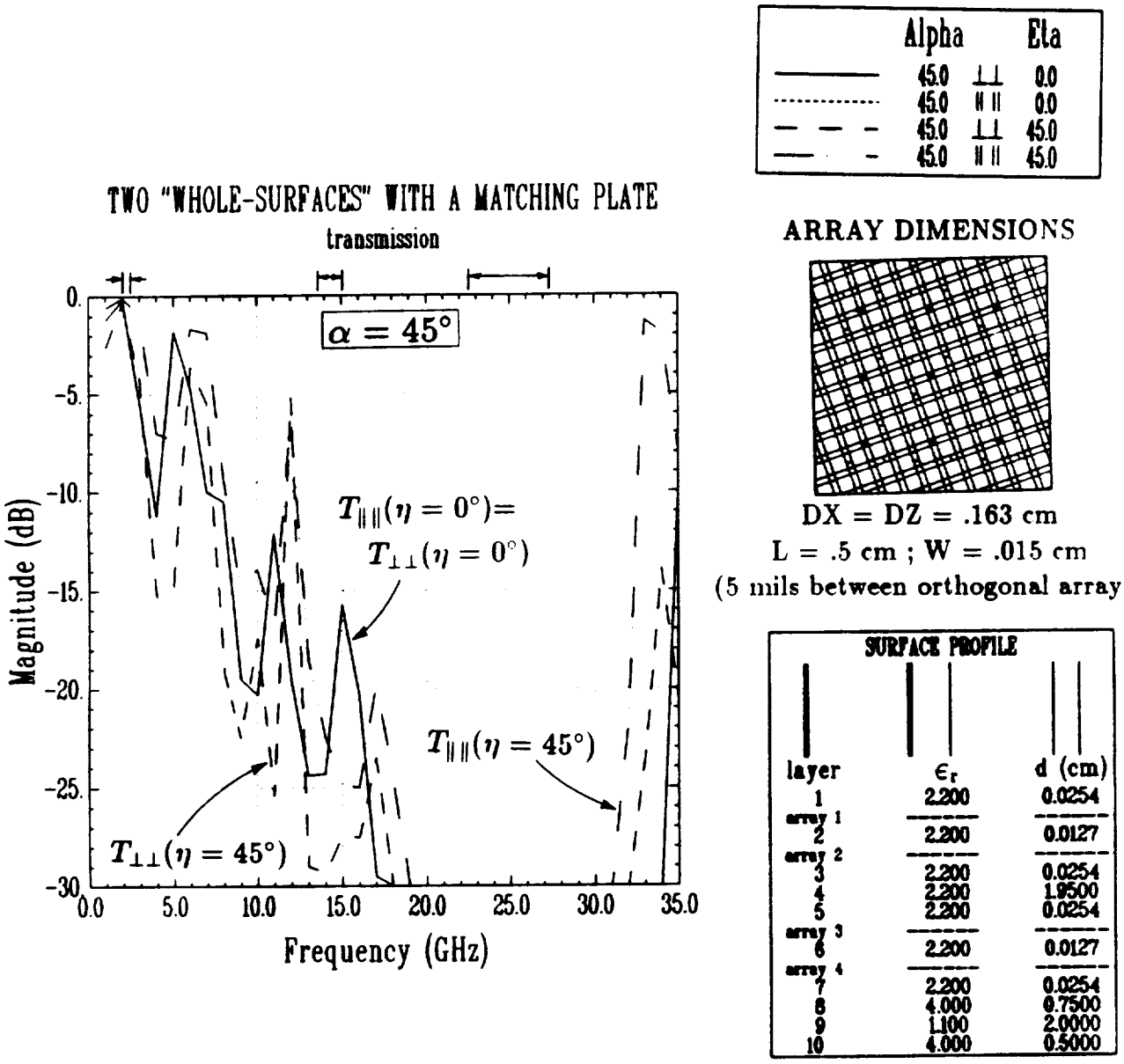

Figure 4.22: The transmission coefficient curves for the double array surface with a matching plate in the plane of incidence $\alpha = 45°$ at angles of incidence $\eta = 0°$ and $\eta = 45°$

plate. Finally we show in Figures 4.25 and 4.26 the reflection and transmission cross polarization coefficients for the double array design with the dielectric matching plate.

Comparing the reflection cross polarization curves of Figure 4.11, Figure 4.23 and Figure 4.25 we notice only minor differences in the curves in the highly reflective regions ($\sim$ 12.5 to $\sim$ 35.0). This is because the cross polarization characteristics of front "whole-surface", which reflects most of the incident energy, are dominant here. Below this reflective region (0.1 to $\sim$ 12.0). a sufficient amount of energy is transmitted through the front surface thus allowing the rear surface and the matching plate to contribute a reflection cross polarization component. The transmission cross polarization curves of Figure 4.12, Figure 4.24 and Figure 4.26 vary due to the different surface profiles, however, the level of this cross polarized component remains quite low in all our regions of interest (below $\sim$ 30 GHz).

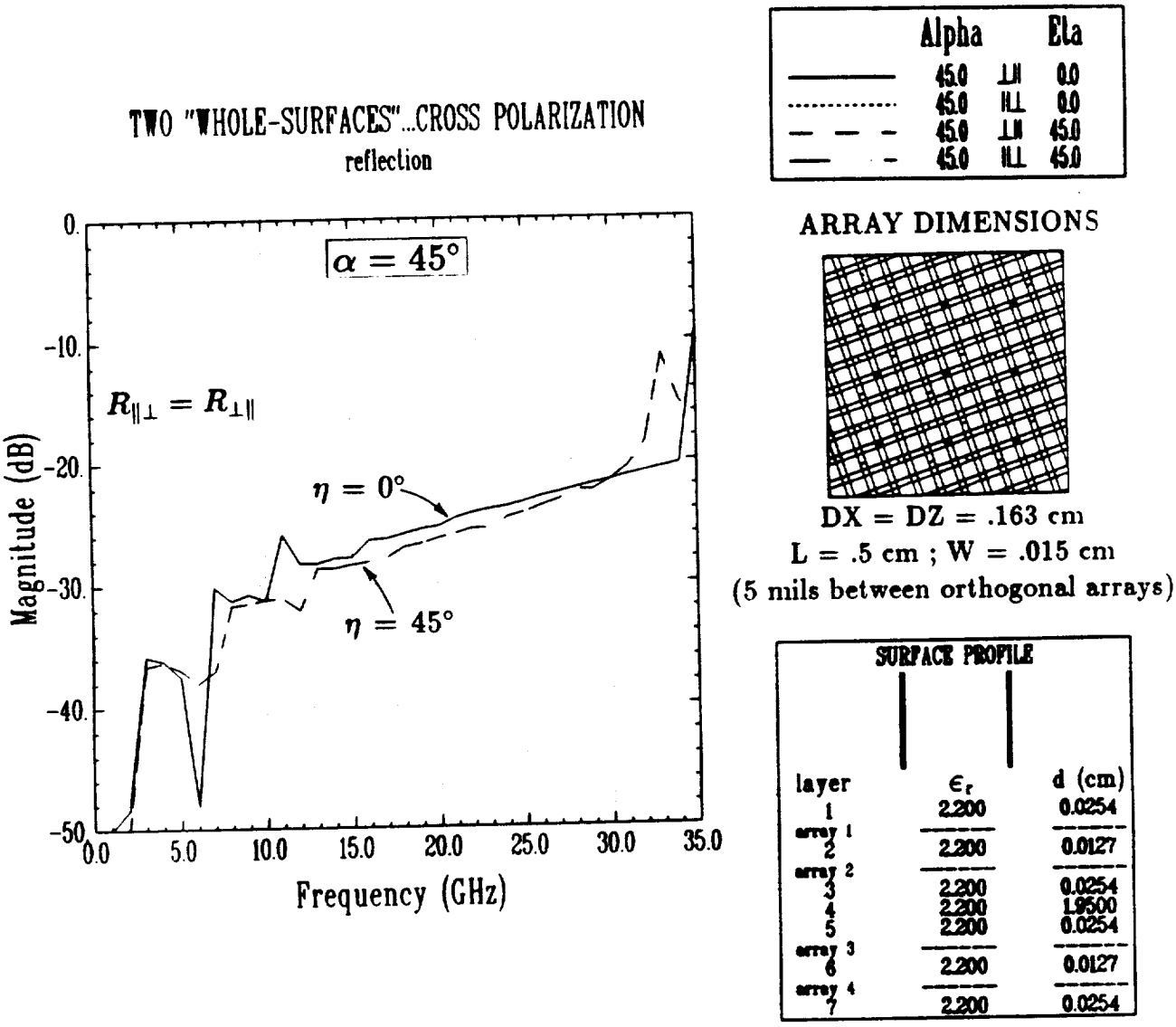

Figure 4.23: The cross polarized reflection coefficient curves for the double array surface in the plane of incidence $\alpha = 45°$ at angles of incidence $\eta = 0°$ and $\eta = 45°$

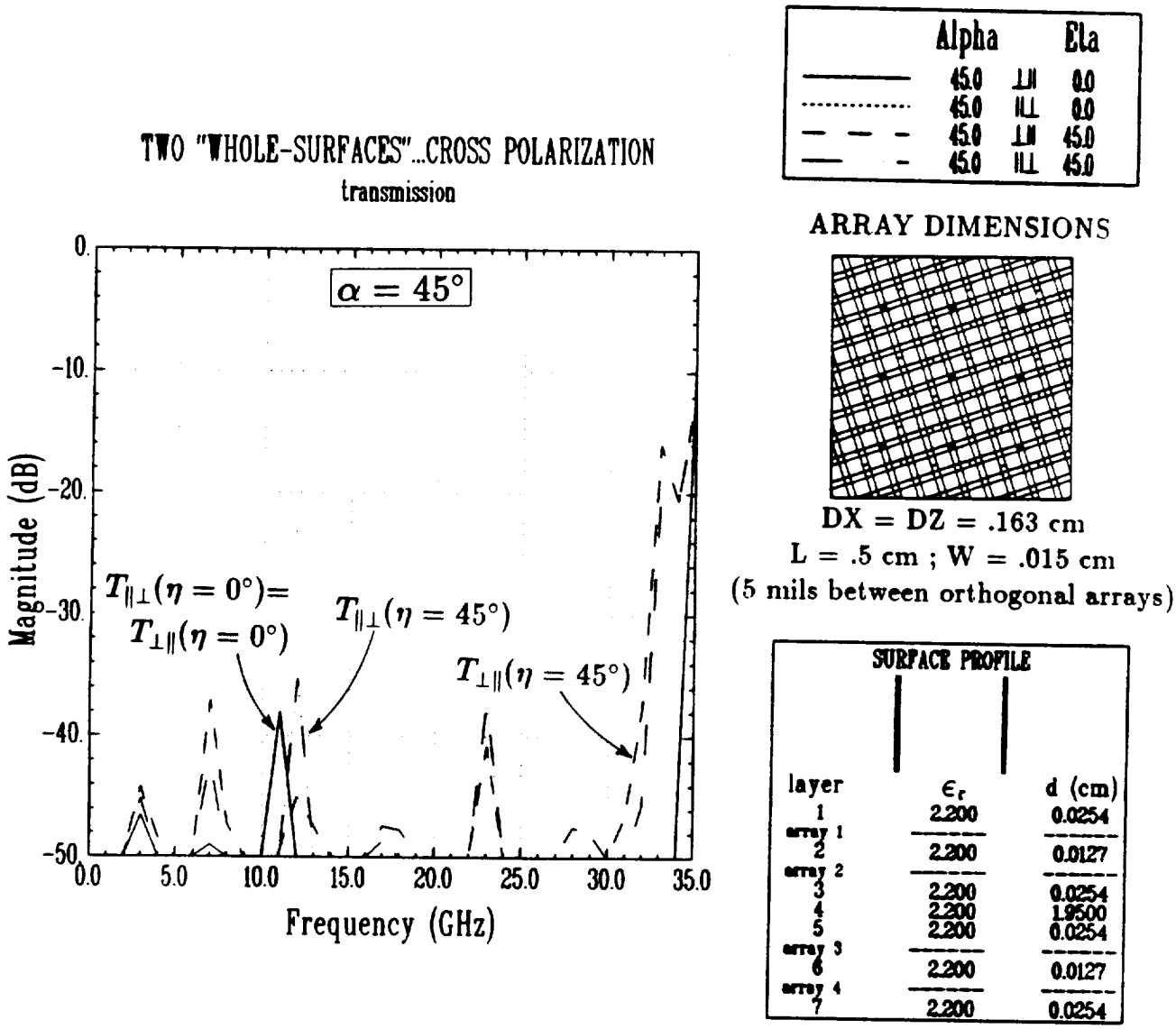

Figure 4.24: The cross polarized transmission coefficient curves for the double array surface in the plane of incidence $\alpha = 45°$ at angles of incidence $\eta = 0°$ and $\eta = 45°$

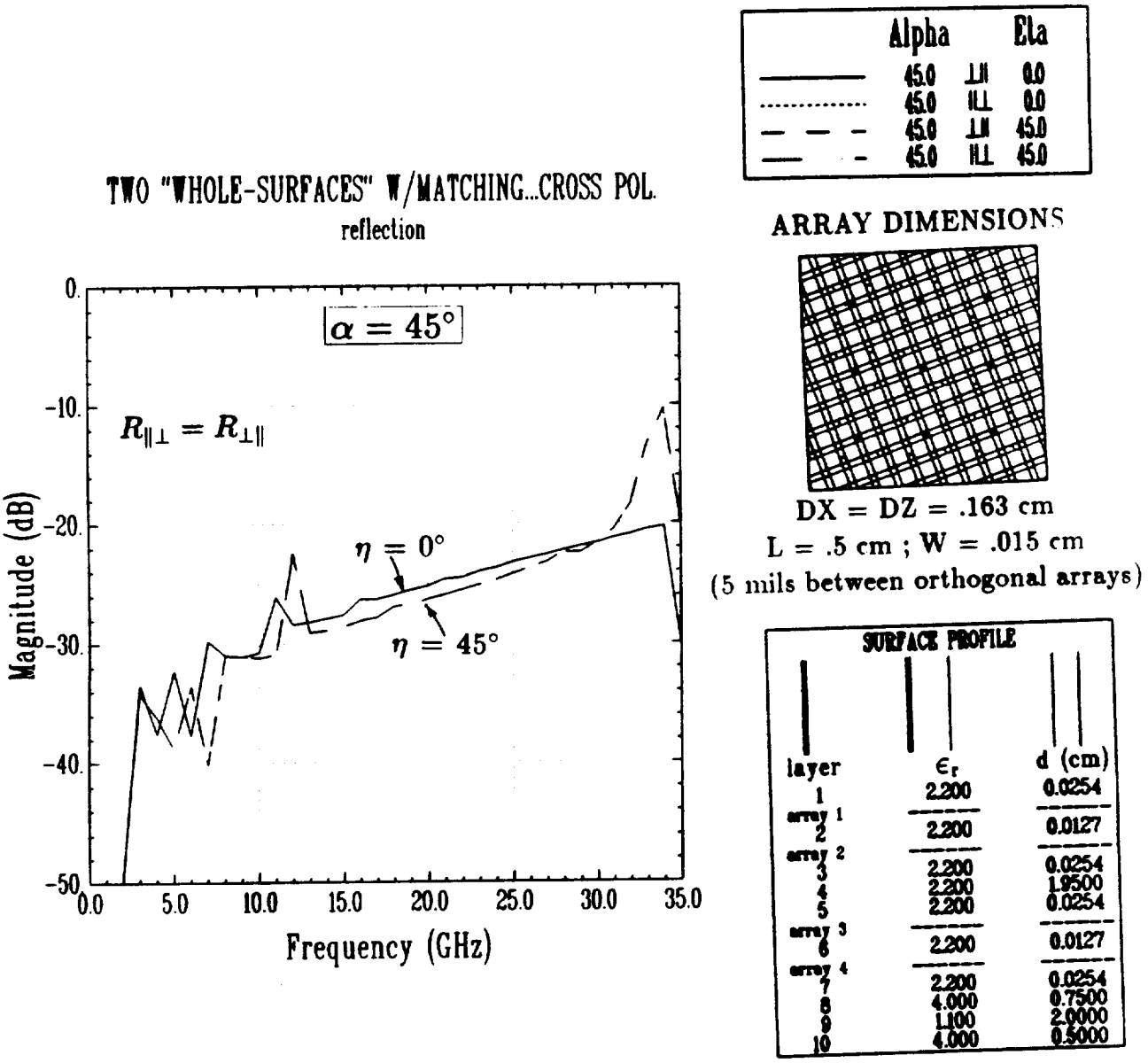

Figure 4.25: The cross polarized reflection coefficient curves for the double array surface with a matching plate in the plane of incidence $\alpha = 45°$ at angles of incidence $\eta = 0°$ and $\eta = 45°$

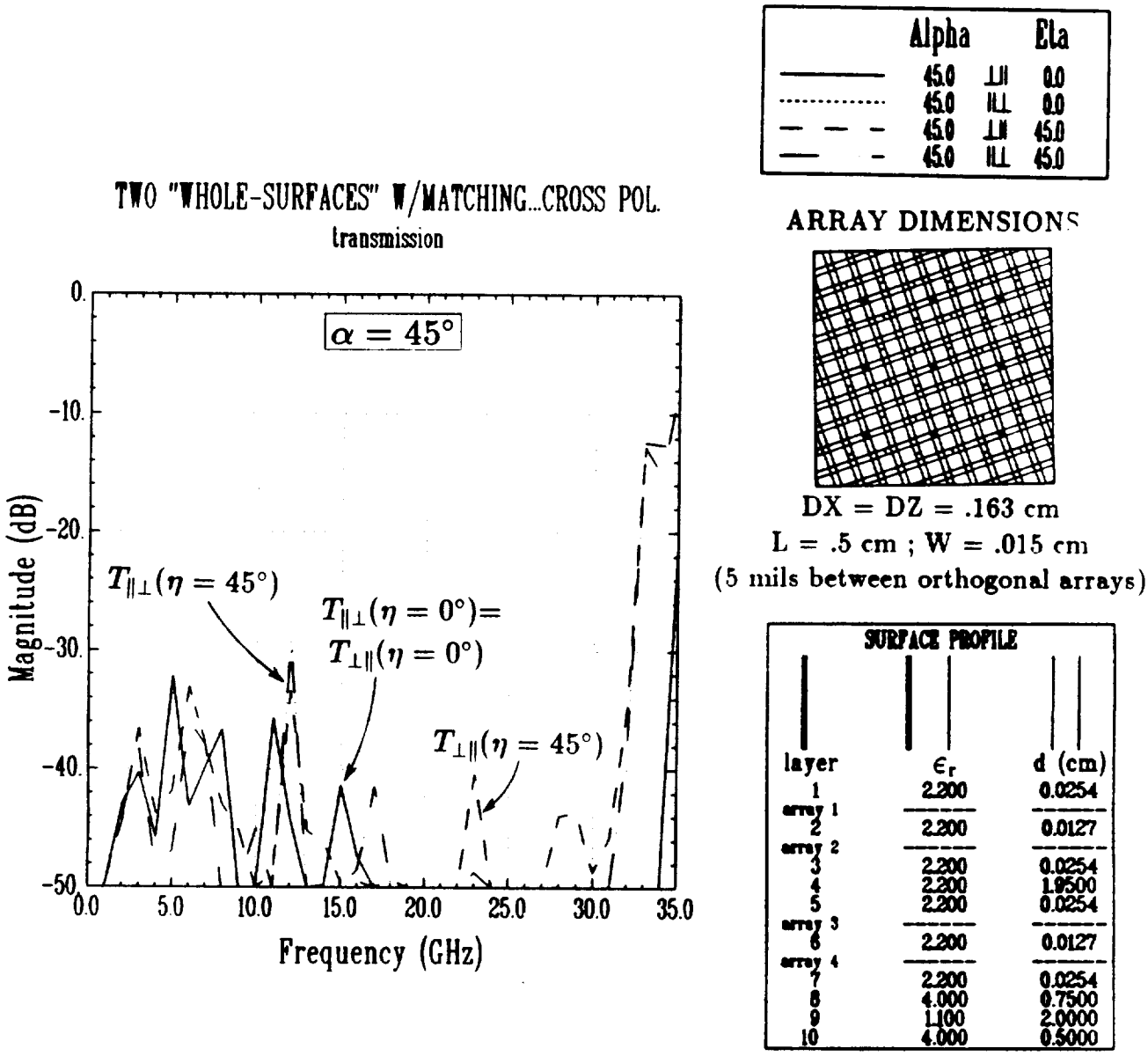

Figure 4.26: The cross polarized and transmission coefficient curves for the double array surface with a matching plate in the plane of incidence $\alpha = 45°$ at angles of incidence $\eta = 0°$ and $\eta = 45°$

Chapter 5

Conclusions

We have, in this report, developed a dichroic surface design that is reflective in the Ka-band from 22.5-27.3 GHz, and the Ku-band from 13.7-15.1 GHz, while transmitting in the S-band from 2.0-2.3 GHz, for arbitrary planes of incidence and all angles of incidence out to 45°.

In Chapter 2 we formulated a design approach for the parallel polarized component. Specifically, we first found a single surface that resonated high enough to avoid the "modal interaction null" in the Ka-reflection band out to $\eta = 45°$ in the E-plane, yet had enough bandwidth to be reflective in the Ku-reflection band. Next, we added a second array a distance "d" behind the first to produce a flatter reflection coefficient and introduce a transmission region at S-band. The thickness of "d" was carefully chosen to avoid "surface interference nulls" in our Ku-band reflection region for all required angles of incidence. Finally, we added a dielectric matching plate to enhance the low frequency transmission coefficient. We observed that the addition of the dielectric matching plate had little effect in the reflection bands since "a short is a short".

In Chapter 3 we considered how loss effected our dichroic surface design. We found that dielectric loss tangents on the order of .001 showed no noticable deterioration of the design. We noted in this chapter that the transmission coefficient was more effected by dielectric loss than is the reflection coefficient. This is because the transmitted field must pass through all of the lossy dielectrics, and these dielectrics are electrically very thick at the higher frequencies. We further noted that the dielectric substrates had a substantial effect on the reflection loss since the field around the elements was highly concentrated. Finally, we showed that copper loss was insignificant at our design frequencies.

In Chapter 4 we replaced the "gangbuster half-surfaces" in the dichroic surface design with "gangbuster whole-surfaces". We noted that the cross polarized component of the reflected signal in a "gangbuster whole-surface" increased monotonically with frequency. Specifically, we found that the reflection cross polarization was less than -22.5 dB when the array separation was "s" = 5 mils (for frequencies up to 30 GHz and angles up to $\eta = 45°$). We demonstrated that the bisecting plane (i.e. $\alpha = 45°$) produced the highest cross polarization levels since the mutual coupling was greatest in this plane. We further showed that for fields incident in non-principal planes (i.e. the field is not directed along the elements) the reflection cross polarization was greater than the transmission cross polarization.

Also in Chapter 4, the effect of array separation "s" was investigated. We found that as the separation was increased, the cross polarization levels increased. Below resonance we saw, on average, a 6 dB increase in the cross polarization level each time the separation distance was doubled. However,

above resonance the cross polarization was nearly equal for all these separations. This is because the cross polarization above resonance is dominated by array mutual coupling.

We finally observed, in Chapter 4, the cross polarization of our double array dichroic surface design with a matching plate. The cross polarization coefficients of this design did not differ much from that of the single "gangbuster whole-surfaces". We saw that again the maximum reflection cross polarization level in the frequency band from 0-30 GHz was -22.5 dB. The transmission cross polarization level in this same band was never more than -30 dB.

As a final note, we point out that it is possible to calculate the amount of energy that is lossed as heat in a practical dichroic surface. This is done in Appendix A. In the appendix we take our dichroic surface design and calculate its efficiency for a relatively high dielectric loss tan=.01.

Appendix A

Efficiency of Dichroic Surfaces

In this brief section we investigate the efficiency of a lossy dichroic surface having the reflection properties shown in Figure A.1 for various dielectric loss tangents at normal angle of incidence. We note that this is our dichroic surface comprised of "gangbuster whole-surfaces". The figure insert gives all pertinent surface dimensions. It is obvious from this figure that a low loss tangent has a high efficiency and consequently very little heat build up in the surface.

For illustration purposes we calculated the efficiency of the dichroic surface in Figure A.1 with a relatively poor dielectric loss tangent = .01. Table A.1 shows the unit normalized scattered power (both reflected and transmitted) when the surface is exposed to an unit normalized incident field. In the first column we show the frequency. The second column contains the total normalized scattered power for the lossless case, the third contains the total normalized scattered power for the dielectric loss tan = .01 case. (The variation of normalized total scattered power in the lossless case from the ideal normalized value of 1.0 is due to roundoff error.)

Table A.1: The calculated efficiency of the dichroic surface of Figure A.1 having a dielectric loss tan=.01 at various frequencies.

FREQUENCY (GHz)	LOSSLESS P_1	LOSS TAN=.01 P_2	EFFICIENCY P_2/P_1
2.0	1.003	0.957	0.954
5.0	0.993	0.910	0.916
8.0	1.002	0.987	0.985
11.0	0.998	0.866	0.867
14.0	1.005	0.982	0.977
17.0	1.003	0.980	0.977
20.0	1.004	0.981	0.977
23.0	1.004	0.981	0.977
26.0	1.005	0.982	0.977
29.0	1.006	0.984	0.978
32.0	1.008	0.985	0.977
35.0	1.008	0.943	0.936

We find the efficiency (the last column) by dividing the lossy case by the lossless case.

From Table A.1 and Figure A.1 we observe a few things. In the reflective region ($\sim 12-35$ GHz) the loss is quite small and relatively constant. The reason for this is that most of the incident power is reflected by the front surface and therefore must pass through only the front dielectric substrate (which is a tiny fraction of a wavelength for all frequencies considered here). In the transmitting region ($\sim 2-11$ GHz) the loss is greater and is more dependent on the frequency. This is because more of the total input power is transmitted through the entire lossy surface (which is several wavelengths long even at these low frequencies).

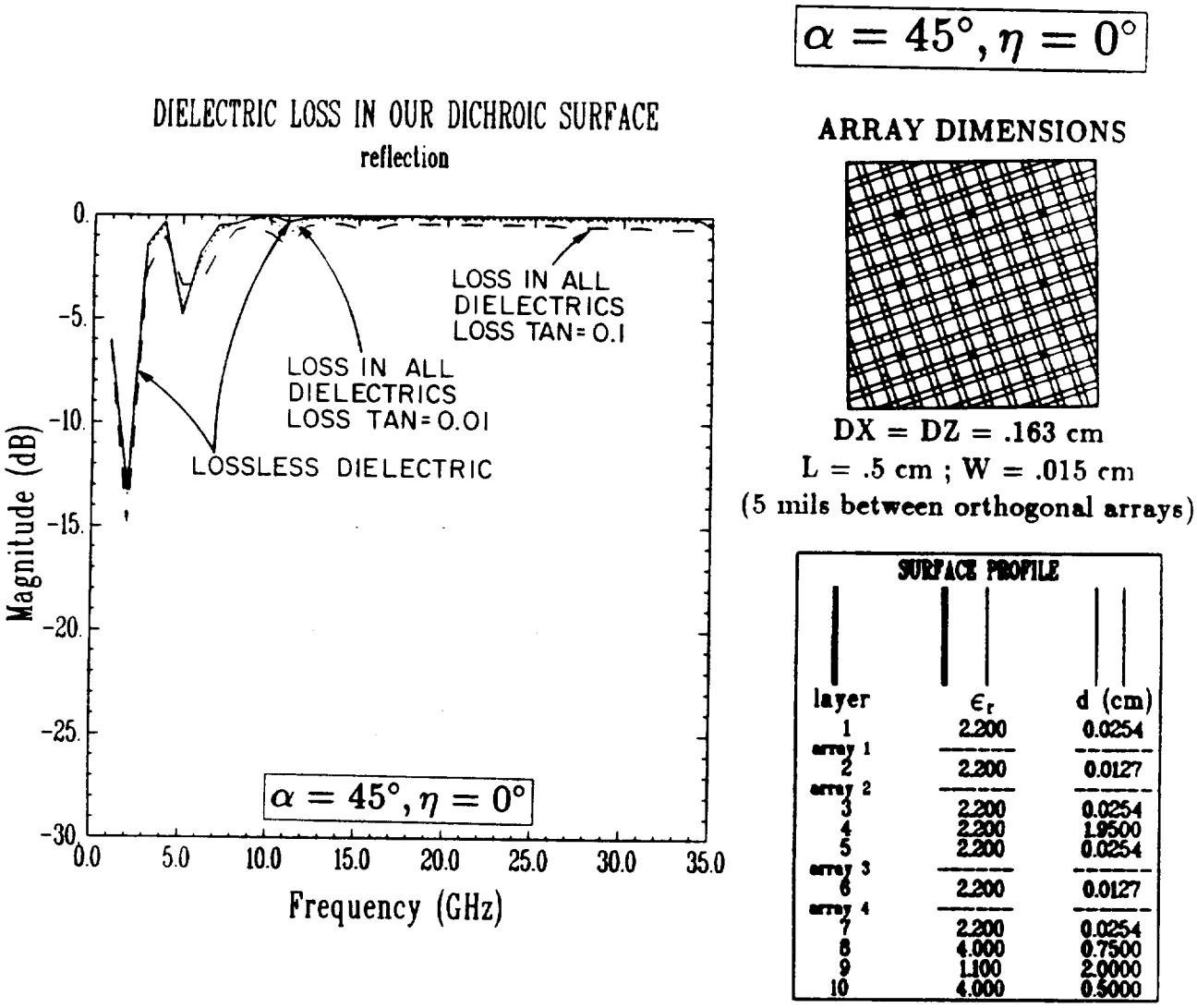

Figure A.1: The reflection coefficient curves for our dichroic surface at normal angle of incidence with dielectric loss tan = 0, .1, and .01.

Table A.2: The power density converted into heat due to a dielectric loss tan=.01 for various input power densities, and at various frequencies.

FREQUENCY (BAND) (GHz)	INPUT POWER DENSITY (dB_{W/m^2})	EFFICIENCY	POWER DENSITY INTO HEAT (W/m^2)
2.0 (S)	40.0-48.0	0.954	460.-2902.
14.0 (Ku)	41.0	0.977	290.
23.0 (Ka)	45.5	0.977	816.
26.0 (Ka)	45.5	0.977	816.

From the results of Table A.1 we may find the total power density converted into heat for some practical input power densities. The results of these calculations are given in Table A.2 for frequencies in our region of interest (S-band, Ku-band and Ka-band).

50272-101

REPORT DOCUMENTATION PAGE	1. REPORT NO.	2.	3. Recipient's Accession No.
4. Title and Subtitle The Reflection and Transmission Properties of a Triple Band Dichroic Surface			5. Report Date December 1990 6.
7. Author(s) S.W. Schneider and B.A. Munk			8. Performing Org. Rept. No. 723108-1
9. Performing Organization Name and Address The Ohio State University ElectroScience Laboratory 1320 Kinnear Road Columbus, OH 43212			10. Project/Task/Work Unit No. 11. Contract(C) or Grant(G) No. (C) (G) NCC3-158
12. Sponsoring Organisation Name and Address National Aeronautics and Space Administration Lewis Research Center 21000 Brookpark Road, Cleveland, OH 44135			13. Report Type/Period Covered Technical Report 14.

15. Supplementary Notes

16. Abstract (Limit: 200 words)

This report details the development of a triple-band dichroic surface design that is reflective in the Ka-band from 22.5-27.3 GHz and the Ku-band from 13.7-15.1 GHz, yet transparant in the S-band from 2.0-2.3 GHz, for all planes of incidence, and for all angles of incidence out to $\eta = 45°$. The design is comprised of two "gangbuster whole-surfaces" separated by a distance "d", that is comparable to a fraction of a wavelength in S-band, and enhanced by the addition of a dielectric matching plate. The "gangbuster" array is comprised of tighly packed straight skewed dipole elements referred to as "half-surfaces". Two of these "half-surfaces" are oriented orthogonal to each other and placed an array separation distance "s" apart to form the "gangbuster whole-surface" which allows any arbitrary plane of incidence. Results are given for the triple-band design with and without dielectric and conduction losses. We further investigate the cross polarization properties of the dichroic surface. It is shown here that the reflection cross polarized component is dominated by the geometry of the front "whole-surface" of our design (particularly the array separation "s") and is never more that -22.5 dB in the frequency band 0-30 GHz. The transmission cross polarization component is dependent on both "whole-surfaces" and is never more than -30 dB in the same frequency band.

17. Document Analysis a. Descriptors

b. Identifiers/Open-Ended Terms

c. COSATI Field/Group

18. Availability Statement	19. Security Class (This Report)	21. No. of Pages
A. Approved for public release; Distribution is unlimited.	Unclassified	
	20. Security Class (This Page) Unclassified	22. Price

(See ANSI-Z39.18) *See Instructions on Reverse* OPTIONAL FORM 272 (4-77)
Department of Commerce